Weydt *et al. Geothermal Energy* (2022) 10:5
https://doi.org/10.1186/s40517-022-00212-8

Geothermal Energy

RESEARCH Open Access

Petrophysical characterization of the Los Humeros geothermal field (Mexico): from outcrop to parametrization of a 3D geological model

Leandra M. Weydt[1*], Kristian Bär[1] and Ingo Sass[1,2]

*Correspondence:
weydt@geo.tu-darmstadt.de
[1] Department of Geothermal Science and Technology, Technische Universität Darmstadt, Schnittspahnstraße 9, 64287 Darmstadt, Germany
Full list of author information is available at the end of the article

Abstract

The Los Humeros Volcanic Complex has been characterized as a suitable target for developing a super-hot geothermal system (> 350 °C). For the interpretation of geophysical data, the development and parametrization of numerical geological models, an extensive outcrop analogue study was performed to characterize all relevant key units from the basement to the cap rock regarding their petrophysical properties, mineralogy, and geochemistry. In total, 226 samples were collected and analyzed for petrophysical and thermophysical properties as well as sonic wave velocities and magnetic susceptibility. An extensive rock property database was created and more than 20 lithostratigraphic units and subunits with distinct properties were defined. Thereby, the basement rocks feature low matrix porosities (< 5%) and permeabilities (< 10^{-17} m^2), but high thermal conductivities (2–5 W m^{-1} K^{-1}) and diffusivities (≤ $4{\cdot}10^{-6}$ m^2s^{-1}) as well as high sonic wave velocities (≥ 5800 m s^{-1}). Basaltic to dacitic lavas feature matrix porosities and permeabilities in the range of < 2–30% and 10^{-18}–10^{-14} m^2, respectively, as well as intermediate to low thermal properties and sonic wave velocities. The pyroclastic rocks show the highest variability with respect to bulk density, matrix porosity (~ 4– > 60%) and permeability (10^{-18}–10^{-13} m^2), but feature overall very low thermal conductivities (< 0.5 W m^{-1} K^{-1}) and sonic wave velocities (~ 1500–2400 m s^{-1}). Specific heat capacity shows comparatively small variations throughout the dataset (~ 700–880 J kg^{-1} K^{-1}), while magnetic susceptibility varies over more than four orders of magnitude showing formation-related trends (10^{-6}–10^{-1} SI). By applying empirical correction functions, this study provides a full physiochemical characterization of the Los Humeros geothermal field and improves the understanding of the hydraulic and thermomechanical behavior of target formations in super-hot geothermal systems related to volcanic settings, the relationships between different rock properties, and their probability, whose understanding is crucial for the parametrization of 3D geological models.

Keywords: Super-hot geothermal systems, Los Humeros geothermal field, Reservoir characterization, Petrophysical and thermophysical properties, Sonic wave velocities, Magnetic susceptibility

Introduction

Super-hot geothermal systems (> 350 °C, SHGS) are important targets for electric power production and have recently been of high interest in the industry and scientific community (Reinsch et al. 2017). An important threshold is achieved when reservoir fluids reach supercritical conditions and recent studies have proven that the extraction of supercritical fluids increases the productivity by a factor of ten compared to conventional wells, including fossil fuels (Cladouhos et al. 2018; Friðleifsson et al. 2014a, b). However, the majority of previous deep and high-temperature drilling projects encountered several problems like corrosion and scaling due to aggressive reservoir fluids, unsuccessful cementing operations as well as damage of the casing material or surface equipment, which often led to well failure and abandonment (Reinsch et al. 2017). To exploit these super-hot reservoirs and to be able to handle the challenging conditions in the reservoir, comprehensive and detailed exploration is needed to enhance the reservoir understanding and modeling (Reinsch et al. 2017; Jolie et al. 2018).

The majority of high-temperature geothermal resources at comparatively shallow depths (< 4 km) are linked to volcanic settings, which often exhibit a complex structural architecture and geological evolution, resulting in various rock types with highly variable mineralogical and hydromechanical characteristics (Pola et al. 2012; Heap and Violay 2021). Furthermore, hydrothermal alteration, diagenetic and metamorphic processes significantly change the properties of the rocks (Frolova et al. 2014; Aretz et al. 2016; Mielke et al. 2015; Villeneuve et al. 2019). The prediction of the thermo-hydro-mechanical behavior of the target formations in the reservoir is challenging, which in turn is crucial to build conceptual geological models, to interpret geophysical data and to parameterize 3D numerical reservoir models. Comprehensive datasets are often scarce or focus on a limited number of parameters only and thus, subsurface models are commonly populated with generalized or assumed values resulting in high uncertainties (Bär et al. 2020). Since diagenetic, hydrothermal or metamorphic processes can enhance or decrease hydraulic, mechanical or thermal properties (Mielke et al. 2015; Wyering et al. 2014; Weydt et al. 2018a, 2021a; Durán et al. 2019; Heap et al. 2020a, 2021), the controlling factors need to be understood and considered during reservoir assessment also from an economical perspective.

The GEMex project (Horizon 2020; GA Nr. 727550) aims to develop new transferable exploration and exploitation approaches for enhanced (EGS) and super-hot unconventional geothermal systems (SHGS). For this purpose, the Los Humeros Volcanic Complex (LHVC) has been selected as demonstration site, which is the third largest active caldera in the Trans-Mexican Volcanic Belt (TMVB) hosting a hydrothermal system that reaches temperatures above 380 °C below 2 km depth (Pinti et al. 2017). The conventional hydrothermal reservoir of Los Humeros has been exploited and operated by the Comisíon Federal Electricidad (CFE) since 1990 (Romo-Jones et al. 2020) and 65 wells have been drilled so far. However, a sustainable utilization of these super-hot sections in the reservoir has not yet been realized. Various geological, geochemical, geophysical, as well as hydrological studies have been performed in the past and conceptual geological models were built and regularly updated (Cedillo 1999, 2000; Arellano et al. 2003). Nevertheless, recent studies revealed a much higher complexity of the reservoir than previously expected (Lucci et al.

2020; Carrasco-Núñez et al. 2021) and the understanding of the internal structure of the reservoir is still limited.

Within the framework of the GEMex project, which aims to build integrated reservoir models at a local, regional and supra-regional scale, preliminary 3D geological models were created (Calcagno et al. 2020) that served as the basis for the evaluation and incorporation of results from combined geological, geophysical and technical investigations (Jolie et al. 2018). Besides the latest update of the geological map (Carrasco-Núñez et al. 2017a), this was the first time that the regional geological formations were considered during exploration. However, until the beginning of the project, information on the different geological units and their physicochemical properties were not available. To overcome the lack of suitable data that meet the spatial coverage and resolution required within the project, a comprehensive outcrop analogue study was performed (Weydt et al. 2018b, 2021a). Therefore, all relevant key units from the cap rock to the basement were characterized regarding their mineralogy, geochemistry, petrophysical and mechanical properties on different scales: (1) macroscale (outcrops), (2) mesoscale (rock samples), and (3) microscale (thin section and chemical analyses). The investigation of outcrop analogues represents a cost-effective opportunity to investigate and correlate, e.g., facies, geologic heterogeneities, hydrothermal processes and petrophysical properties from outcrops to the subsurface and to create a representative dataset sufficient for various modeling approaches (Sass and Götz 2012).

In total, 226 outcrop samples were collected from more than 200 outcrops in the inside of the caldera, the surrounding area and in the exhumed fossil system in Las Minas, which is located east of the LHVC. The samples were analyzed for particle and bulk density, porosity, permeability, thermal conductivity, thermal diffusivity, p-wave and s-wave velocity as well as magnetic susceptibility. Whenever possible, each parameter was analyzed on each plug allowing for the identification of statistical and causal relationships between the parameters. This approach improves the accuracy of geostatistical predictions that are needed for upscaling or downscaling techniques or stochastic approaches. Complementary X-ray fluorescence measurements were conducted to obtain information on the bulk chemistry and to classify the samples into lithological units. New geochronological information obtained during the project were used to assign the samples to different stratigraphic units. Thin section and X-ray diffraction measurements were used to quantify the mineralogical composition as well as possible hydrothermal, metamorphic or diagenetic processes and their impact on the rock properties. Afterwards, the rock properties were statistically analyzed to define lithostratigraphic units with similar petrophysical characteristics and to investigate their variability and probability.

Here, we present a comprehensive dataset of laboratory-measured rock properties and a stepwise workflow for the prediction of in situ reservoir properties that provides the basis for a more precise resource and risk assessment of the Los Humeros geothermal field and geologically similar super-hot geothermal systems related to volcanic settings worldwide.

Geological setting

The LHVC is located about 185 km east of Mexico City and predominantly comprises Pleistocene to Holocene basaltic to rhyolitic volcanic rocks (Norini et al. 2019; Carrasco-Núñez et al. 2018). With a 21×15 km irregular shape, it is the largest and easternmost active caldera of the Trans-Mexican Volcanic Belt (TMVB), which is a E–W trending

about 1000 km long and up to 300 km wide Neogene calc-alkaline volcanic arc (López-Hernández et al. 2009; Fig. 1). The TMVB is commonly associated to the subduction of the Rivera and Cocos plates beneath the North American plate along the Middle-American Trench (Ferrari et al. 2012). The caldera structure developed in the Serdán-Oriental basin, which is a closed basin at the Mexican high plateau characterized by bimodal, mainly monogenetic volcanic structures of basaltic to rhyolitic composition (e.g., rhyolitic domes, scoria cones, lava fields, maars and tuff-rings) and older felsic domes (Yáñez and García 1982; Carrasco-Núñez et al. 2021). The basin is filled with Quaternary sediments, pyroclastic and volcanoclastic deposits and is limited to the east by large andesitic stratovolcanoes and dome complexes of the Cofre de Perote-Citlaltépetl volcanic chain and to the west by Miocene andesitic lavas of the Tlaxco-Cerro Grande range (Carrasco-Núñez et al. 2017a).

Based on new stratigraphic and geochronological data, the different geological units in the study area can be classified into: (1) post-caldera volcanism; (2) caldera volcanism; (3) pre-caldera volcanism and the (4) pre-volcanic basement (Carrasco-Núñez et al. 2017a and 2018; Figs. 1, 2).

The pre-volcanic basement group comprises the Paleozoic crystalline basement in the eastern TMVB, which is exposed in the Teziutlán Massif and partially covered by up

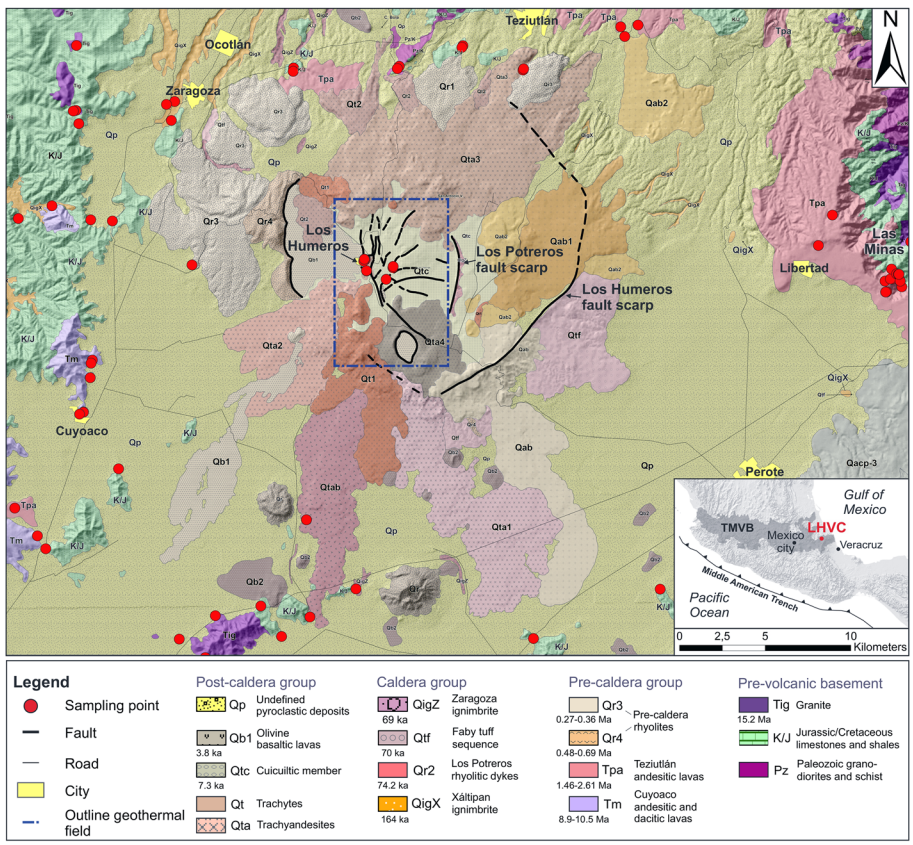

Fig. 1 Geological map of the LHVC slightly modified from Carrasco-Núñez et al. (2017a). The red points mark the sampling locations of the outcrop samples. Inset map showing the location of the LHVC and extension of the TMVB in Mexico

to 3000 m thick, intensively folded and thrusted Mesozoic sedimentary rocks belonging to the Sierra Madre Oriental (López-Hernández et al. 2009). The Teziutlán Massif consists of green schists, granites and granodiorites dated at 246–131 Ma representing the stratigraphically oldest units exposed in the study area (Carrasco-Núñez et al. 2018). The Mesozoic sedimentary successions include sandstones, shales, hydrocarbon-rich limestones and dolomites of Jurassic age, which are overlain by Cretaceous limestones, marls and shales. The basement was deformed by the Late Cretaceous–Eocene compressive Laramide Orogeny resulting in NW–SE striking thrusts and folds and subordinate NE-striking normal faults that are associated to an Eocene–Pliocene extensional tectonic deformation phase (Norini et al. 2019; Fítz-Díaz et al. 2017; López-Hernández et al. 1995). Oligocene to Miocene granitic and syenitic plutons as well as basaltic to andesitic dykes intruded into the sedimentary basement causing local metamorphism of marble, hornfels and skarn (Ferriz and Mahood 1984). Thereby, Eocene–Pliocene extensional structures acted as preferential pathways for Eocene–Oligocene magmatic intrusions preceding the onset of the subsequent volcanism in the study area (Norini et al. 2019; López-Hernández et al. 1995). Metamorphic rocks are exposed in the exhumed system of Las Minas east of the LHVC, which is considered as an analogue to the deeper reservoir rocks of the Los Humeros geothermal field (Olvera-García et al. 2020).

The pre-caldera volcanism in the study area is represented by Late Miocene (~10.5 ± 0.7 Ma K/Ar; Yáñez and García 1982) and Pliocene to Pleistocene lavas (1.44 ± 0.31 and 2.65 ± 0.43 Ma, Ar/Ar; Carrasco-Núñez et al. 2017a) of the Cuyoaco and Alseseca as well as Teziutlán andesite units, respectively. The Cuyoaco and Alseseca lavas mainly comprise andesitic and dacitic lava flows with a cumulative thickness of 800–900 m, which can be correlated to the Cerro Grande volcanic complex dated

a

Group	Stratigraphic units of the LHVC area	Age[a]
Post-caldera group	Pyroclastics (undifferentiated)	-
	Basaltic, trachyandesitc and trachytic lava flows	2.86 ka – 7.3 ka
	Cuicuiltic Member	7.3 ka
	San Antonio/Las Chapas trachyandesitic lava flows	8.9 ka
	Llano tuff	28.27 ka
	Maztaloya rhyodacite	<50 ka
	Xoxoctic Member	<50 ka[a,b]
	Rhyolitic domes	44.8 – 50.7 ka
Caldera group	Zaragoza ignimbrite	69 ka
	Faby tuff	70 ka
	Los Potreros rhyolitic lavas	74.2 ka
	Xáltipan ignimbrite	164 ka
Pre-caldera group	Rhyolitic lavas and domes	155.7 – 693 ka
	Teziutlán andesitic lavas	1.46 – 2.61 Ma
	Cuyoaco/Alseseca andesitic and dacitic lavas	8.9 – 10.5 Ma
Basement	Granites	15.2 Ma
	Skarn, Marble	12.18 – 17.8 Ma[c]
	Basaltic and andesitic dykes	11.2 – 16.5 Ma[d]
	Limestone, shale and sandstone	Cretaceous/Jurassic
	Igneous and metamorphic basement	131 – 246 Ma

References: a = Carrasco-Núñez et al. (2018), b = Willcox (2011), c = Fuentes-Guzmán et al. (2020) and d = Kozdrój et al. (2020) with c and d representing the Las Minas area only.

b

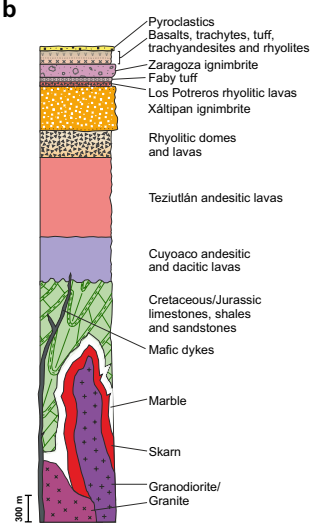

Fig. 2 Stratigraphy of the Los Humeros Volcanic Complex in **a** and a simplified stratigraphic profile in **b** based on Willcox (2011), Carrasco-Núñez et al. (2012, 2017a, 2017b, 2018), Olvera-García et al. (2020), and Calcagno et al. (2020). The color scheme is based on Carrasco-Núñez et al. (2017a). The estimated thickness or occurrence of the individual units might vary throughout the study area (not all units of the LHVC have been dated or described in detail yet and geological studies are ongoing)

between 8.9 and 11 Ma (K/Ar; Carrasco-Núñez et al. 1997; Gómez-Tuena and Carrasco-Núñez 2000). The fractured pre-caldera andesites form the currently exploited geothermal reservoir in the subsurface of the Los Humeros geothermal field. Thereby, the Teziutlán andesites have a reported thickness of up to 1500 m according to lithostratigraphic profiles the geothermal wells (Carrasco-Núñez et al. 2017b; López-Hernández et al. 1995; Fig. 2).

The beginning of the magmatic activity of the LHVC is represented by the emplacement of rhyolitic lavas and rhyolitic domes, which are mainly located at the western side of the LHVC (Carrasco-Núñez et al. 2017a). Radiometric ages of the domes range between 270 ± 17 and 693 ± 1.9 ka with occurrences at 486.5 ± 2.2 and > 350 ka (Ar/Ar and U/Th; Carrasco-Núñez et al. 2018; Ferriz and Mahood 1984).

The LHVC is associated with two main caldera-forming eruptions separated by large plinian and sub-plinian eruptive phases (Norini et al. 2019; Carrasco-Núñez et al. 2021) resulting in the outer Los Humeros caldera and the smaller inner Los Potreros caldera (8 × 10 km in diameter). The Los Humeros caldera collapse is associated with the emplacement of the high-silica rhyolite Xáltipan ignimbrite (164.0 ± 4.2 ka, Ar/Ar and U/Th; Carrasco-Núñez et al. 2018) with an estimated thickness of up to 880 m and a volume of 291 km^3 (dense rock equivalent, Cavazos and Carrasco- Núñez 2020). After the emplacement of the Xáltipan ignimbrite eruption, a sequence of explosive events (70.0 ± 23 ka, Ar/Ar, Carrasco-Núñez et al. 2018) lead to the deposition of thick rhyodacitic Plinian deposits called Faby Tuff (9–16 m thick in Ferriz and Mahood 1984). The second caldera-forming eruption is related to the deposition of the rhyodacitic to andesitic Zaragoza ignimbrite (69 ± 16 ka, Ar/Ar, Carrasco-Núñez et al. 2018; 2–60 m thick, Carrasco-Núñez et al. 2012, 2017b).

The most recent volcanic activity in the study area is represented by the post-caldera stage, which mainly consist of lava flows, scoria deposits as well as pumice fall out deposits with a highly lateral and vertical distribution, as well as a variable chemical composition. The unit can be divided into a Late Pleistocene resurgence phase and a Holocene reactivation phase (Carrasco-Núñez et al. 2021). The Late Pleistocene phase is characterized by rhyolitic and dacitic domes within the Los Humeros caldera center (44.8 ± 1.7 ka, U/Th; Carrasco-Núñez et al. 2018) and north of the Los Humeros caldera (55.7 ± 4.4 ka, Ar/Ar; Carrasco-Núñez et al. 2018) followed by a sequence of explosive eruptions producing dacitic pumice fall units (Xoxoctic Tuff; Ferriz and Mahood 1984), volcaniclastic breccias and pyroclastic flow deposits (Llano Tuff, ~ 10 m thick in Ferriz and Mahood 1984; Willcox 2011). During the Holocene alternated episodes of effusive and explosive eruptions occurred producing basaltic to trachyandesitic lava flows (8.9 ± 0.03 ka, C14; Carrasco-Núñez et al. 2017a, > 30 m thick in Ferriz and Mahood 1984) and basaltic and trachyandesitic fall out deposits (Cuicuiltic Member, 7.3 ± 0.1 ka, C14, ~ 1.5–8 m thickness; Dávila-Harris and Carrasco-Núñez 2014). The thickness of the post-caldera group ranges between 100 and 300 m in the wells (Carrasco-Núñez et al. 2017b; Fig. 2).

Materials and methods

Sampling campaign and sample preparation

In order to provide a reliable and sufficiently large data set for each target unit, a high sampling rate is required allowing the determination of statistical parameters and

probability distributions for numerical simulations (Hartmann et al. 2008). During the field campaigns 226 representative samples with a dimension of ~ 30 × 30 × 20 cm were collected from more than 200 outcrops inside of the caldera, in the surrounding area as well as in the exhumed system of Las Minas. Whenever possible, each geological unit was sampled several times at different outcrop locations to cover the unit's heterogeneity. Only samples with an overall fresh appearance unaffected by weathering were considered. Hydrothermal alteration was observed in some outcrops in close proximity to fault zones and dykes. In these cases, hydrothermally altered samples were deliberately collected to analyze the effect of these processes on the rock properties. The samples were directly drilled in the field or shipped as boulders to Germany. Cylindrical cores with diameters ranging from 25 to 64 mm were drilled from the outcrop samples and subsequently cut into plugs according to the international standard ASTM D4543 (2019) for the required sample length whereby the irregular and rough core ends were cut to be parallel to one another. In total 1507 plugs with an axial length ranging between ~ 25 and 128 mm were prepared from the outcrop samples. Thereby, short plugs (diameter: 25–40 mm, length: 25 to ~ 30 mm) were predominantly used for the non-destructive petrophysical measurements like bulk density, porosity and permeability due to the specific sample size requirements of the measurement devices. Remaining plugs were prepared to meet the requirements for different destructive rock mechanical tests, which were performed within the GEMex project (Weydt et al. 2021a). To ensure reproducibility of the results, the plugs were analyzed under oven-dried conditions (105 °C for more than 24 h or 64 °C for 48 h) and stored in in a desiccator at room temperature (20 °C). To perform measurements under saturated conditions, a vacuum desiccator (approx. − 1 bar) filled with de-ionized water was used.

Laboratory measurements

Material and methods of the petrophysical and geochemical measurements are described in detail in Weydt et al. (2021a), which also includes the raw data used in the figures and tables presented in this study. Thus, the measurement procedures are only mentioned briefly in the following sections. All measurements described below were performed under ambient laboratory temperature (~ 20 °C) and pressure (~ 0.1 MPa).

Grain and bulk densities were determined in a multi-step procedure using a helium pycnometer (AccuPyc 1330) and a powder pycnometer (GeoPyc 1360), thereby measuring the particle and bulk volume five times for each plug, respectively. Subsequently, porosity was calculated from the resulting differences in volume and represents the gas-effective porosity. The accuracy is given as 1.1% by the manufacturer (Micromeritics 1997, 1998).

The intrinsic matrix permeability was determined after Filomena et al. (2014) based on the principle of Klinkenberg (1941) using a column gas permeameter constructed according to ASTM D4525 (2013). The plugs were analyzed in a confined cell (1 MPa) with dried compressed air at five air pressure levels ranging from 1 to 3 bar. Measurement accuracy varies from 5% for high permeable rocks ($K > 10^{-14}$ m^2) to 400% for low-permeability rocks ($K < 10^{-16}$ m^2) (Bär 2012).

In order to determine bulk thermal conductivity and thermal diffusivity a thermal conductivity scanner (Lippmann and Rauen TCS) was used applying the optical scanning

method after Popov et al. (2016). Both parameters were measured four to six times on each plug for saturated and dry conditions, respectively. Measurement accuracy is 3% for thermal conductivity and 5% for thermal diffusivity (Lippman and Rauen 2009).

Specific heat capacity was determined using a heat-flux differential scanning calorimeter from Setaram Instrumentation (2009). Crushed sample material was heated at a steady rate from 20 up to 200 °C within a period of 24 h, thereby monitoring the heat flux in the sample chamber and an empty reference chamber. Specific heat capacities were derived from the resulting temperature curves through heat flow differences. The measurement accuracy is 1% (Setaram Instrumentation 2009). Subsequently, volumetric heat capacity was calculated by multiplying the specific heat capacity with the associated bulk density of each sample.

Compressional and shear wave velocities were measured using the Geotron USG40 (UKS-D) ultrasound generator from Geotron-Elektronik (2011) including a digital PicoScope oscilloscope and mounted point-source transmitter–receiver transducers. Continuous measurements were performed with a frequency of 80 kHz to 250 kHz and a constant contact pressure of 0.1 MPa. The arrival times of the p- and s-waves were picked manually. Both velocities were measured four to six times on each plug under saturated and dry conditions, respectively.

Magnetic susceptibility was analyzed with a magnetic susceptibility meter SM30 from ZH Instruments (2008). An interpolating mode was applied including two air reference measurements and one measurement directly on the sample surface. Each plane surface of a plug was measured five times to account for mineralogical heterogeneities.

Geochemical analyses included powder X-ray diffractometry (XRD) and X-ray fluorescence spectroscopy (XRF), which were performed at three different institutes (GFZ Potsdam, TU Delft and TU Darmstadt). XRD measurements were performed using a Bruker D8 Advance diffractometer and the software Diffrac.EVA (TU Delft) as well as the software Match! (GFZ). XRF measurements were conducted to analyze the bulk composition of the rock samples using a Panalytical Axios Max WD-XRF spectrometer and the SuperQ5.0i/Omnian software 15 (TU Delft) and a PANalytical AXIOS Advanced spectrometer in combination with the software Super Q (GFZ) as well as a Bruker S8Tiger 4 WD-XRF spectrometer using the Quant Express method (TU Darmstadt). Measurement accuracy is < 5% for the major elements and < 10% for the trace elements. The proposed limit of detection ranges between 400 ppm (Na) and < 10 ppm (e.g., Rb, Sr, Nb).

Furthermore, the samples were studied by optical microscope using thin sections and acetate peels, which were prepared from small 20 × 40 mm blocks cut from selected outcrop samples.

Data evaluation

Based on the results of the chemical and petrographic analyses the samples were classified into lithological units. New geochronological information provided by the project partners (Carrasco-Núñez et al. 2018; Kozdrój et al. 2019; Fuentes-Guzmán et al. 2020) was used to assign the samples to stratigraphic units, which allowed the definition of lithostratigraphic units as well as the correlation with the different regional and local model units of the preliminary 3D model of Los Humeros presented in Calcagno et al.

(2020). The results are displayed in "Petrophysical properties—data distribution and parameter correlations" section. Thereby, the color code is based on Carrasco-Núñez et al. (2017a) and SGM (2002).

To investigate the variability and distribution of the petrophysical properties, univariate descriptive statistical parameters such as mean, standard deviation, median, the 25% and the 75% quartiles and the coefficient of variance were determined, which are often used as a direct input in design calculations or numerical models (Hartmann et al. 2008). Scatter plots and histograms were created to allow for a quick investigation of the relationships between parameters and their probability distribution. Whenever required, lithostratigraphic units were divided into subunits that are petrophysically similar to increase the accuracy of predicting the unit's properties. A more complex statistical approach is the principal component analysis (PCA; Jolliffle 2005), which was used to visualize the whole data set and the relations between the properties as well as the lithostratigraphic units and subunits. The classification of Bär (2012) was used to evaluate the unit's properties regarding their geothermal potential. Descriptive statistics, scatter plots, normality and lognormality tests were performed using the software GraphPad Prism Version 8.0.2, while the PCA was performed using XLSTAT-biomat-2019.3.1 (Addinsoft, Boston, Massachusetts, USA).

Results

Sample classification and descriptions

Post-caldera group

Samples belonging to the post-caldera volcanism were predominantly collected inside of the Los Humeros caldera and comprise hydrothermally altered basaltic lavas, pyroclastic and ash fall deposits. The pyroclastic deposits represent the geologically youngest unit in the study area with an estimated age of < 2.8 ka (Carrasco-Núñez et al. 2018). They consist of soft, fine-grained beige to brownish, porous tuff with small phenocrysts of up to 3×5 mm in size (Fig. 3a). Outcrops are widely distributed around the caldera complex; however, the source of these pyroclastic deposits has not been identified yet (Carrasco-Núñez et al. 2017a) and thus, are referred to as "pyroclastics, undifferentiated" in this study.

Two different basaltic lava flows were sampled within the caldera complex. The first one represents a fractured Holocene pahoehoe lava flow north of the Los Humeros town building a rectilinear topographic scarp in the field (Norini et al. 2019). The lavas contain a dark grey to blackish, vesicular groundmass with a porphyritic texture (Fig. 3a) and the irregular vesicles (< 1 mm in diameter up to 5×10 mm) are often rimmed ore partially filled with secondary clays and alteration minerals. This particular lava flow has not been dated yet, but according to Carrasco-Núñez et al. (2017a) the age of these young olivine-bearing basaltic lava flows in the study area is about 3.87 ± 0.13 ka (unit Qb1 in Fig. 1) representing one of the last volcanic stages related to the caldera activity. Furthermore, it overlies the Cuicuiltic Member, which has been dated at 7.3 ± 0.1 ka (Carrasco-Núñez et al. 2017a). The second basaltic lava related to the post-caldera volcanism was retrieved from an outcrop located east of the Los Humeros town representing the Xoxoctic member as described in Willcox (2011). The collected samples consist of a blackish, vesicular and fractured groundmass with a porphyritic texture. The samples show

a weak-to-moderate hydrothermal overprint, especially along fractures, and the pores are often partially filled with secondary clays. Further sample material collected from the Xoxoctic member contains soft, fine-grained and well-sorted, highly porous beige to reddish ash fall deposits.

Caldera group

Outcrop samples representing the caldera group of the LHVC include the Zaragoza and Xáltipan ignimbrites (Fig. 3a). Samples of the Zaragoza ignimbrite were collected inside of the caldera east of the town of Los Humeros and comprise beige, poorly sorted, lithic-rich, fine-grained, partially welded lapilli tuff with a dacitic composition (Fig. 4a). The samples contain numerous angular white to black lava clasts and pumice that are highly variable in size and occasionally fiamme structures.

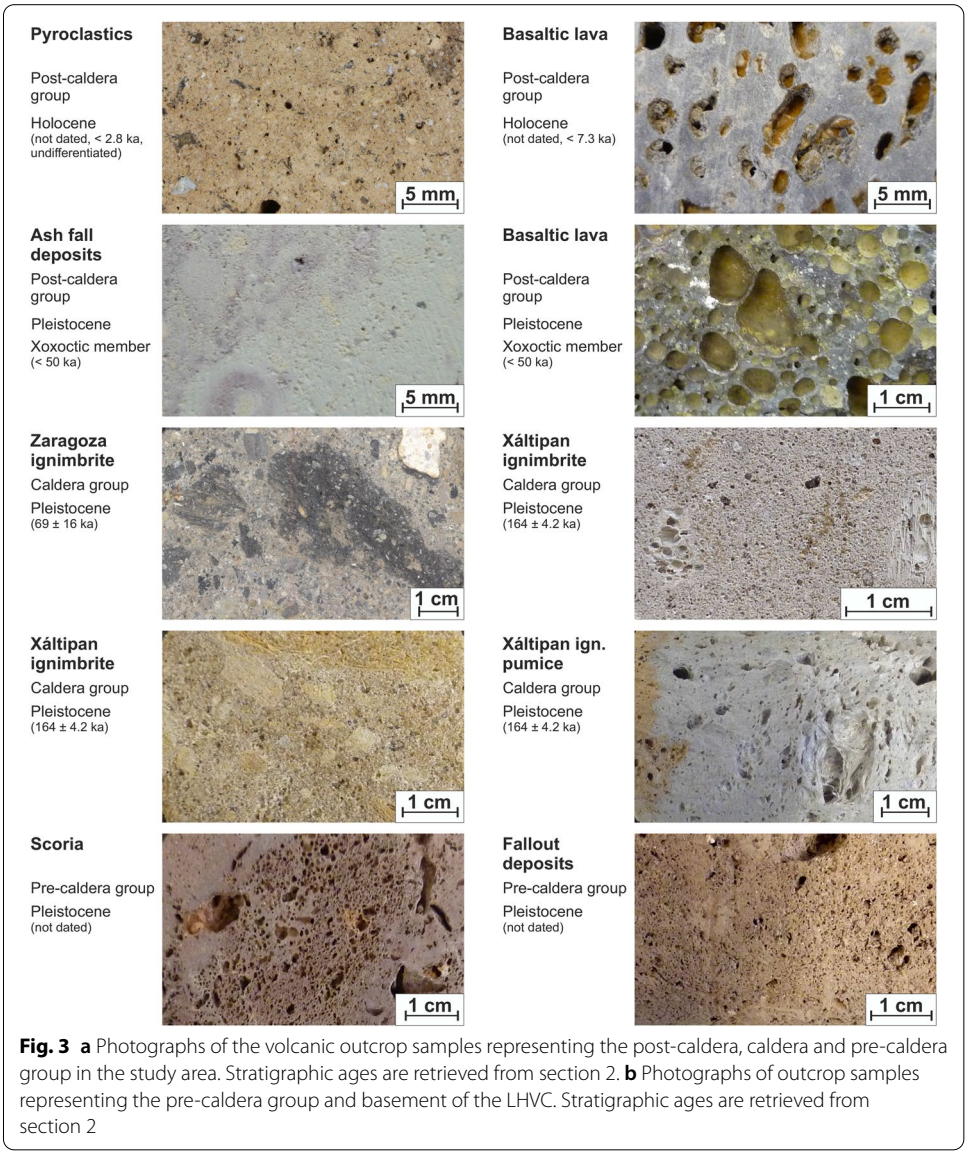

Fig. 3 **a** Photographs of the volcanic outcrop samples representing the post-caldera, caldera and pre-caldera group in the study area. Stratigraphic ages are retrieved from section 2. **b** Photographs of outcrop samples representing the pre-caldera group and basement of the LHVC. Stratigraphic ages are retrieved from section 2

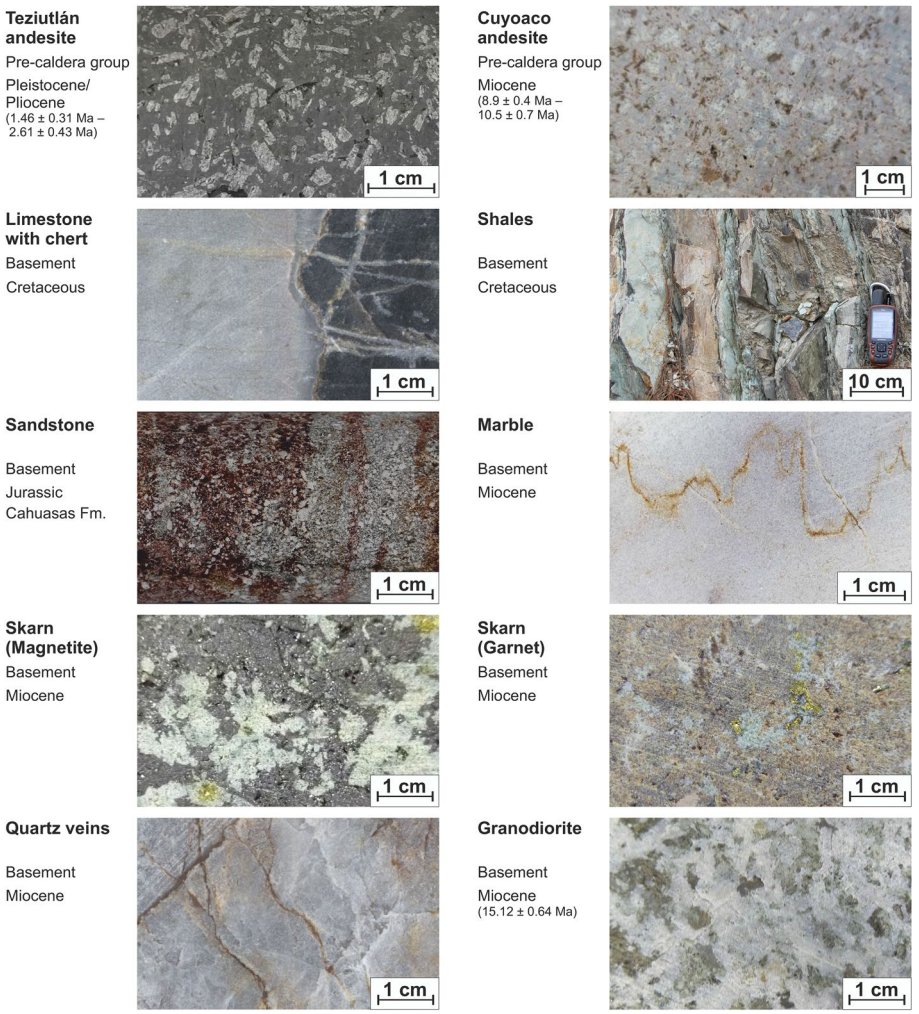

Fig. 3 continued

Samples of the Xáltipan ignimbrite were collected from several outcrops, quarries and road cuts in the surrounding area of the caldera complex. The samples represent a heterogenous collection of predominantly non-welded to slightly welded, matrix-supported, massive lapilli tuff and pumice fallout deposits. XRF measurements of selected samples reveal a rhyolitic composition (Fig. 4a). The color is highly variable and ranges from rosé over reddish to ochre–brown–grey. Likewise, the clast load ranges from a few pumice clasts to abundant lithic fragments (volcanic rock fragments, but also intrusive and sedimentary fragments from the pre-volcanic basement). Vesicles in the pumice fallouts vary widely in both size and shape, but are commonly elongated. In addition, one sample of beige, massive, welded tuff was collected west of the town Cuyoaco, which has been affected by hydrothermal alteration (argillization in form of secondary clays, occasionally microcrystalline quartz in fractures; further details are presented in Cavazos-Álvarez et al. 2020).

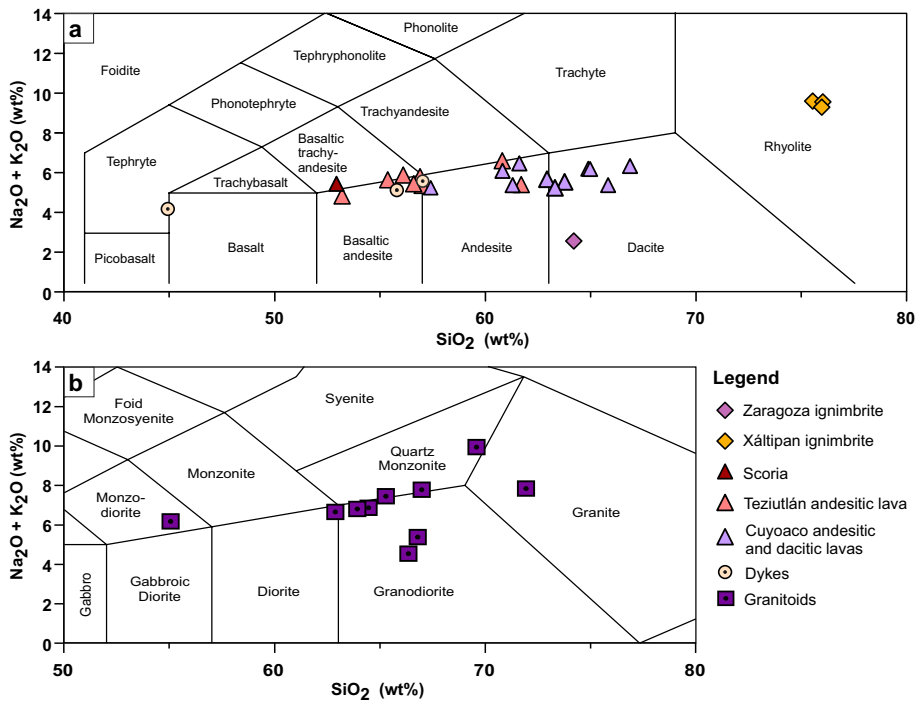

Fig. 4 Total alkali versus silica (TAS) diagram for the **a** volcanic (Le Maitre et al. 2002) and **b** plutonic outcrop samples (Middlemost 1994)

Pre-caldera group

Samples related to the pre-caldera group include the Teziutlán and Cuyoaco andesite units (Fig. 3b) as well as scoria and fallout deposits. The latter was collected from a scoria cinder cone located approximately 5 km west of the Los Humeros caldera, which can be related to a sequence of basaltic and basaltic andesitic scoria cones dated at 190 ± 20 ka (Carrasco-Núñez et al. 2017a). Results of the XRF measurements of the scoriaceous lava revealed a basaltic trachyandesitic composition (Fig. 4a). The samples consist of a reddish-brown color, aphanitic texture and abundant ellipsoidal vesicles (< 1 mm up to 2 cm in length). The fallout deposits represent soft ashes to ash tuff, which are reddish-brown in color, fine-grained, well-sorted and occasionally contain small blackish to grey lava fragments (< 1 cm in length). Since this unit has not been investigated in greater detail yet, we refer to it as scoria and fallout deposits in this study.

The Teziutlán andesite unit comprises dark grey to medium grey, basaltic andesitic to andesitic lavas with a porphyric to glomeophyric texture. The lavas are often fractured and predominantly massive without macroscopically visible pores. Several outcrops located northeast of the Los Humeros caldera (east of the town Teziutlán) comprise vesicular basaltic andesitic lavas. Phenocrysts commonly consist of plagioclase, pyroxene and minor olivine, while the groundmass predominantly comprises microcrystalline plagioclase.

Outcrops of the Miocene Cuyoaco andesite unit occur west of the Los Humeros caldera close to the town Cuyoaco as well as southwest of the caldera complex. The collected samples comprise grey to slightly reddish, fractured and massive andesitic to

dacitic lavas with a porphyritic to glomeophyric texture and a microcrystalline groundmass that mainly comprises plagioclase. The phenocrysts predominantly consist of plagioclase, pyroxene and minor olivine. In contrast to previous studies (Ferriz and Mahood 1984, Carrasco-Núñez et al. 2017a), hornblende was not identified. However, both andesite units have not been investigated in greater detail yet and further volcanological studies are needed to fully understand their temporal evolution and extension.

Pre-volcanic basement

Outcrops of the pre-volcanic basement are widely distributed in proximal distance around the Los Humeros caldera. However, metamorphic rocks like marble and skarns are only exposed in the exhumed system of Las Minas. The Cretaceous is mainly represented by light to dark grey, fine-grained, medium to thick bedded and intensively folded limestones (Figs. 3b, 13) often with black chert nodules (~ 5 to 20 cm thick, cm to dm scale in length) or interbedded ochre-brownish marl and chert layers with a thickness of ~ 5 to 25 cm. Referred from thin section analyses, the collected samples represent nonporous, open marine mudstones to wackestones. However, joints and fractures (< 1 mm to a few cm wide) are very common and often filled with calcite. Similarly, the chert layers and nodules contain numerous fractures that are usually filled with calcite. Furthermore, grey to greenish, fine-grained and finely laminated shales were collected from outcrops west of the town Cuyoaco. Due to their fragile nature, only a few plugs were suitable for petrophysical measurements. In addition, it was not possible to obtain samples from the friable marl layers. The Cretaceous outcrops in the study area predominantly correspond to the Tamaulipas Inferior and Tamaulipas Superior Formations and to a lesser extent to the Agua Nueva, San Felipe (Viniegra-Osario 1965; SGM 2011, 2012) and Orizaba Formation (predominantly in the Las Minas area; SGM 2007). Samples representing the Jurassic units comprise light to dark grey, thin to medium bedded, fine-grained limestones to argillaceous limestones (Pimienta, Taman and Santiago Formations; SGM 2011, 2012) and reddish-beige, medium to coarse, grain-supported sandstones of the Cahuasas Formation or so-called red beds (Ochoa-Camarillo et al. 1999). The limestones comprise nonporous mudstones to wackestones, which commonly contain fine, calcite-filled veins (< 1 mm wide). The samples of the Cahuasas Formation are made of rather fairly sorted angular grains of quartz and feldspar, occasionally granophyric grains and trace amounts of clay minerals coated by iron oxides that cause the reddish color of the samples. Pores are generally smaller than 1 mm and fractures are unfilled.

Outcrops of intrusive rocks are spread over the study area, but are best accessible in the exhumed system of Las Minas (Figs. 3b, 13). The collected samples predominantly represent granodiorites, but also have monzodioritic, dioritic to granitic compositions (Fig. 4b). For the following evaluation, the samples are referred to as 'granitoids' in this study. The samples usually contain quartz, plagioclase, K feldspar, hornblende, biotite and pyroxenes. The majority of the collected granitoids showed a weak-to-moderate hydrothermal overprint (greenish-greyish color and minerals such as epidote, chlorite or sericite). Strongly altered and fractured samples often containing macroscopically visible fracture porosity were grouped separately as 'granitoids strongly altered'.

The intrusive bodies led to the generation of variable skarn assemblages with prograde mineralization caused by contact metamorphism followed by retrograde mineralization due to hydrothermal alteration along fractures and fault zones (Fuentes-Guzmán et al. 2020). According to Fuentes-Guzmán et al. (2020) the skarns can be classified into endoskarns with grossular-andradite, clinopyroxenes, and quartz in prograde associations, and magnetite, chalcopyrite, bornite, and native gold in retrograde associations as well as exoskarns, which comprise wollastonite, clinopyroxenes, potassium feldspar, quartz, epidote, and chromian muscovite. The collected samples show a high mineralogical variability and span from brownish garnet-dominated, greenish-grey magnetite-dominated to reddish hematite-dominated skarn associations. Quartz veins range from centimeter to meter scale and occur associated with skarn bodies. They are most likely the product of cooled down silica- and iron-rich fluids sealing existing fractures. Furthermore, they consist of several generations of quartz and are intensively fractured indicating a repeated reactivation and sealing of these fractures.

The formation of marble is caused by the contact metamorphism during Miocene as described above (Fig. 13l). The collected samples have a calcic to dolomitic composition, vary from white to grey in color and contain a fine to coarse grain size with a granoblastic texture. Since the marbles are predominantly associated to skarn deposits and intrusions along large fractures and fault zones, they often contain numerous veins and fractures and hydrothermal minerals such as wollastonite, diopside, garnet, serpentine and talc were identified (Rochelle et al. 2021). Several mafic dykes crosscutting the Cretaceous formations and intrusive bodies (Fig. 13o) were observed in the outcrops. They commonly contain a basaltic to andesitic composition (Fig. 4a), blackish to dark grey color and predominantly have an aphanitic as well as occasionally a porphyric texture.

Petrophysical properties—data distribution and parameter correlations

The results of the petrophysical analyses are displayed in the cross-plots, histograms and boxplots of Figs. 5, 6, 7 and 8, respectively.

Except for the pumice fallout deposits and skarns, particle density is relatively constant throughout the data set and ranges between 2.64 and 2.80 g cm^{-3} (Figs. 5e, 7a). Bulk density, porosity and permeability are highly variable ranging from 0.48 to 4.27 g cm^{-3}, from < 1 to 73% and from 10^{-20} to 10^{-10} m^2 (Figs. 5, 6, 7), respectively. Matrix porosity and bulk density are negatively correlated, while porosity and permeability show only a weak correlation (Fig. 5a). Matrix porosity of the units related to the pre-volcanic basement is generally lower than 5%, while only the Jurassic sandstones exhibit porosities of about 21%. Higher porosities observed on the limestones and metamorphic rocks are mainly caused by fractures and microfractures and their associated mineralization products (e.g., quartz and calcite fillings), which leads to a right skewed distribution, as is the case for the Cretaceous limestones (Fig. 6l) and skarns (Fig. 6v). Likewise, fractures increase the in general low matrix permeabilities (median: 10^{-17} to 10^{-18} m^2) about several orders of magnitudes (up to 10^{-10} m^2 for skarns). With respect to matrix porosity and permeability, the volcanic rocks can be grouped into: (1) low-porous samples (< 5%) with predominantly fracture controlled permeabilities (e.g., Cuyoaco andesite); (2) samples with intermediate porosity (~ 10–16%) and low to high permeability due to vesicular pores and occasionally

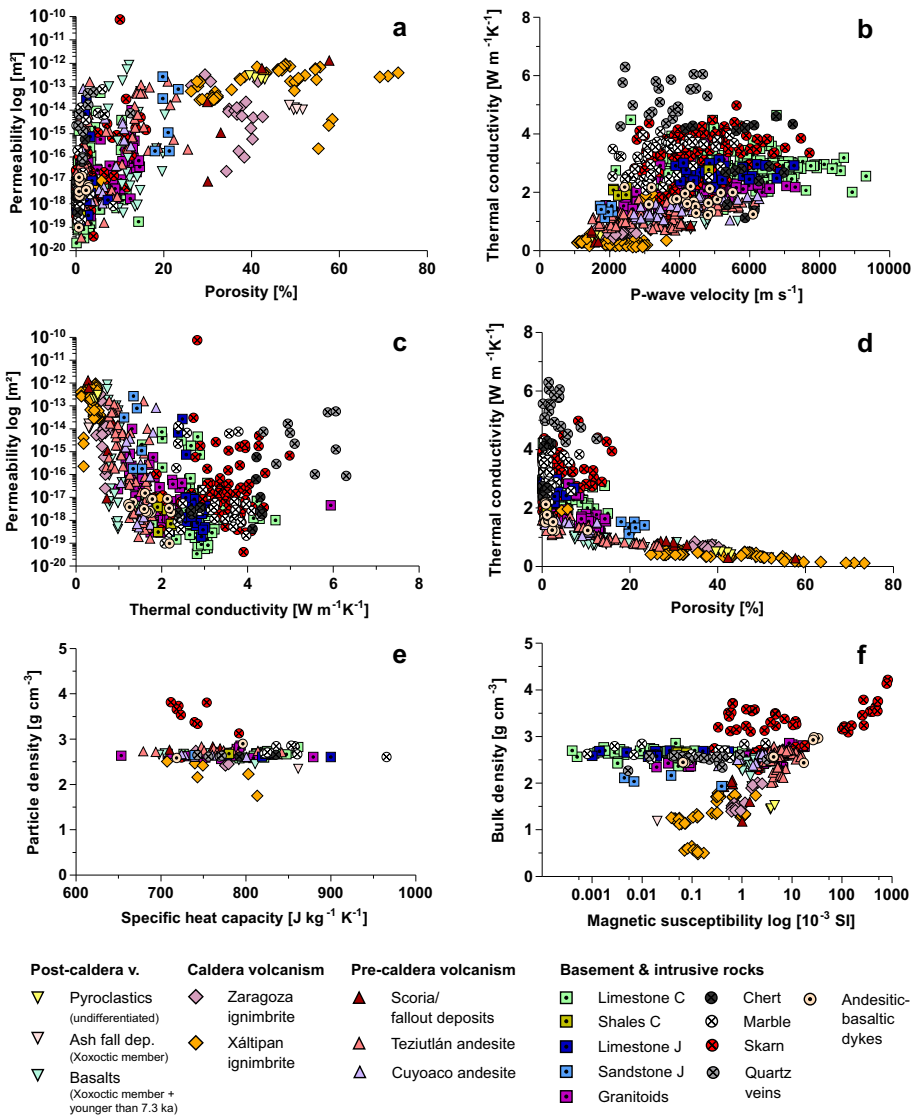

Fig. 5 Scatter plots of selected rock properties analyzed under dry conditions of the outcrop samples with respect to their lithostratigraphic units

fractures (e.g., Teziutlán andesite porous); and (3) samples with high porosities (> 20%) and permeabilities that are predominantly pore controlled ($> 10^{-15}$ m^2; ignimbrites, ash fall and pumice fallout deposits). Some units reveal distinct bimodal or multimodal distributions for bulk density, porosity or permeability (Fig. 6). In order to provide representative average values for each unit with respect to the scale of the 3D model, further subunits were defined (Figs. 7 and 8). For example, the properties of the Xaltipán ignimbrite were subdivided into Xaltipán ignimbrite (unwelded–partially welded), Xaltipán ignimbrite (pumice) and Xaltipán ignimbrite (altered and welded).

Thermal conductivity and thermal diffusivity vary from 0.17 ± 0.03 (Xáltipan ignimbrite pumice) to 5.25 ± 0.61 W m^{-1} K^{-1} (quartz veins) and from 0.37 ± 0.02

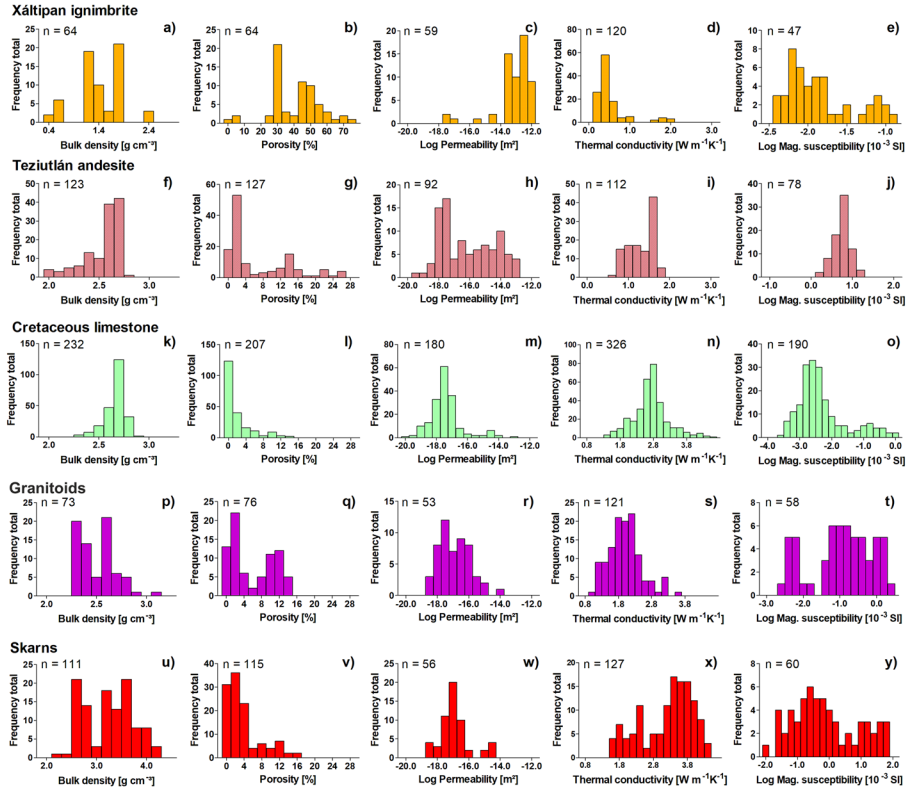

Fig. 6 Histograms of selected units for bulk density, porosity, permeability, thermal conductivity and magnetic susceptibility. *N* = number of analyzed plugs. **a**–**e** Xáltipan ignimbrite, **f**–**j** Teziutlán andesite unit, **k**–**o** Cretaceous limestone, **p**–**t** granitoids and **u**–**y** skarns

(pyroclastics) to $4.30 \pm 1.08\ 10^{-6} \cdot m^2\ s^{-1}$ (quartz veins), respectively. Thermal conductivity and thermal diffusivity of the volcanic rocks show a strong positive correlation with matrix porosity (Fig. 5d) and to a lesser extend with p-wave (Fig. 5b) and s-wave velocity. Furthermore, both parameters decrease with decreasing bulk density and increasing permeability (Fig. 5c). In contrast, the units belonging to the pre-volcanic basement show a higher scattering while correlating thermal conductivity and diffusivity with porosity, permeability or p-wave velocity. However, rock type-specific clusters are identifiable. Furthermore, Figs. 6 and 7 imply that besides porosity, mineral composition and to a lesser extent microfractures play an important role. Thermal conductivity analyzed under saturated conditions increased for all rock types; up to 0.75 W m^{-1} K^{-1} for porous samples like the Xáltipan ignimbrite (Table 4). Thermal diffusivity, however, changes for each unit differently under saturated conditions. For marbles, saturated thermal diffusivity is almost twice as high compared to dry conditions, while it shows reduced values for the intensively fractured quartz veins (Table 4).

The average specific heat capacity shows only a small variation within the data set ranging from 707 J kg^{-1} K^{-1} (Xáltipan ignimbrite altered) to 833 J kg^{-1} K^{-1} (pyroclastics, Table 6). Thus, volumetric heat capacity follows the same trends as described for bulk density.

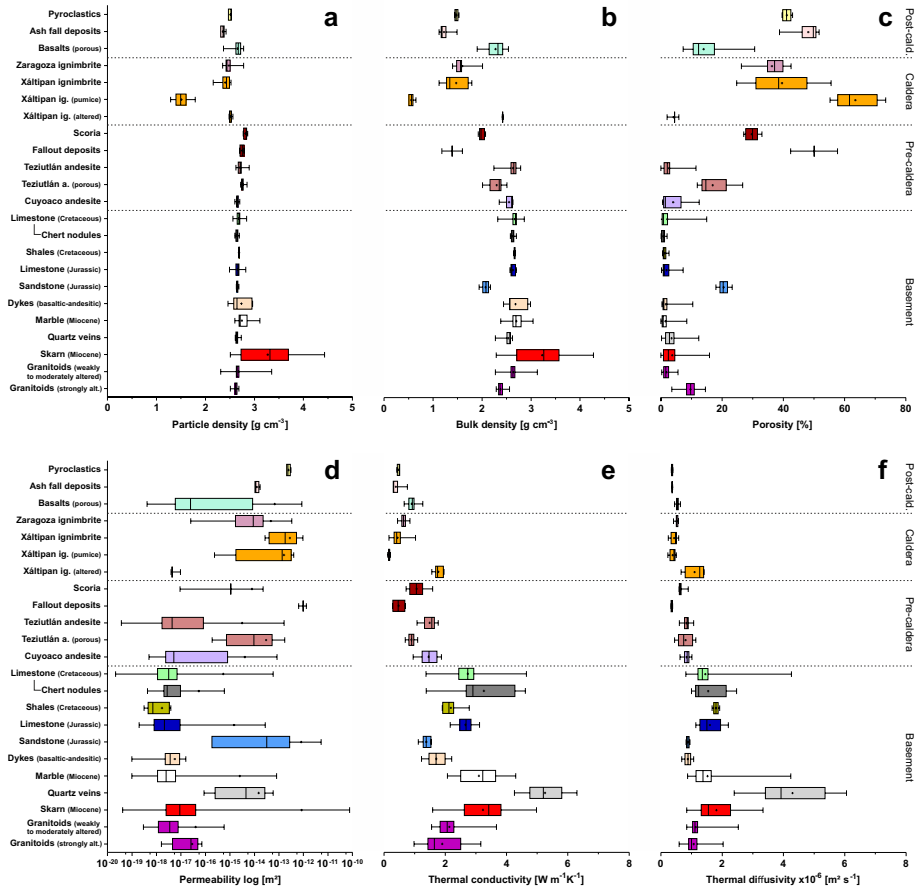

Fig. 7 Box plots of petrophysical (**a**, **b**), hydraulic (**c**, **d**) and thermal properties (**e**, **f**) of the outcrop samples analyzed under dry conditions

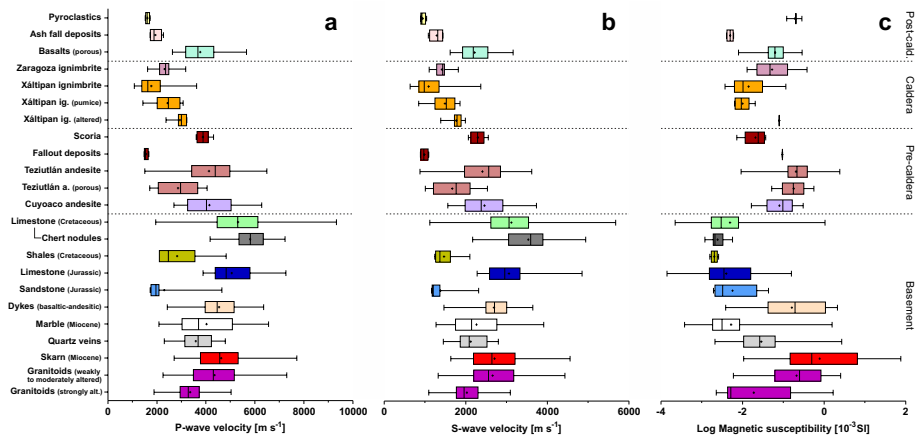

Fig. 8 Ultrasonic wave velocities (**a**, **b**) and magnetic susceptibility (**c**) of the outcrop samples analyzed under dry conditions

The results of the ultrasonic wave measurements reveal a wide parameter range for individual units. Thereby, the units with high porosities like ash fall deposits or samples with foliation like shales comprise lower p-wave velocities and s-wave velocities in the range of ~ 1500 to 3000 m s^{-1} and ~ 1000 to 1800 m s^{-1}, respectively (Figs. 5 and 8). The basaltic to andesitic lavas, intrusive and metamorphic rocks show intermediate values (p-wave: 2000–6000 m s^{-1}; s-wave: 1000–5500 m s^{-1}), while the Cretaceous limestones exhibit the highest variability with values of up to 9300 m s^{-1} for p-wave velocity (Fig. 8). The correlation of the sonic wave velocities with porosity and thermal conductivity shows rock type-specific clusters, but overall, only a weak correlation (Fig. 5). Furthermore, the correlation with permeability shows no trend at all. P-wave and s-wave velocity analyzed under saturated conditions is significantly higher and increase up to 45% (pyroclastics, Table 5).

Magnetic susceptibility ranges from − $0.12 \cdot 10^{-3}$ SI (Cretaceous limestones) to $818.5 \cdot 10^{-3}$ SI (skarns, Figs. 5, 6, 8) throughout the data set. Contrary to the parameters described above, magnetic susceptibility is not affected by matrix porosity and strongly depends on the mineralogical composition of the samples and their magnetic behavior. The correlation with bulk density reveals an almost linear trend for the sedimentary and metamorphic rocks, while the volcanic units show an exponential trend (Fig. 5f, negative values are not presented in this graph). As common for sedimentary rocks, the limestones, shales, marbles, but also the Jurassic sandstones are characterized by a diamagnetic to paramagnetic behavior, thus, showing slightly negative to slightly positive magnetic susceptibilities (10^{-5} to 10^{-4} SI). The slightly higher values and the resulting bimodal distribution observed on the Cretaceous limestones can be attributed to fracture fillings in samples collected in close proximity to dykes (Fig. 6o). The basaltic to andesitic lavas exhibit magnetic susceptibilities of about one to two orders of magnitudes higher compared to the sedimentary rocks, while the pyroclastic rocks show a very variable magnetic behavior featuring slightly negative magnetic susceptibilities to positive values in the order of magnitude of 10^{-3} SI. Hydrothermal alteration observed on the intrusive rocks significantly reduces the magnetic susceptibility from ~ 5.2 to 0.036 10^{-3} SI resulting in a bimodal distribution (Fig. 6t). Magnetic susceptibility of the skarn samples ranges about four orders of magnitude. Thereby, the skarns that are rich in calcite or garnet show slightly positive magnetic susceptibilities (10^{-4} SI), while skarns with magnetite reveal the highest values (10^{-1} SI, Figs. 6y and 8).

A principal component analysis (PCA) was applied to assess the differences between each unit and subunit regarding their petrophysical characteristics (Fig. 9). Thereby, PCA in total covered 65.66% of the overall variation in the dataset, while factor F1 contributed with 52.34% to the separation of the units and subunits, whereas factor F2 accounted for 13.32%. Overall, ~ 4/5 of the displayed variation among the units and subunits can be attributed to factor F1, whereas the remaining ~ 1/5 can be attributed to factor F2 (Fig. 9). The variables (in this case the rock parameters) porosity, specific heat capacity, and thermal conductivity predominantly contributed towards factor F1. In contrast, permeability, magnetic susceptibility, and particle density mostly contributed towards factor F2. The impact of the variable's bulk density, thermal diffusivity, and the sonic wave velocities is in large parts observable on axis F1, but to a lesser extent also noticeable on axis F2. The distance of the variables from the origin of the plot indicates

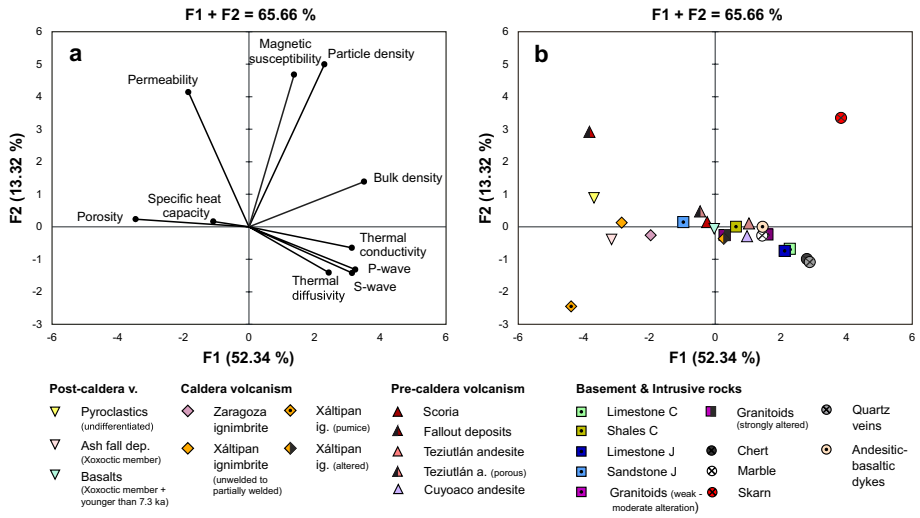

Fig. 9 Principal component analysis applied to the magnetic susceptibility, sonic wave velocities as well as petrophysical, and thermophysical properties of the investigated lithostratigraphic units and subunits of the LHVC. **a** Represents the contribution of each parameter to the overall separation between the units and subunits as shown by factors F1 and F2. Each data point in **b** represents arithmetic means of all analyzed plugs for the respective unit or subunits

their impact on the overall variance. Thus, particle density, magnetic susceptibility, permeability had the highest variances, whereas specific heat capacity clearly had the lowest variance (Fig. 9a). On one hand, the parameters magnetic susceptibility and particle density, p-wave and s-wave velocity as well as porosity and specific heat capacity each showed a strong correlation. On the other hand, porosity and specific heat capacity are negatively correlated with thermal conductivity, thermal diffusivity, and the sonic wave velocities as was previously observed in the cross-plots (cf. Figure 5). In addition, it is important to note, that permeability, magnetic susceptibility, and particle density were mostly indifferent to the remaining seven parameters.

Based on the PCA, the units and subunits can be separated into three groups, namely the highly porous pyroclastic rocks like the Xáltipan and Zaragoza ignimbrites, the major cluster of rocks comprising, e.g., the Jurassic sandstones and granitoids (F1: − 2 to 2 with decreasing porosity and increasing thermal conductivity and sonic wave velocities), and metamorphic rocks like quartz and skarn (Fig. 9b), which exhibit high thermal conductivities or magnetic susceptibilities. Figure 9b shows that differences within a lithostratigraphic unit are in some cases higher than those between different units, as is the case for the Xáltipan ignimbrite or Teziutlán andesite.

Discussion

Petrophysical characterization of the Los Humeros geothermal field

The investigation of outcrop analogues revealed the complexity and high geological variability of the key formations in the study area that are relevant for modeling the Los Humeros geothermal field. The composition, lateral extension and distribution of the volcanic sequences are very variable, particularly of the cap rock and post-caldera group, but also the pre-volcanic basement showed a high geological heterogeneity consisting

of several different rock types like limestones, shales, sandstones, mafic dykes as well as marble, quartz and skarn that are associated with intrusive bodies.

The high geological variability of the different units is also depicted in the results of the petrophysical measurements. The youngest volcanic sequences and the upper sections of the cap rock consist of alternating pyroclastic deposits and basaltic to rhyodacitic lavas showing contrasting physiochemical characteristics. Thereby, the ash fall deposits and ignimbrites can be characterized as highly porous (> 35%) and permeable with a very low thermal conductivity (dry conditions: ≤ 0.5 W m^{-1} K^{-1}) and diffusivity ($\leq 1{\cdot}10^{-6}$ m^2 s^{-1}), but high heat capacity (> 760–880 J kg^{-1} K^{-1}). Due to their weak mechanical strength and high compressibility (Table 6), they are very sensitive to pressure changes with increasing depth.

The post-caldera lavas, however, feature very low to intermediate porosities (< 5–15%) and matrix permeabilities ($< 10^{-16}$–10^{-14} m^2). Thermal conductivity and diffusivity are also very low to low (< 1.5 W m^{-1} K^{-1} and $\leq 1{\cdot}10^{-6}$ m^2 s^{-1}, respectively), but bulk density and sonic wave velocities are significantly higher compared to the pyroclastic rocks.

The Xáltipan ignimbrite represents the thickest section of the cap rock and in contrast to the aforementioned units has a much larger lateral extension (~ 50 km in both directions from the Los Humeros caldera). From a petrophysical perspective, this unit shows the highest variability and widest parameter range and can be grouped into a non-welded to partially welded facies, a highly welded facies and pumice fall outs. The samples collected in this study predominantly represent the non-welded to partially welded facies and pumice fall outs that show high to very high porosities (> 35– > 60%) and high permeabilities (10^{-13} m^2). With only one sample location, the welded facies are somehow underrepresented, due to the limited number of outcrops in the sampling area. Furthermore, a revised petrographic description and map of the Xáltipan ignimbrite was just recently published (Cavazos-Álavarez et al. 2019, 2020) and the extension of this unit was significantly smaller in previous studies (Ferriz and Mahood 1984; Willcox 2011; both do not include the welded facies). The welded and hydrothermally altered samples collected in this study are characterized by a very low matrix porosity (~ 4%) and permeability ($6{\cdot}10^{-18}$ m^2) as well as intermediate thermal properties (1.8 W m^{-1} K^{-1} and $1.4{\cdot}10^{-6}$ m^2 s^{-1}). According to Cavazos-Álavarez et al. (2020) the transition from non-welded over partially welded to highly welded is gradual from top to base and matrix porosity and permeability range from 52 to 4% and $2{\cdot}10^{-12}$ to $2{\cdot}10^{-18}$ m^2 ($n = 9$), respectively, which is well in line with the results presented here. In previous conceptual geothermal models, the Xáltipan ignimbrite was described as a texturally homogenous and low permeable unit with a uniform lateral extension that act as an aquitard in the geothermal system (Cedillo 1999, 2000). However, the recent petrographic and petrophysical investigations identified distinct lateral and vertical heterogeneities (this study and Cavazos-Álavarez et al. 2020).

The lavas belonging to the pre-caldera group feature properties in a similar range than the lavas of the post-caldera group. Thereby, the laterally and vertically most extensive and thus most important unit is the Teziutlán andesite, which hosts the currently exploited geothermal reservoir in the Los Humeros geothermal field. Regarding its spatial extension, the Teziutlán andesites predominantly consist of fractured and massive low porous and low permeable lavas and to a lesser extent of vesicular lavas. Thereby, the

ratio of massive versus porous lavas is similar than observed in the geothermal reservoir (Lorenzo-Pulido et al. 2008, Deb et al. 2019) suggesting that fluid flow in the pre-caldera group is predominantly fracture controlled.

Except for the Jurassic sandstones, the investigated units belonging to the basement are characterized by a very low matrix porosity (< 4%) and permeability (10^{-18} m^2). Fractures are abundant and higher porosities observed for example in limestones are associated with fractures and fracture filling minerals. The weak correlation between matrix porosity and permeability indicates that fluid flow is predominantly fault controlled in the study area, which has been confirmed by Lelli et al. (2020). Likewise, hydrothermal alteration observed in outcrops is predominantly restricted to fractures and fault zones (Weydt et al. 2021a). Alteration observed in granitic samples increased matrix porosity and permeability, but reduced the thermal properties, sonic wave velocities and magnetic susceptibility. Thermal conductivity and thermal diffusivity of the basement rocks can be classified as intermediate to high and are significantly higher than observed for the overlying volcanic sequences, while the results for specific heat capacity show a similar range. However, limestones and marbles make up the largest proportion of the basement and revealed significantly higher specific heat capacities compared to the magmatic and metamorphic rocks. Likewise, the limestones show the highest sonic wave velocities. The wide parameter range observed on the sonic wave velocities might be the result of mineralogical differences between the outcrops, the abundance of microfractures and the sample size. In general, small samples (30 mm length) contain less microfractures and thus, tend to have higher sonic velocities than larger ones (125 mm length). However, more detailed investigations would be required to provide a final conclusion.

Figures 7, 8, 9 show that the low-porous andesites, carbonates and intrusive rocks feature bulk densities, porosities, permeabilities and p-wave velocities in a similar range, making the interpretation of geophysical surveys at greater depth increasingly difficult. However, the results of the magnetic susceptibility measurements are highly variable throughout the dataset showing formation-related trends, which might be helpful to identify skarn bodies and intrusions in the basement as well as alteration zones or highly porous layers in the volcanic successions. Magnetic susceptibility measurements are very sensitive to mineralogical changes even on a cm-scale and thus, have been frequently used in mapping, mineral exploration (Hrouda et al. 2009, Baroomand et al. 2015), to solve geotechnical problems (von Dobeneck et al. 2021) or to investigate hydrothermal alteration in geothermal reservoirs (Oliva-Urcia et al. 2011).

The comparison with literature data (Table 1) underlines the importance of a detailed petrophysical characterization for each case study in order to avoid under- or overestimation of thermal, storage and fluid flow properties or mechanical behavior.

Particularly, the petrophysical properties of volcanic rocks are highly variable and are mostly controlled by matrix porosity and secondly by the occurrence of microfractures (Mielke et al. 2015; Navelot et al. 2018; Heap et al. 2020b). Notable are also the drastic decrease of matrix porosity with increased welding observed in ignimbrites from Central Mexico (Lenhardt and Götz 2015). However, the decrease of matrix permeability with increasing welding observed on samples of the Xáltipan ignimbrite is even two orders of magnitude higher. Similar to observations presented in Heap and Kennedy (2016), the porosity–permeability relationships of the volcanic rocks cannot be described with one

Table 1 Petrophysical data retrieved from literature—1 = Mielke et al. (2015), 2 = Lenhardt and Götz (2015), 3 = Pola et al. (2016), 4 = Mielke et al. (2017), 5 = Navelot et al. (2018), 6 = Eshagi et al. (2019), 7 = Heap et al. (2020b), 8 = Weinert et al. (2021)

Rock type	ρ_B [g cm^{-3}]	ϕ [%]	K [m^2]	λ dry [W m^{-1} K^{-1}]	α dry [10^{-6} m^2 s^{-1}]	cp [J kg^{-1} K^{-1}]	V_P dry [m s^{-1}]	V_S dry [m s^{-1}]	χ [10^{-3} SI]	Ref
Ash tuff	1.57 (125)	40.56 (125)	3E-14 (125)	0.79 (125)		630 (125)				1
Scoria, pumice and ashes	1.52 (20)	34.24 (16)	8E-13 (10)	0.54 (25)		880 (15)	1642 (17)		8.84 (14)	5
Tuff, non-welded		> 36	5.1E-15 (6)	0.5 (6)						2
Tuff, incipiently welded		30–36	6.4E-14 (17)	0.6 (17)						2
Tuff, partially welded		2–30	2.2E-14 (33)	0.9 (33)						2
Tuff, densely welded		< 2	3.8E-16 (13)	1.7 (13)						2
Ignimbrite, welded (lithic and pumice lithofacies)	1.59 ± 0.046	34					1490 ± 70	790 ± 60		3
Ignimbrite, welded (lithic and pumice stratified lithofacies)	1.44 ± 0.056	31					2150 ± 130	1250 ± 150		3
Volcaniclastic rocks	2.86 ± 0.15 (668)								0.34 ± 0.10 (16)	6
Andesite	2.64 (210)	4 (31)	6E-18 (46)	1.68 (50)		750 (28)	4589 (34)		13.92 (41)	5
Andesite	2.37 (24)	9.52 (24)	4E-17 (24)	1.32 (24)		740 (24)				1
Andesite	2.27 ± 0.37 (57)	17.3 ± 12.7 (57)		1.08 ± 0.30 (57)	0.61 ± 0.10 (57)	783 ± 79 (57)				7
Basalt		11.8 ± 9.6 (15)		1.7 ± 0.47 (75)			4730 ± 1160 (75)			4
Intermediate extrusive rocks	2.78 ± 0.10 (280)								1.74 ± 7.13 (1351)	6
Mafic intrusive rocks	2.89 ± 0.12 (1384)								8.51 ± 25.7 (2747)	6
Rhyolite				2.84 ± 0.16 (63)			4220 ± 470 (63)			4
Sedimentary rocks	2.75 ± 0.10 (1384)								1.59 ± 7.52 (1408)	6
Medium sandstone		15 ± 4.5 (219)		2.5 ± 0.37 (349)			2930 ± 570 (349)			4
Limestone		3 ± 1.3 (45)		2.45 ± 0.22 (108)			5030 ± 730 (108)			4
Dolomite		2.4 ± 1.6 (22)		2.68 ± 0.1 (24)			5140 ± 1120 (24)			4
Marble				2.84 ± 0.17 (38)			3180 ± 0.99 (38)			4
Metamorphic rocks	2.78 ± 0.13 (1825)								3.44 ± 13.48 (1111)	6
Granite	2.62 ± 0.08 (238)	1.93 ± 1.59 (233)		2.74 ± 0.42 (293)	1.44 ± 0.28 (292)		4711 ± 1116 (225)	2623 ± 679 (225)		8
Granite	2.66 ± 0.07 (666)								1.91 ± 3.52 (344)	6
Granodiorite	2.69 ± 0.07 (296)	1.82 ± 1.88 (262)		2.48 ± 0.36 (394)	1.22 ± 0.19 (386)		4489 ± 975 (284)	2541 ± 561 (284)		8

Arithmetic mean values in normal font, ± = standard deviation, () = number of analyzed samples, ρ_B = bulk density, ϕ = porosity, K = permeability, λ = thermal conductivity, α = thermal diffusivity, V_P = P-wave velocity, V_S = S-wave velocity, cp = specific heat capacity, X = magnetic susceptibility

linear trend. This becomes important when upscaling the parameters to reservoir scale. For example, Farqhuarson et al. (2015) defined a critical porosity threshold beneath which the fluid flow is predominantly restricted to small microcracks. With higher vesicular porosity (> 14–16%) the fluid flow is mainly pore controlled. In general, the investigated rock types of the pre-volcanic basement exhibit data for most parameters in a similar range compared with literature (Table 1). However, especially mineralogical differences can impact bulk density and thermal conductivity (Weinert et al. 2021; Weydt et al. 2018a). For example, thermal conductivity of marble, limestone and dolomite presented in Mielke et al. (2017) are significantly lower compared to the results in this study or Weydt et al. (2018a). While the assumption of rock properties based on literature data might be sufficient for preliminary assessments and numerical models, it cannot account for site-specific depositional environments in sedimentary rocks (Sass and Götz 2012, Aretz et al. 2016), diagenesis (Homuth et al. 2015; Weydt et al. 2018a), hydrothermal and metamorphic overprints (Mielke et al. 2016; Heap et al. 2020a) and their impact on the rock properties.

The here presented rock properties are well in line with data obtained on the few available wellbore core samples of the Los Humeros geothermal field (Weydt et al. 2021a). For example, particle density, bulk density, matrix porosity as well as magnetic susceptibility of the marble wellbore core samples ($n = 3$) representing the upper section of the carbonatic basement in the geothermal reservoir are in the same range compared to the marbles retrieved from outcrops in Las Minas. However, the wellbore core samples exhibit increased matrix permeabilities (10^{-14} m^2) and reduced sonic wave velocities (p-wave velocity = ~ 2600 m s^{-1}, s-wave velocity = ~ 1500 m s^{-1}) due to numerous fractures. Likewise, wellbore core samples retrieved from the andesitic units were affected by fracturing, brecciation and hydrothermal alteration of different intensities resulting in increased hydraulic properties, but reduced bulk densities and sonic wave velocities. Thereby, hydrothermal alteration is commonly restricted to fractures and the alteration intensity often varies on the cm-scale.

The majority of the wellbore core samples were retrieved in close proximity to fault zones. Depending on the scale, accuracy and future application, the observed differences in the physiochemical behavior of the reservoir formations need to be considered during parametrization of a reservoir model. For local, small-scaled reservoir models (e.g., drill path or fault zones) with a high resolution (grid size) the usage of the wellbore core data would be favorable, whereas for large-scaled regional models with a large grid size the usage of this data would significantly overestimate, e.g., matrix porosity and permeability and probably lead to false interpretations and numerical calculations.

Variability and probability density

Deterministic approaches in numerical 3D models are not suitable to capture the intrinsic variability of a rock mass since they commonly assign a single mean value only (Heidarzadeh 2021). In order to deal with the heterogenous nature of rock formations, probability methods are common tools to express and address their variability and uncertainty. Probability density functions (pdfs) are commonly used in stochastic assessments and determined using the mean value and standard deviation of a parameter.

Thereby, pdfs represent the likeliness of each parameter value in the unit and provide a quantitative description of the state of knowledge and uncertainty of our data (the higher and narrower the peaks, the higher the probability; Takahashi 2000). With the help of the previously determined relationships between rock properties pdfs are often used to model other properties and to quantify their uncertainty (Scott et al. 2019).

In order to directly compare the variability and probability distribution of the different lithostratigraphic units, pdfs were calculated (Fig. 10). Since it was not possible to investigate each unit to the same extent due to the complex geological setting and the resulting sample availability, Monte Carlo simulations of the parameters with 1000 random iterations were run using Microsoft Excel 2019. Pdfs were calculated by fitting a normal or beta distribution depending on the outcome of normality and lognormality tests. The majority of the investigated parameters can be depicted with a normal distribution. In a few cases, the data showed a non-normal distribution, e.g., for matrix porosity of the Cretaceous limestones, skarns or granitoids. In these cases, a beta distribution represented the best fit. Figure 10 shows that the probability not only differs between the different units, but also between the parameters within a unit. For example, the pdfs of bulk density and porosity of the Cretaceous limestones show a high and narrow peak (Fig. 10a and b) and thus, high probability. However, the pdfs of the same unit for thermal conductivity and p-wave velocity show a much broader shape compared to the remaining units suggesting a much higher uncertainty. Likewise, a high variability and uncertainty needs to be considered for the porosity and bulk density of the Xáltipan ignimbrite in future modeling applications. In some cases, the pdfs of different units overlap, e.g., the pdfs of bulk density or p-wave velocity of the Teziutlán andesites and granitoids.

The normal distribution is commonly chosen for simplification reasons or in cases with limited information (Adams 2005, Takahashi 2000). However, the results indicate that the data distribution cannot be generalized for a parameter or a reservoir unit and should be tested prior modeling whenever frequency distributions of input parameters are available to avoid parameter overestimations or underestimations. Likewise, uncertainty should be addressed for each unit and parameter. Stochastic approaches are commonly used for geotechnical assessments (Sari 2009; Contreras et al. 2018; Heidarzadeh et al. 2021), processing of geophysical data and modeling (Scott et al. 2019) to address the natural variability of the reservoir formations and geological features as well as to overcome the problem with limited available in situ data. However, it has to be emphasized that the pdfs are biased by the quality of input data. Although more advanced techniques like the Markov Chain Monte Carlo method or Bayesian approach (Contreras et al. 2018) try to overcome lacking information in the input data, the lithological heterogeneities need to be addressed properly during field work and laboratory analyses before modeling.

Prediction of reservoir properties

The petrophysical data presented in this study were determined under standardized laboratory conditions to ensure the reproducibility of the measurements and the comparability between the samples and different rock types. Consequently, the data do not reflect in situ conditions such as high fluid and reservoir temperatures, high overburden stress or fluid composition at reservoir depth. Hydraulic properties such as porosity

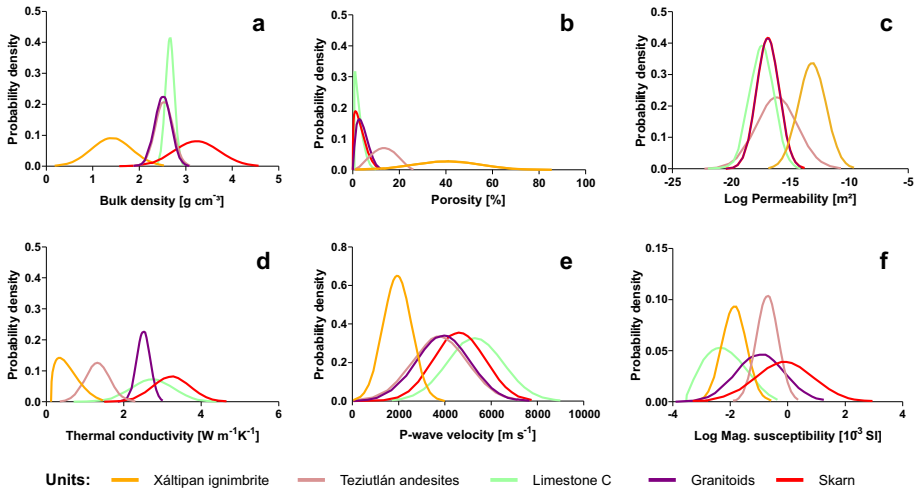

Fig. 10 Probability density functions of selected units (cf. Figure 6) for bulk density (**a**), porosity (**b**), permeability (**c**), thermal conductivity (**d**), p-wave velocity (**e**) and magnetic susceptibility (**f**)

and permeability are sensitive to pressure changes, particularly for soft volcanic rocks. They tend to decrease with increasing pressure at reservoir depth due to consolidation of the rock mass and by closing of fractures (Zimmermann et al. 1986; Jiang et al. 2010; Ashena et al. 2020). The decrease in porosity and the closure of fractures often results in increased bulk density, thermal conductivity, electric resistivity and sonic wave velocities (Clauser and Huenges 1995; Schön 2015). However, with increasing temperature thermal expansion of minerals can cause micro-fracturing, which increases matrix porosity and permeability, but might in turn reduce thermal conductivity, sonic wave velocities or rock strength (Heap et al. 2014a; Vinciguerra et al. 2005). Several physical models, empiric or semi-empiric equations have been developed in the past to predict reservoir conditions (Weydt et al. 2021a). To account for temperature- and pressure-dependent changes on the properties, the measured data were transferred to reservoir conditions using the temperature data of well H8 as an example of the central part of the Los Humeros geothermal field with temperatures of ~ 300 °C at 2 km depth. The thickness of the reservoir units was estimated based on lithostratigraphic well logs and their interpretation used in the preliminary 3D geological model of the Los Humeros geothermal field presented in Calcagno et al. (2020). In this paper, the authors defined four units for the regional 3D model and nine units for the local 3D model of the Los Humeros geothermal field (Table 2). Changes in porosity with reservoir depth were determined after Ashena et al. (2020) based on Athy's law (Athy 1930) by calculating the rock compressibility for each individual unit:

$$\phi = \phi_0 e^{-cf \cdot z}, \tag{1}$$

where ϕ_0 is the initial porosity at zero overburden pressure, *cf* is the formation compaction or compressibility calculated for each individual unit and z is the reservoir depth. Subsequently, changes in matrix permeability were calculated based on the changes in porosity after Wang et al. (2016) using the Carman–Kozeny equation as shown in Eq. 2:

Table 2 Rock properties transferred to reservoir conditions of the Los Humeros geothermal field

Lithology	Model unit*	M [m]	P [MPa]	T [°C]	ϕ [%]	K [m^2]	ρB sat [g cm^{-3}]	λ sat [W m^{-1} K^{-1}]	α sat [10^{-6} m^2 s^{-1}]	Cp sat [J kg^{-1} K^{-1}]	VHC sat [J m^3 K^{-1}]	V_P sat [m s^{-1}]	V_S sat [m s^{-1}]
Undefined pyroclastic deposits	U1	50	≤ 0.93	15–67	41.1–40.5	2.4E-13–2.2E-13	1.89	0.52–0.57	0.27–0.28	2245–2268	3028–3100	2667–2703	1070–1106
Rhyodacite, andesite, basalts	U2	200	0.93–5.56	67–179	15.9–15.6	1.2E-15–8.2E-16	2.37–2.36	0.93–0.97	0.50–0.42	1379–1471	2530–2674	5184–5649	3156–3621
Rhyodacite and Zaragoza ignimbrite	U3	150	5.56–8.85	179–210	21.0–20.7	2.8E-15–2.6E-15	2.24	0.99	0.59–0.57	1658–1689	2726–2742	4489–4528	2783–2822
Faby tuff and andesites	U4	100	8.85–11.04	210–240	20.7–20.5	2.6E-15–2.5E-15	2.24–2.23	0.99–0.97	0.57–0.55	1689–1736	2742–2764	4528–4512	2822–2806
Xaltipan ignimbrite	U5	450	11.04–20.48	240–255	36.4–15.5	4.2E-14–9.9E-15	1.75–2.14	0.60–1.27	0.41–0.72	2339–1569	2787–2387	2355–3330	1352–1966
Teziutlán andesites (30% porous and 70% nonporous lava)	U6	1150	20.48–49.63	255–310	6.81–6.68	7.1E-17–7.0E-17	2.58	1.37–1.33	0.56–0.52	1227–1318	2668–2758	6179–6406	4022–4248
Basement (until 3 km depth, 80% marble, 10% granites and 10% skarn)	U9	1000	49.63–73.58	310–340	1.80–1.81	6.41E-18–6.42E-18	2.72–2.71	2.36–2.38	1.03	1170–1214	2994–3038	7832–7948	4998–5114

*Classification after Calcagno et al. (2020), (weighted) arithmetic mean values in normal font, ρ_B = bulk density, ϕ = porosity, K = permeability, λ = thermal conductivity, α = thermal diffusivity, V_P = p-wave velocity, V_S = s-wave velocity, cp = specific heat capacity, VHC = volumetric heat capacity, sat = saturated, T = reservoir temperature range, P = calculated overburden pressure range, M = estimated average thickness of the unit

$$K = K_{m0} \cdot \left(\frac{1-\phi_0}{1-\phi}\right)^3 \cdot \left(\frac{\phi}{\phi_0}\right)^3, \tag{2}$$

where K_{m0} is the initial matrix permeability at ambient pressure and temperature. To account for mineralogical changes with temperature, thermal expansion coefficients for the different rock types and their change with temperature were retrieved from Heard and Page (1982) and Konietzky and Wang (2019) and integrated into the porosity equation after Wang et al. (2016).

Available chemical data of reservoir fluids from previous studies (e.g., Tello 2005; Bernard et al. 2011) indicated that total dissolved solid (TDS) contents are low at around 1 g kg^{-1} of solution on average and at about 4 g kg^{-1} at maximum. Given the low TDS contents of the majority of the reservoir fluids, it can be implied that their liquid phase properties will closely match those of pure water properties at given pressure and temperature conditions (IAPWS R15-11 2011; IAPWS R6-95 2016; Zarrouk and Watson 2010; assuming that the fluid state is subcritical), which were used to account for saturated conditions at depth by applying the arithmetic-mean model. For example, bulk density of the reservoir formations was calculated as follows:

$$\rho B = \phi \cdot \rho F + (1-\phi) \cdot \rho P. \tag{3}$$

with ρB = bulk density at reservoir depth, ρF = fluid density for the respective temperature and pressure conditions, ρP = particle density of the rock matrix, and ϕ = porosity at reservoir depth. Then, the overburden pressure was obtained by simple gravitational modeling using the previously calculated in situ bulk density and formation thickness multiplied by gravity acceleration. The effect of temperature on specific heat capacity was determined according to Vosteen and Schellschmidt (2003) who provide empirical temperature-correction functions for magmatic, metamorphic and sedimentary rocks. Likewise, thermal conductivity of the majority of rock types was corrected for reservoir temperature after Vosteen and Schellschmidt (2003). The exception forms the highly porous volcanic rocks, such as ignimbrites with very low thermal conductivities, which were corrected on the basis of laboratory experiments presented in Chen et al. (2021). Pressure corrections of the resulting thermal conductivities were applied after Abdulagatov et al. (2006), Abdulagatova et al. (2009). To adapt thermal diffusivity to reservoir conditions, temperature-correction functions after Durham et al. (1987) for volcanic rocks and Vosteen and Schellschmidt (2003) for the remaining rock types were applied. Pressure has only a minor effect on thermal diffusivity of rocks (≤ 0.05–$0.1 \cdot 10^{-6}$ mm s^{-1} for a pressure change of 50 MPa in gabbros, granites and basalts; Durham et al. 1987) and laboratory experiments are scarce. Therefore, the influence of pressure on thermal diffusivity was neglected in this study. Temperature and pressure dependencies of p-wave and s-wave velocities were calculated after experimental data from Qi et al. (2020; carbonates), Vinciguerra et al. (2005, tuff), Hughes and Maurette (1957) and Birch (1961; magmatic and intrusive rocks). Additional information is presented in Appendix B.

The effect of pressure or temperature on selected hydraulic, thermal and dynamic mechanical properties is shown in Fig. 11. Matrix porosity decreases exponentially with increasing depth for the highly porous ignimbrites and fall out deposits, which

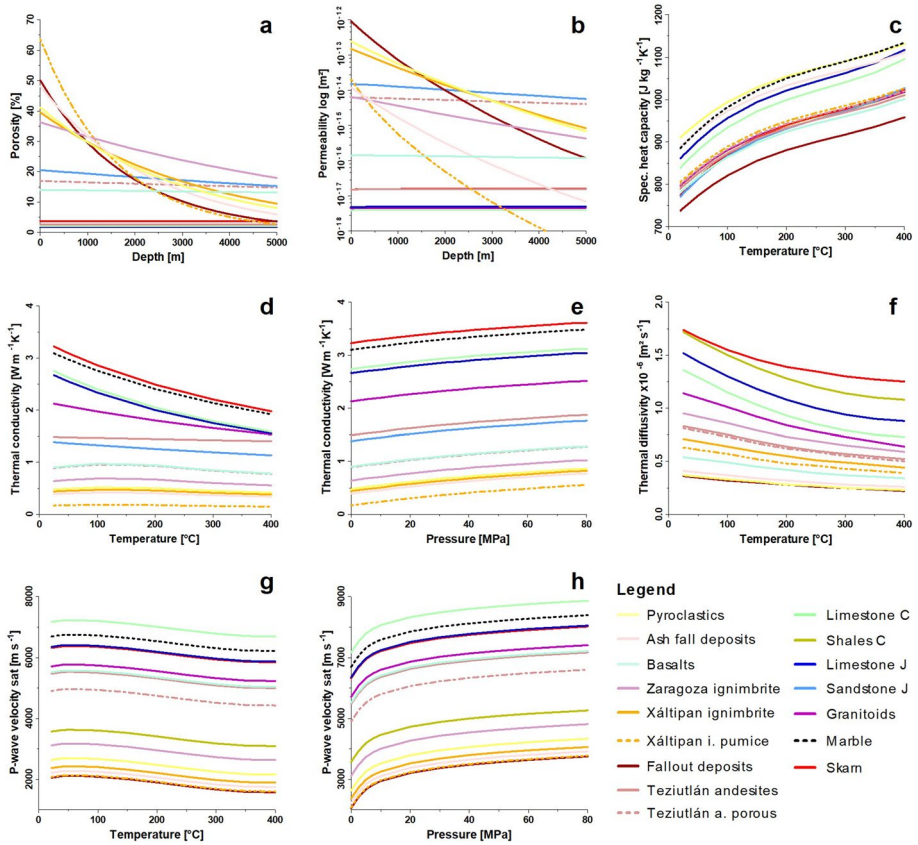

Fig. 11 Depth correction of porosity **a** and matrix permeability **b**, temperature correction of specific heat capacity, thermal conductivity, thermal diffusivity and p-wave velocity (**c**, **d**, **f**, **g**) as well as pressure correction of thermal conductivity and p-wave velocity in **e** and **h**

also contain the highest calculated rock matrix compressibility (~ 10^{-4} PSI). Already at about 1000 m depth, the porosity of the Xáltipan ignimbrite pumice layers would be halved, while the porosity of the Zaragoza ignimbrite would be reduced by about 5% (Fig. 11a). The large changes in porosity of the ignimbrites and ash fall deposits is commonly the result of inelastic compaction due to cataclastic pore collapse, which can occur at very low threshold pressures (Heap et al. 2014b; Vinciguerra et al. 2006), and thus, affect the rock properties already at relatively shallow reservoir depth. Reported UCS values for the Xáltipan ignimbrite range between 2 and 6 MPa for pumice fallouts and ~ 10–45 MPa for the non-welded to partially welded facies (Weydt et al. 2021a). The porous Teziutlán andesite lavas, basalts and Jurassic sandstones show a steady, but small decrease in porosity with depth. In contrast, the porosity of the low-porous sedimentary, intrusive and metamorphic rocks remains almost constant. The comparatively small porosity reductions in the units with very low-to-intermediate porosity are predominantly caused by the closure of microfractures (elastic compaction, Zimmermann et al.

1986). As previously described, detailed investigations of the different lithofacies in the field in combination with laboratory experiments are necessary to accurately estimate matrix porosity and fluid properties at reservoir depth.

Since the change in matrix permeability was calculated after Wang et al. (2016) using the results of the matrix porosity, the same trends can be observed (Fig. 11b). The influence of thermal expansion on matrix porosity and permeability is very small (predominantly < 1% until 350 °C) and thus, might be neglectable for the selected temperature and depth range.

Specific heat capacity significantly increases by about ~ 25–30% (Fig. 11c) with reservoir temperature based on the empirical equations presented in Vosteen and Schellschmidt (2003). Thermal conductivity and thermal diffusivity of the metamorphic, intrusive and carbonatic rocks decrease up to 45% (skarns, marble and limestones) until 400 °C. However, the increase in pressure, and thus the closure of fractures and the reduction in matrix porosity have the opposite effect on thermal conductivity. Pressure and temperature changes of the p-wave velocities determined after Qi et al. (2020) and Hughes and Maurette (1957) are presented in Fig. 11g and h. Thereby, the increasing effect of pressure on the sonic wave velocities predominates the decreasing effect of temperature and thus, the effect of thermal expansion and microcracking.

Table 2 comprises the rock properties at saturated conditions transferred to reservoir pressure and temperature (here ≤ 3 km depth) for the individual lithostratigraphic units which were classified into local model units after Calcagno et al. (2020). The determined overburden pressure reaches ~ 74 MPa at 3 km depth. The formation thickness represents the average thickness of the individual units within the geothermal reservoir based on lithostratigraphic well logs and their interpretation presented in Calcagno et al. (2020). However, the well logs do not always provide detailed thickness estimations for each lithology and rather provide classifications of lithostratigraphic groups that are composed of different rock types. Therefore, the assigned properties for the model units in part represent weighted averages reflecting the estimated contributions of the different rock types within each unit. For example, the alternating lavas and pyroclastic deposits of unit 2 (Table 2) were estimated containing 60% basaltic to andesitic lavas, 20% dacites to rhyolitic lavas and 20% tuff. Furthermore, the units 3 and 4 were estimated containing about 50% pyroclastic deposits and 50% lavas each and the precaldera andesitic lavas were estimated containing about 30% porous and 70% massive lavas based on the results of the only available sonic log (Lorenzo-Pulido et al. 2008; Deb et al. 2019). For the parametrization of the Xáltipan ignimbrite, a gradual transition with reservoir depth from unwelded over partially welded to welded was assumed based on petrographic descriptions presented in Cavazos-Álavarez et al. (2020). The carbonatic basement predominantly consists of recrystallized limestones within the Los Humeros geothermal field and a percentage of 10% intrusive rocks and 10% skarns were assumed based on the outcrop investigations and preliminary results of the geophysical surveys. The results presented in Table 2 reveal a highly variable change of the average rock

properties with increasing reservoir depth. Especially the thermal properties are very sensitive to changes in porosity, due to the different thermal properties of water compared to the rock matrix (Zarrouk and Watson 2010) as well as the decreasing volume of fluid with decreasing porosity.

The effects of reservoir temperature and pressure are often only partially considered (Deb et al. 2019) or completely neglected (Cornejo et al. 2020; Kruszewski et al. 2020; Gonzalez-Garcia et al. 2020) during reservoir modeling leading to oversimplified predictions of the reservoir behavior (Norden et al. 2020). For example, the application of correction functions for thermal conductivity without applying a pressure correction leads to significantly underestimated thermal conductivities (Norden et al. 2020). Commonly, the thermomechanical behavior of the reservoir formations and their complex interplay with fluid properties, stress, overburden pressure and reservoir temperature are commonly solved numerically. The usage of empirical and analytical equations already provides a good prediction of the rock properties at reservoir depth, particularly in cases without geophysical well log data. However, since they are commonly based on laboratory experiments performed on sample sets collected from different study areas, they are not able to represent the site-specific fracture pattern, microstructural variability, mineralogy, as well as hydrothermal, diagenetic or metamorphic overprints. Additionally, the majority of high T/P experiments presented in the literature focus on rock types with low to intermediate porosity (e.g., granites, limestones or sandstones). The response to pressure changes of high-porosity rocks can be however fundamentally different compared to low-porous rocks (inelastic vs. elastic compaction; Vinciguerra et al. 2006; Heap et al. 2014b). Up to now, high T/P laboratory tests considering pyroclastic rocks are scarce, particularly for thermal properties, and therefore their behavior under high T/P is not fully understood yet. Thus, for a more precise reservoir property prediction further high T/P experiments would be required for each target unit.

Data application and limitations with respect to modeling the Los Humeros geothermal field

In a previous attempt, a preliminary structural-geological model of Los Humeros was created (Calcagno et al. 2020) and used for simulating the initial state of the super-hot geothermal system (Deb et al. 2019). Due to lack of data at this stage of the project, the classification of the model units was based on the local stratigraphy as presented in Fig. 2 and the parametrization was performed mainly using assumed average values for each unit. However, some of these model units comprise multiple different rock types, which leads to a wide parameter range and high uncertainty during modeling. Based on the presented findings, the following updates are suggested.

The pre-volcanic basement revealed the highest geological heterogeneity and thus, the highest parameter range, e.g., for thermal conductivity. The recharge and fluid flow of the Los Humeros geothermal field are controlled by fault zones and fractures in the carbonatic basement and subsequently in the andesitic reservoir (Lelli et al. 2020).

Furthermore, the heat flow is controlled by shallow intrusions that are nested in the carbonates (Lucci et al. 2020) and potentially even in the upper section of the andesitic unit (Urbani et al. 2020). The intrusions in the carbonates led to the formation of skarn and marble bodies, which attain up to 100 m in width for skarns (Olvera-Garcia et al. 2020) and between 300 and 400 m in width for marble (Fuentes-Guzmán et al. 2020) in the exhumed system of Las Minas. With their high thermal conductivities and abundant fractures, they act as heat conduits in the subsurface. To improve the accuracy of a 3D geothermal model, these rather 'vertical features' should be implemented as additional model units in the pre-volcanic basement unit.

While in previous studies the Cuyoaco andesite unit has been assumed to have a thickness of several hundreds of meters in the reservoir (Cedillo 1999; Calcagno et al. 2020), recent petrographic investigations concluded that this unit might have a very limited extension in the subsurface of the Los Humeros geothermal field (Carrasco-Núñez et al. 2017a). However, due to the hydrothermal overprint observed on the wellbore core samples, a clear correlation with the outcropping units or between wells remains challenging. Since the Cuyoaco and Teziutlán andesites exhibit very similar physiochemical characteristics, it seems plausible to merge both pre-caldera andesites in one model unit instead of using stratigraphic ages to define differences.

The Xáltipan ignimbrite represents the cap rock of the Los Humeros geothermal field and resembles the most heterogenous lithostratigraphic unit considering its variable thickness (70–880 m) and petrophysical properties (Figs. 8, 9, 10, 11). Furthermore, especially the basal section of the Xáltipan ignimbrite within the Los Humeros geothermal field were affected by fracturing, brecciation and occasionally by hydrothermal alteration due to the caldera collapse events and volcanic activities during the post-caldera phase (Cavazos-Álavarez et al. 2020; Urbani et al. 2020; Weydt et al. 2021b). In previous studies, the Xáltipan ignimbrite was described as a nonpermeable, rather homogeneous layer (Cedillo 1999), however, the results of the petrographic (Cavazos-Álavarez et al. 2020) and petrophysical characterization have shown that a much higher heterogeneity and thus, uncertainty need to be considered. The remaining units of the caldera and post-caldera group have a thickness of a few meters to tens of meters only. Up to now accurate information about their thickness and lateral distribution are not available for the Los Humeros geothermal field and thus, it is not possible to define further units that exhibit petrophysically similar properties. The interpretation of geophysical data is still ongoing and might provide new insights for an updated 3D geological model of Los Humeros.

The investigation of outcrop analogues and their petrophysical characterization significantly improved the geological understanding of the LHVC and forms the basis for the interpretation of geophysical surveys (e.g., electric resistivity, gravimetric and magnetotelluric surveys; Benediktsdóttir et al. 2020, Cornejo et al. 2020), economical assessments (e.g., productivity index and Heat-in-Place calculations; Gonzalez-Garcia et al. 2020), the estimation of the local stress field (Kruzewski et al. 2020), an accurate

assessment of the heat transport and heat storage in the reservoir as well as a precise parametrization of numerical reservoir models to simulate, e.g., reservoir temperature (Deb et al. 2019) or production and stimulation scenarios (Hofmann et al. 2021).

However, despite the high number of analyzed samples, it was not possible to cover all units to the same extent in the study area. The number of samples per unit strongly depended on the availability and accessibility of representative outcrops in the field that allowed to gain a representative overview of the unit's heterogeneity and to collect large boulders for the petrophysical characterization. In addition, the number of samples per unit was influenced by the project goals, which targeted the currently exploited hydrothermal reservoir (pre-caldera units) and the potential supercritical reservoir (pre-volcanic basement). Thus, a further criterion was the importance of a unit with respect to a 3D geological model considering the thickness and extension in the study area.

Furthermore, the here presented data set comprises matrix properties only and does not account for fracture properties, which can vary over several orders of magnitude for different scales. For example, matrix permeabilities commonly underestimate the equivalent permeability at reservoir scale since they do not depict fracture networks and their permeabilities (Heap and Kennedy 2016; Farquharson and Wadsworth 2018). Depending on the aim and scale of future applications, the data need to be individually processed, which is also called upscaling. Various different approaches have been developed in the past to tackle the problem of retaining as much information of the original structure, facies heterogeneities, geometry, petrophysical and hydraulic properties on reservoir scale (Farmer 2002; Qi and Hesketh 2005; Rühaak et al. 2015; Chen et al. 2018, Ringrose and Bentley 2021). The simplest and fastest techniques are cross-correlations or (power law) averaging (calculating the arithmetic, harmonic or geometric mean value of a respective volume; weighted sum of an independent property), which is often applied in combination with stochastic techniques, e.g., the Monte Carlo method (Qi and Hesketh 2005). More advanced approaches such as variogram analysis, Kriging or Gaussian simulations are often used to populate numerical models of geologically complex and/or fractured reservoirs (Bourbiaux et al. 2005; Ebong et al. 2019). Furthermore, Discrete Fracture Networks or dual porosity/permeability models allow to explicitly represent fractures and their geometries in reservoir simulations (Ringrose and Bentley 2021). In conclusion, numerous upscaling techniques exist, which need to be chosen carefully for each parameter considering the geological setting, rock type and application.

Conclusions

This study provides an assessment of petrophysical, thermophysical, dynamic mechanical as well as magnetic rock properties for the Los Humeros Volcanic Complex which hosts a currently exploited high-temperature (> 350 °C) geothermal reservoir. For a reliable reservoir characterization, 226 samples were collected from more than 200 outcrops in the inside of the Los Humeros caldera, the surrounding area of the volcanic complex and the nearby exhumed system of Las Minas to investigate and cover the heterogeneity of all key formations from the basement to the cap rock that are relevant for regional and local 3D numerical geothermal models of the Los

Humeros geothermal field. Based on chemical and petrographic analyses as well as new information on dating, the samples were assigned to lithostratigraphic units. About 1500 plugs were petrophysically analyzed resulting in an extensive rock property database covering sedimentary, magmatic and metamorphic rocks from Jurassic to Holocene age. The distribution and variability of the petrophysical properties as well as the relationship between the parameters were statistically investigated and displayed for each lithostratigraphic unit. For a more reliable reservoir characterization, the rock properties were transferred to reservoir conditions of the Los Humeros geothermal field of up to 3 km depth using empiric and analytical correction functions.

The study highlights the geological complexity of the study area which is also depicted in the petrophysical properties:

- More than 20 lithostratigraphic units and subunits were defined that exhibit distinct properties. The basement and andesitic reservoir predominantly comprise low-to-very low matrix porosities and permeabilities as well as intermediate-to-high densities, thermal properties and sonic wave velocities.
- The weak correlation between matrix porosity and permeability suggests that fluid flow in the study area is predominantly controlled by faults.
- The high variability of thermal conductivity and diffusivity observed on the basement rocks should be considered in future thermal models, whereby intrusions and their associated metamorphic rocks might act as heat conduits.
- The cap rock and the overlying younger volcanic sequences show the highest variability with respect to matrix porosity and bulk density, but feature overall low-to-intermediate thermal conductivities and sonic wave velocities.
- Specific heat capacity shows comparatively small variations throughout the dataset. In contrast, magnetic susceptibility varies over more than four orders of magnitude showing formation-related trends that could be helpful for the interpretation of geophysical surveys.
- Rock properties are sensitive to pressure and temperature changes with increasing reservoir depth. Particularly, matrix porosity and permeability of the pyroclastic rocks significantly decrease with reservoir depth due to their high rock compressibility. The effects of pressure and temperature on the thermal and mechanical properties are complex and often counteract each other. Thus, correction functions for both parameters should be considered in numerical simulations to depict the rock properties at reservoir depth as accurate as possible.
- Furthermore, the probability density distribution should be assessed for each parameter and unit individually during stochastic modeling.

The dataset provided in this study improves the understanding of the Los Humeros Volcanic Complex and super-hot geothermal systems in general, and underlines the importance of outcrop analogue studies and the assessment of petrophysical properties during reservoir exploration for the development of conceptual geological models, the interpretation of geophysical data or the parametrization of 3D numerical geothermal models. Beyond the scope of the GEMex project, the level of detail presented in this study facilitates various applications in comparable geological settings within the TMVB

or similar volcanic geothermal play types worldwide. Since extensive field campaigns and laboratory measurements are time consuming and often exceed project budgets, our study improves the prediction of rock properties in the subsurface at early exploration stages or in case of low data densities and thus, could be used to improve and speed-up reservoir simulation of future projects.

Appendix A petrophysical database

See Figs. 12, 13 and Tables 3, 4, 5 and 6.

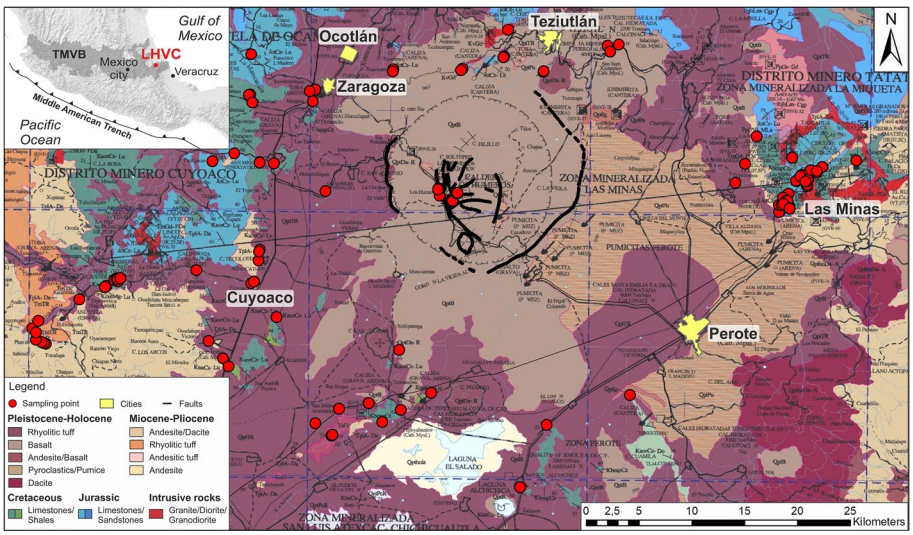

Fig. 12 Regional geological setting with the Los Humeros Volcanic Complex in the center (SGM, 2002). The red circles represent the sampling points of the outcrop samples investigated in this study

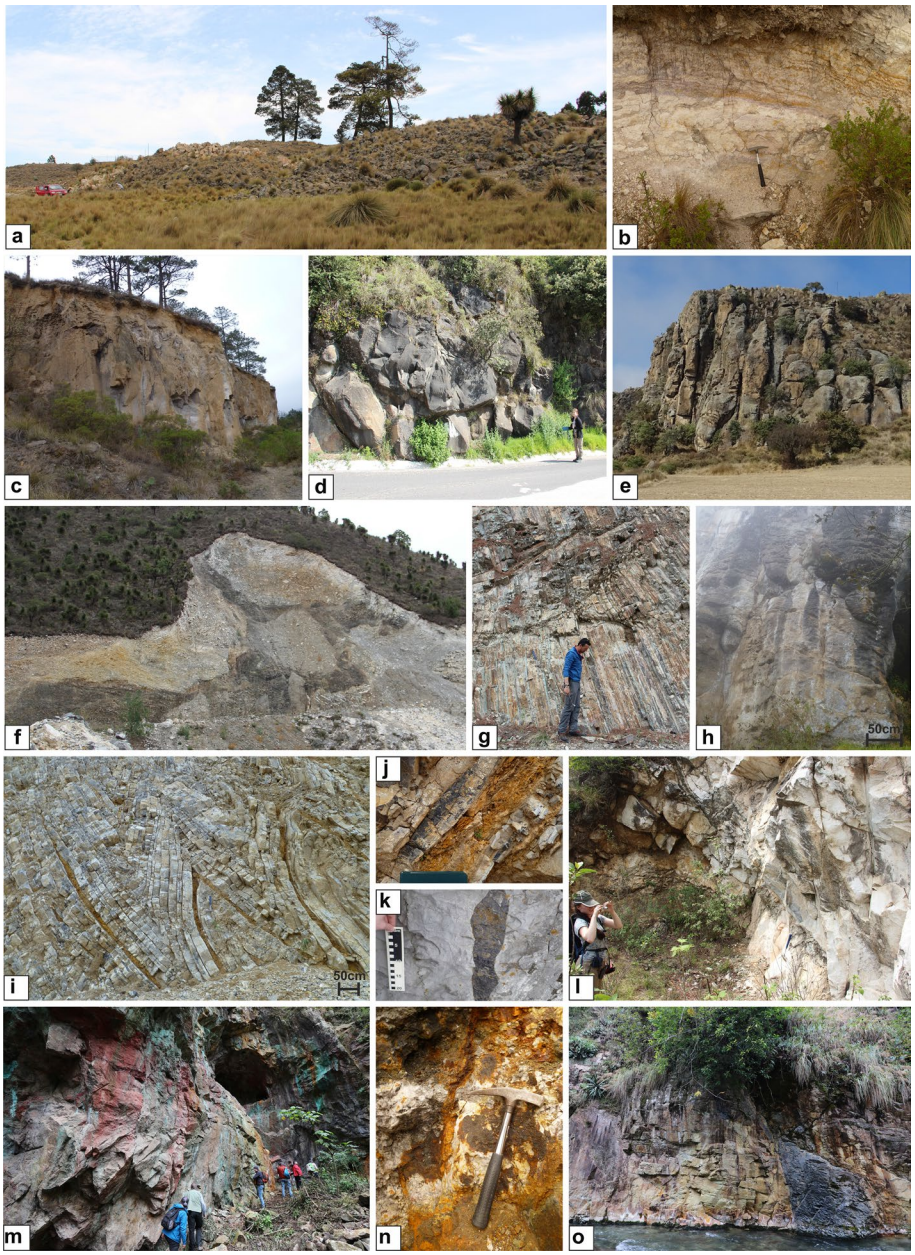

Fig. 13 Photographs of selected outcrops representing **a** Holocene basaltic lava flows and **b** ash deposits of the Xoxoctic member inside of the Los Humeros caldera, **c** unwelded Xáltipan ignimbrite located northwest of the LHVC close to the town Temextla, **d** the Teziutlán andesite unit located east of the LHVC, **e** the Cuyoaco andesite unit located west of the LHVC, **f** andesitic dykes intruding into Cretaceous limestones located southwest of the LHVC (road cut), **g** Cretaceous shales, **h** Jurassic sandstone deposits, **i**–**k** Cretaceous limestones, marl and chert layers as well as chert nodules, **l** Miocene marbles, **m** skarn deposits of the Eldorado mine, **n** quartz veins associated with skarn deposits and **o** a granitic intrusion cut by a mafic dyke in a riverbed (**l**–**o** represent outcrops in Las Minas)

Table 3 Petrophysical and hydraulic properties of the LHVC

Unit	ρ_P [g cm^{-3}]	ρ_B [g cm^{-3}]	ϕ [%]	K [m^2]
Post-caldera group				
Pyroclastics, undifferentiated	2.51/**2.52** (6) ± 0.03 Q1: 2.47, Q3: 2.53 CV: 1.15%	1.48/**1.48** (6) ± 0.03 Q1: 1.45, Q3: 1.51 CV: 2.32%	41.1/**41.0** (6) ± 1.3 Q1: 39.8, Q3: 42.4 CV: 3.24%	2.4E-13/**2.3E-13** (4) ± 4.7E-14 Q1: 2.1E-13, Q3: 2.9E-13 CV: 19.03%
Basalts	2.65/**2.67** (40) ± 0.10 Q1: 2.62, Q3: 2.72 CV: 3.9%	2.28/**2.33** (28) ± 0.18 Q1: 2.14, Q3: 2.42 CV: 8.01%	14.0/**12.3** (28) ± 5.4 Q1: 10.5, Q3: 17.5 CV: 38.65%	6.7E-14/**2.5E-17** (27) ± 1.9E-13 Q1: 5.8E-18, Q3: 8.4E-15 CV: 291.46%
Ash fall deposits	2.36/2.36 (6) ± 0.04 Q1: 2.31 Q3: 2.38 CV: 1.78%	1.23/**1.19** (6) ± 0.13 Q1: 1.17, Q3: 1.27 CV: 10.81%	48.1/**49.8** (6) ± 4.7 Q1: 46.1, Q3: 50.6 CV: 9.82%	1.3E-14/**1.1E-14** (5) ± 2.7E-15 Q1: 1.1E-14, Q3: 1.5E-14 CV: 21.80%
Caldera group				
Zaragoza ignimbrite	2.48/**2.44** (34) ± 0.11 Q1: 2.42, Q3: 2.50 CV: 4.33%	1.60/**1.56** (23) ± 0.18 Q1: 1.48, Q3: 1.58 CV: 11.40%	36.3/**37.1** (23) ± 4.5 Q1: 34.8, Q3: 39.8 CV: 12.32%	4.7E-14/**8.8E-15** (19) ± 8.8E-14 Q1: 1.7E-15, Q3: 2.3E-14 CV: 188.13%
Xáltipan ignimbrite total	2.28/**2.41** (120) ± 0.34 Q1: 2.25, Q3: 2.49 CV: 15.02%	1.40/**1.33** (64) ± 0.44 Q1: 1.24, Q3: 1.72 CV: 31.01%	40.9/**42.9** (64) ± 14.5 Q1: 31.0, Q3: 50.1 CV: 35.46%	2.5E-13/**1.7E-13** (59) ± 2.6E-13 Q1: 3.3E-14, Q3: 4.1E-13 CV: 103.68%
Xáltipan ig. (unaltered)	2.40/**2.43** (93) ± 0.10 Q1: 2.36, Q3: 2.49 CV: 4.25%	1.47/**1.34** (53) ± 0.23 Q1:1.28, Q3: 1.72 CV: 15.71%	39.5/**38.4** (53) ± 9.5 Q1: 31.0, Q3: 47.7 CV: 23.92%	2.8E-13/**1.7E-13** (50) ± 2.7E-13 Q1: 3.9E-14, Q3: 5.2E-13 CV: 96.38%
Xáltipan ig. (pumice)	1.51/**1.50** (18) ± 0.15 Q1: 1.40, Q3: 1.61 CV: 9.86%	0.56/**0.56** (8) ± 0.06 Q1: 0.51, Q3: 0.59 CV: 9.92%	63.5/**61.6** (8) ± 6.9 Q1: 57.8, Q3: 70.6 CV: 10.87%	1.6E-13/**1.3E-13** (6) ± 1.8E-13 Q1: 1.7E-15, Q3: 3.1E-13 CV: 111.85%
Xáltipan ig. (altered, welded)	2.52/**2.52** (9) ± 0.03 Q1: 2.49, Q3: 2.53 CV: 1.03%	2.42/**2.42** (3) ± 0.01 Q1: 2.41, Q3: 2.43	4.1/**4.5** (3) ± 1.9 Q1: 2.1, Q3: 5.9	6.0E-18/**4.3E-18** (3) ± 3.2E-18
Pre-caldera group				
Cinder cones total	2.80/**2.81** (15) ± 0.05 Q1: 2.77, Q3: 2.83 CV: 1.64%	1.82/**1.98** (7) ± 0.32 Q1: 1.60, Q3: 2.03 CV: 17.72%	35.5/**30.1** (7) ± 11.0 Q1: 28.3, Q3: 42.4 CV: 31.1%	3.9E-13/**2.3E-14** (5) ± 5.8E-13 Q1: 5.5E-16, Q3: 9.7E-13 CV: 147.54%
Scoria	2.82/**2.83** (11) ± 0.03 Q1: 2.78, Q3: 2.84 CV: 1.11%	2.00/**1.98** (5) ± 0.06 Q1: 1.95, Q3: 2.05 CV: 2.85%	29.7/**29.9** (5) ± 2.2 Q1: 27.7%, Q3: 31.5 CV: 7.54%	7.9E-15/**1.1E-15** (3) ± 1.3E-14
Fallout deposits	2.75/**2.75** (4) ± 0.04 Q1: 2.71, Q3: 2.79	1.39 (2) ± 0.30	50.0 (2) ± 10.8	9.7E-13 (2) ± 4.8E-13
Teziutlán andesite unit total	2.72/**2.72** (142) ± 0.06 Q1: 2.69, Q3: 2.74 CV: 2.07%	2.53/**2.60** (131) ± 0.19 Q1: 2.39, Q3: 2.68 CV: 7.44%	6.9/**2.7** (126) ± 7.3 Q1: 1.5, Q3: 13.4 CV: 106.26%	1.0E-14/**4.6E-17** (92) ± 3.0E-14 Q1: 2E-18, Q3: 2.9E-15 CV: 299.72%
Teziutlán and. (nonporous)	2.71/**2.71** (105) ± 0.05 Q1: 2.67, Q3: 2.73 CV: 1.96%	2.63/**2.65** (94) ± 0.10 Q1: 2.59, Q3: 2.69 CV: 3.89%	2.7/**2.1** (89) ± 2.5 Q1: 1.1, Q3: 2.9 CV: 92.58%	3.1E-15/**4.3E-18** (68) ± 2.0E-14 Q1:1.7E-18, Q3: 8.2E-17 CV: 627.69%
Teziutlán and. (porous)	2.76/**2.75** (37) ± 0.04 Q1: 2.74, Q3: 2.77 CV: 1.53%	2.30/**2.35** (37) ± 0.15 Q1: 2.17, Q3: 2.39 CV: 6.31%	16.9/**14.7** (37) ± 4.6 Q1: 13.4, Q3: 21.3 CV: 27.21%	3.0E-14/**9.5E-15** (24) ± 4.4E-14 Q1: 7.2E-16, Q3: 5.2E-14 CV: 147.99%
Cuyoaco andesite unit	2.64/**2.65** (50) ± 0.02 Q1: 2.64, Q3: 2.67 CV: 0.87%	2.55/**2.61** (32) ± 0.10 Q1: 2.50, Q3: 2.62 CV: 3.75%	4.0/**1.4** (32) ± 4.1 Q1: 0.9, Q3: 6.6 CV: 100.81%	4.0E-15/**5.1E-18** (26) ± 1.6E-14 Q1: 2.4E-18, Q3: 7.9E-16 CV: 407.02%
Basement				
Limestone Cretaceous	2.67/**2.68** (352) ± 0.05 Q1: 2.65, Q3: 2.70 CV: 1.78%	2.66/**2.68** (232) ± 0.10 Q1: 2.63, Q3: 2.70 CV: 3.61%	2.1/**0.8** (201) ± 3.0 Q1: 0.5, Q3: 2.6 CV: 141.52%	5.3E-16/**3.2E-18** (179) ± 4.4E-15 Q1: 1.1E-18, Q3: 6.9E-18 CV: 825.21%
Chert nodules	2.63/**2.65** (19) ± 0.03 Q1: 2.62, Q3: 2.6 CV: 1.02%	2.63/**2.63** (15) ± 0.04 Q1: 2.60, Q3: 2.65 CV: 1.42%	0.8/**0.8** (14) ± 0.6 Q1: 0.2, Q3: 1.2 CV: 74.50%	5.4E-17/**2.8E-18** (13) ± 1.6E-16 Q1: 2E-18, Q3: 9.5E-18 CV: 303.80%
Shales Cretaceous	2.68/**2.68** (7) ± 0.01 Q1: 2.68, Q3: 2.69 CV: 0.20%	2.66/**2.66** (6) ± 0.01 Q1: 2.66, Q3: 2.67 CV: 0.39%	1.3/**1.1** (6) ± 0.7 Q1: 0.8, Q3: 1.7 CV: 56.95%	1.7E-18/**7.2E-19** (5) ± 1.6E-18 Q1: 4.6E-19, Q3: 3.4E-18 CV: 94.83%
Limestone Jurassic	2.64/**2.66** (39) ± 0.05 Q1: 2.62, Q3: 2.68 CV: 1.98%	2.63/**2.61** (30) ± 0.04 Q1: 2.59, Q3: 2.68 CV: 1.69%	1.8/**1.1** (29) ± 1.6 Q1: 0.8, Q3: 2.6 CV: 88.61%	1.5E-15/**2.1E-18** (24) ± 5.7E-15 Q1: 8.1E-19, Q3: 9.2E-18 CV: 388.40%

Table 3 (continued)

Unit	ρ_P [g cm^{-3}]	ρ_B [g cm^{-3}]	ϕ [%]	K [m^2]
Sandstone Jurassic	2.64/**2.65** (7) ± 0.02 Q1: 2.64, Q3: 2.66 CV: 0.63%	2.07/**2.08** (6) ± 0.08 Q1: 2.02, Q3: 2.13 CV: 3.77%	20.5/**20.4** (6) ± 1.8 Q1: 19.3, Q3: 21.8 CV: 8.74%	8.1E-13/**3.2E-14** (7) ± 2.0E-12 Q1: 1.8E-16, Q3: 2.7E-13 CV: 243.80%
Basaltic—andesitic dykes	2.66/**2.65** (26) ± 0.19 Q1: 2.58, Q3: 2.95 CV: 6.85%	2.68/**2.57** (22) ± 0.21 Q1: 2.56, Q3: 2.93 CV: 7.73%	1.6/**1.0** (22) ± 2.1 Q1: 0.7, Q3: 2.0 CV: 128.04%	5.6E-18/**3.7E-18** (16) ± 4.5E-18 Q1: 2.3E-18, Q3: 8.8E-18 CV: 79.44%
Marble	2.72/**2.71** (69) ± 0.10 Q1: 2.69, Q3: 2.85 CV: 3.59%	2.70/**2.69** (69) ± 0.11 Q1: 2.63, Q3: 2.80 CV: 4.06%	1.5/**0.8** (79) ± 1.7 Q1: 0.5, Q3: 1.8 CV: 117.27%	2.5E-15/**2.5E-18** (48) ± 1.2E-14 Q1: 1.1E-18, Q3: 6E-18 CV: 467.41%
Quartz veins	2.63/**2.64** (20) ± 0.03 Q1: 2.62, Q3: 2.69 CV: 1.10%	2.53/**2.57** (19) ± 0.09 Q1: 2.51, Q3: 2.58 CV: 3.64%	3.5/**2.8** (19) ± 3.0 Q1: 1.5, Q3: 4.3 CV: 85.60%	1.5E-14/**4.5E-15** (10) ± 2.2E-14 Q1: 2.5E-16, Q3: 2.7E-14 CV: 151.63%
Skarn	3.19/**3.32** (142) ± 0.51 Q1: 2.73, Q3: 3.69 CV: 15.53%	3.23/**3.26** (111) ± 0.49 Q1: 2.71, Q3: 3.57 CV: 15.14%	3.7/**2.4** (115) ± 3.9 Q1: 0.8, Q3: 4.5 CV: 103.87%	8.4E-13/**9E-18** (90) ± 8.0E-12 Q1: 2.5E-18, Q3: 4E-17 CV: 948.01%
Granitoids total	2.64/**2.65** (124) ± 0.12 Q1: 2.61, Q3: 2.67 CV: 4.39%	2.51/**2.52** (73) ± 0.18 Q1: 2.35, Q3: 2.63 CV: 6.99%	6.0/**3.6** (76) ± 4.8 Q1: 1.6, Q3: 10.7 CV: 80.26%	2.6E-16/**7.9E-18** (53) ± 1.4E-15 Q1: 2.7E-18, Q3: 5.8E-17 CV: 539.26%
Granitoids (weak–moderate alteration)	2.65/**2.65** (80) ± 0.12 Q1: 2.63, Q3: 2.68 CV: 4.53%	2.56/**2.59** (52) ± 0.18 Q1: 2.36, Q3: 2.65 CV: 6.91%	1.8/**1.6** (40) ± 1.2 Q1: 0.9, Q3: 2.5 CV: 65.85%	4.0E-17/**3.5E-18** (28) ± 1.2E-16 Q1: 1.2E-18, Q3: 7.7E-18 CV: 300.54%
Granitoids (strong alteration)	2.60/**2.62** (30) ± 0.04 Q1: 2.60, Q3: 2.64 CV: 1.50%	2.38/**2.37** (21) ± 0.07 Q1: 2.36, Q3: 2.42 CV: 2.77%	9.7/**9.7** (21) ± 2.8 Q1: 8.4, Q3: 10.9 CV: 28.68%	2.9E-17/**2.6E-17** (14) ± 2.5E-17 Q1: 4.5E-18, Q3: 4.9E-17 CV: 87.14%

Arithmetic mean values in normal font, the numbers in bold represent the median, ± = standard deviation, () = number of analyzed plugs, Q1: 25% quartile, Q3: 75% quartile, ρ_P = particle density, ρ_B = bulk density, ϕ = porosity, K = permeability

Table 4 Thermal properties of the LHVC

Unit	λ dry [W m^{-1} K^{-1}]	λ sat [W m^{-1} K^{-1}]	α dry [10^{-6} m^2 s^{-1}]	α sat [10^{-6} m^2 s^{-1}]
Post-caldera group				
Pyroclastics, undifferentiated	0.48/**0.50** (4) ± 0.04 Q1: 0.44, Q3: 0.51	1.00/**1.01** (4) ± 0.05 Q1: 0.95, Q3: 1.03	0.37/**0.37** (4) ± 0.02 Q1: 0.35, Q3: 0.39	0.89/**0.89** (4) ± 0.05 Q1: 0.85, Q3: 0.94
Basalts	0.90/**0.92** (33) ± 0.12 Q1: 0.81, Q3: 0.98 CV: 13.77%	1.33/**1.32** (33) ± 0.20 Q1: 1.19, Q3: 1.36 CV: 14.94%	0.54/**0.54** (29) ± 0.05 Q1: 0.51, Q3: 0.57 CV: 8.94%	0.88/**0.85** (29) ± 0.17 Q1: 0.78, Q3: 0.96 CV: 19.13%
Ash fall deposits	0.39/**0.32** (6) ± 0.18 Q1: 0.58, Q3: 0.44 CV: 47.40%	1.16/**1.09** (6) ± 0.21 Q1: 1.04, Q3: 1.22 CV: 18.61%	0.37/**0.37** (5) ± 0.01 Q1: 0.36, Q3: 0.38	0.41/**0.40** (5) ± 0.02 Q1: 0.39, Q3: 0.44 CV: 5.97%
Caldera group				
Zaragoza ignimbrite	0.64/**0.64** (34) ± 0.09 Q1: 0.58, Q3: 0.70 CV: 14.10%	1.31/**1.28** (26) ± 0.18 Q1: 1.19, Q3: 1.39 CV: 13.88%	0.52/**0.51** (32) ± 0.04 Q1: 0.50, Q3: 0.55 CV: 7.24%	0.95/**0.91** (24) ± 0.20 Q1: 0.77, Q3: 1.12 CV: 21.57%
Xáltipan ignimbrite total	0.51/**0.40** (120) ± 0.41 Q1: 0.30, Q3: 0.54 CV: 79.40%	1.19/**1.26** (84) ± 0.34 Q1: 0.99, Q3: 1.40 CV: 28.56%	0.48/**0.47** (117) ± 0.22 Q1: 0.34, Q3: 0.50 CV: 46.12%	0.76/**0.66** (81) ± 0.23 Q1: 0.60, Q3: 0.90 CV: 30.53%
Xáltipan ig. (unaltered)	0.44/**0.41** (98) ± 0.18 Q1: 0.33, Q3: 0.53 CV: 40.30%	1.19/**1.24** (73) ± 0.25 Q1: 1.01, Q3: 1.39 CV: 21.04%	0.43/**0.48** (90) ± 0.10 Q1: 0.33, Q3: 0.50 CV: 22.58%	0.71/**0.66** (70) ± 0.15 Q1: 0.60, Q3: 0.87 CV: 21.21%
Xáltipan ig. (pumice)	0.17/**0.18** (13) ± 0.03 Q1: 0.15, Q3: 0.19 CV: 15.99%	0.47/**0.45** (5) ± 0.06 Q1: 0.43, Q3: 0.52 CV: 13.80%	0.39/**0.42** (18) ± 0.09 Q1: 0.30, Q3: 0.46 CV: 23.29%	0.63/**0.64** (5) ± 0.11 Q1: 0.55, Q3: 0.71 CV: 17.24%
Xáltipan ig. (altered, welded)	1.78/**1.75** (9) ± 0.14 Q1: 1.69, Q3: 1.94 CV: 7.88%	1.83/**1.82** (6) ± 0.07 Q1: 1.77, Q3: 1.91 CV: 3.64%	1.10/**1.27** (9) ± 0.32 Q1: 0.79, Q3: 1.40 CV: 29.14%	1.39/**1.39** (6) ± 0.11 Q1: 0.64, Q3: 1.51 CV: 8.08%

Table 4 (continued)

Unit	λ dry [W m^{-1} K^{-1}]	λ sat [W m^{-1} K^{-1}]	α dry [10^{-6} m^2 s^{-1}]	α sat [10^{-6} m^2 s^{-1}]
Pre-caldera group				
Cinder cones total	0.91/**0.86** (15) ± 0.37 Q1: 0.70, Q3: 1.23 CV: 41.10%	1.62/**1.63** (11) ± 0.09 Q1: 1.53, Q3: 1.70 CV: 5.77%	0.57/**0.61** (15) ± 0.15 Q1: 0.38, Q3: 0.64 CV: 26.81%	0.74/**0.76** (11) ± 0.09 Q1: 0.64, Q3: 0.83 CV: 12.21%
Scoria	1.07/**1.06** (11) ± 0.28 Q1: 0.84, Q3: 1.26 CV: 26.35%	1.62/**1.63** (11) ± 0.09 Q1: 1.53, Q3: 1.70 CV: 5.77%	0.65/**0.64** (11) ± 0.08 Q1: 0.60, Q3: 0.66 CV: 12.95%	0.74/**0.76** (11) ± 0.09 Q1: 0.64, Q3: 0.83 CV: 12.21%
Fallout deposits	0.48/**0.46** (4) ± 0.22 Q1: 0.29, Q3: 0.68	–	0.36/**0.36** (4) ± 0.02 Q1: 0.34, Q3: 0.38	–
Teziutlán andesite unit total	1.32/**1.35** (112) ± 0.32 Q1: 0.99, Q3: 1.61 CV: 24.09%	1.50/**1.52** (112) ± 0.12 Q1: 1.43, Q3: 1.58 CV: 7.67%	0.82/**0.86** (110) ± 0.15 Q1: 0.73, Q3: 0.91 CV: 18.33%	1.10/**1.09** (110) ± 0.16 Q1: 0.99, Q3: 1.18 CV: 14.82%
Teziutlán and. (nonporous)	1.49/**1.56** (80) ± 0.18 Q1: 1.32, Q3: 1.64 CV: 12.36%	1.52/**1.54** (80) ± 0.13 Q1: 1.43, Q3: 1.60 CV: 8.26%	0.83/**0.86** (80) ± 0.10 Q1: 0.77, Q3: 0.89 CV: 12.31%	1.14/**1.14** (78) ± 0.17 Q1: 1.06, Q3: 1.23 CV: 15.27%
Teziutlán and. (porous)	0.89/**0.90** (32) ± 0.10 Q1: 0.82, Q3: 0.97 CV: 11.52%	1.47/**1.48** (32) ± 0.08 Q1: 1.43, Q3: 1.54 CV: 5.14%	0.81/**0.74** (30) ± 0.24 Q1: 0.58, Q3: 1.03 CV: 29.58%	1.00/**1.00** (32) ± 0.06 Q1: 0.95, Q3: 1.04 CV: 5.70%
Cuyoaco andesite unit	1.46/**1.47** (47) ± 0.26 Q1: 1.24, Q3: 1.73 CV: 17.90%	1.67/**1.63** (38) ± 0.21 Q1: 1.52, Q3: 1.75 CV: 12.64%	0.84/**0.86** (48) ± 0.10 Q1: 0.78, Q3: 0.92 CV: 11.95%	1.38/**1.38** (38) ± 0.18 Q1: 1.26, Q3: 1.48 CV: 12.98%
Basement				
Limestone Cretaceous	2.74/**2.73** (327) ± 0.55 Q1: 2.44, Q3: 2.93 CV: 20.11%	3.03/**2.93** (272) ± 0.58 Q1: 2.64, Q3: 3.34 CV: 19.23%	1.45/**1.35** (324) ± 0.46 Q1: 1.21, Q3: 1.54 CV: 31.57%	1.72/**1.56** (264) ± 0.59 Q1: 1.32, Q3: 1.93 CV: 34.52%
Chert nodules	3.26/**2.90** (16) ± 1.04 Q1: 2.67, Q3: 4.27 CV: 31.81%	4.11/**3.27** (17) ± 1.57 Q1: 2.91, Q3: 5.73 CV: 38.19%	1.54/**1.23** (17) ± 0.52 Q1:1.13, Q3: 2.13 CV: 33.75%	1.91/**1.80** (17) ± 0.83 Q1: 1.21, Q3: 2.32 CV: 43.68%
Shales Cretaceous	2.18/**2.12** (7) ± 0.30 Q1: 1.92, Q3: 2.27 CV: 13.60%	2.29/**2.13** (7) ± 0.39 Q1: 2.09, Q3: 2.26 CV: 17.25%	1.80/**1.80** (6) ± 0.09 Q1: 1.73, Q3: 1.87 CV: 4.75%	1.64/**1.65** (6) ± 0.06 Q1: 1.60, Q3: 1.69 CV: 3.52%
Limestone Jurassic	2.66/**2.68** (38) ± 0.23 Q1: 2.48, Q3: 2.84 CV: 8.65%	2.76/**2.66** (36) ± 0.32 Q1: 2.49, Q3: 3.08 CV: 11.76%	1.60/**1.50** (36) ± 0.34 Q1: 1.28, Q3: 1.95 CV: 21.41%	1.95/**1.69** (30) ± 0.75 Q1: 1.44, Q3: 2.50 CV: 38.66%
Sandstone Jurassic	1.38/**1.38** (6) ± 0.16 Q1: 1.28, Q3: 1.53 CV: 11.29%	2.28/**2.29** (6) ± 0.12 Q1: 2.20, Q3: 2.39 CV: 5.21%	0.88/**0.88** (6) ± 0.05 Q1: 0.84, Q3: 0.92 CV: 5.36%	1.89/**1.77** (6) ± 0.41 Q1: 1.61, Q3: 2.17 CV: 21.58%
Basaltic–andesitic dykes	1.71/**1.70** (22) ± 0.32 Q1: 1.47, Q3: 1.99 CV: 18.90%	1.86/**1.65** (26) ± 0.57 Q1: 1.53, Q3: 1.99 CV: 30.51%	0.88/**0.89** (20) ± 0.11 Q1: 0.79, Q3: 0.97 CV: 12.57%	1.12/**0.91** (24) ± 0.39 Q1: 0.83, Q3: 1.48 CV: 34.78%
Marble	3.10/**3.22** (65) ± 0.60 Q1: 2.51, Q3: 3.64 CV: 19.29%	3.52/**3.42** (65) ± 0.77 Q1: 2.78, Q3: 4.45 CV: 21.85%	1.52/**1.37** (62) ± 0.60 Q1: 1.15, Q3: 1.64 CV: 39.66%	3.01/**2.75** (61) ± 1.39 Q1: 1.85, Q3: 3.99 CV: 46.19%
Quartz veins	5.25/**5.21** (20) ± 0.61 Q1: 4.77, Q3: 5.80 CV: 11.65%	5.85/**5.78** (20) ± 0.79 Q1: 5.20, Q3: 6.49 CV: 13.44%	4.30/**3.92** (19) ± 1.08 Q1: 3.41, Q3: 5.36 CV: 25.19%	3.95/**3.50** (20) ± 1.31 Q1: 2.92, Q3: 5.18 CV: 33.16%
Skarn	3.23/**3.42** (127) ± 0.77 Q1: 2.62, Q3: 3.82 CV: 23.71%	3.44/**3.48** (126) ± 0.93 Q1: 2.87, Q3: 4.11 CV: 26.91%	1.81/**1.55** (123) ± 0.63 Q1: 1.32, Q3: 2.27 CV: 34.17%	2.25/**2.27** (117) ± 0.78 Q1: 1.63, Q3: 2.69 CV: 34.58%
Granitoids total	2.00/**1.97** (121) ± 0.50 Q1: 1.68, Q3: 2.28 CV: 25.19%	2.35/**2.24** (102) ± 0.59 Q1: 1.95, Q3: 2.57 CV: 25.31%	1.09/**1.08** (120) ± 0.26 Q1: 0.95, Q3: 1.18 CV: 23.91%	1.61/**1.40** (102) ± 0.79 Q1: 1.08, Q3: 1.73 CV: 49.28%
Granitoids (weak–moderate alteration)	2.13/**2.06** (81) ± 0.39 Q1: 1.84, Q3: 2.28 CV: 18.43%	2.31/**2.27** (68) ± 0.41 Q1: 2.06, Q3: 2.41 CV: 17.93%	1.14/**1.11** (77) ± 0.21 Q1: 1.03, Q3: 1.20 CV: 30.15%	1.69/**1.54** (62) ± 0.68 Q1: 1.30, Q3: 1.81 CV: 40.15%
Granitoids (strong alteration)	1.90/**1.64** (30) ± 0.62 Q1: 1.43, Q3: 2.50 CV: 32.71%	2.58/**2.73** (26) ± 0.92 Q1: 1.78, Q3: 3.28 CV: 35.60%	1.07/**1.00** (33) ± 0.32 Q1: 0.91, Q3: 1.18 CV: 30.15%	1.65/**1.26** (30) ± 1.03 Q1: 1.08, Q3: 1.52 CV: 62.35%

Arithmetic mean values in normal font, the numbers in bold represent the median, ± = standard deviation, () = number of analyzed plugs, Q1: 25% quartile, Q3: 75% quartile, λ = thermal conductivity, α = thermal diffusivity, dry or sat = analyzed under dry or saturated conditions

Table 5 Compressional and shear wave velocities of the LHVC

Unit	V_P dry [m s^{-1}]	V_P sat [m s^{-1}]	V_S dry [m s^{-1}]	V_S sat [m s^{-1}]
Post-caldera group				
Pyroclastics, undifferentiated	1615/**1605** (4) ± 85 Q1: 1539, Q3: 1701 CV: 5.25%	2637/**2633** (4) ± 145 Q1: 2506, Q3: 2771	946/**925** (4) ± 66 Q1: 897, Q3: 1016	1040/**1036** (4) ± 125 Q1: 926, Q3: 1158
Basalts	3770/**3674** (38) ± 689 Q1: 3177, Q3: 4325 CV: 18.29%	5521/**5573** (36) ± 866 Q1: 5046, Q3: 6009 CV: 15.69%	2216/**2183** (36) ± 385 Q1: 1919, Q3: 2541 CV: 17.36%	3362/**3276** (34) ± 554 Q1: 2924, Q3: 3890 CV: 16.47%
Ash fall deposits	1938/**1886** (4) ± 240 Q1: 1740, Q3: 2190	2222/**2219** (4) ± 273 Q1: 1962, Q3: 2485	1286/**1312** (4) ± 170 Q1: 1115, Q3: 1432	1402/**1348** (4) ± 235 Q1: 1218, Q3: 1639
Caldera group				
Zaragoza ignimbrite	2311/**2356** (34) ± 306 Q1: 2108, Q3: 2485 CV: 13.26%	3119/**3002** (31) ± 642 Q1: 2708, Q3: 3271 CV: 20.58%	1414/**1433** (32) ± 153 Q1: 1289, Q3: 1478 CV: 10.85%	1881/**1777** (29) ± 390 Q1: 1642, Q3: 1964 CV: 20.75%
Xáltipan ignimbrite total	1945/**1756** (117) ± 613 Q1: 1432, Q3: 2391 CV: 31.51%	2461/**2295** (81) ± 742 Q1: 2055, Q3: 2726 CV: 30.14%	1194/**1075** (114) ± 379 Q1: 886, Q3: 1472 CV: 31.75%	1458/**1378** (78) ± 416 Q1: 1215, Q3: 1686 CV: 28.52%
Xáltipan ig. (unaltered)	1773/**1628** (92) ± 525 Q1: 1382, Q3: 2134 CV: 29.60%	2371/**2256** (68) ± 616 Q1: 2071, Q3: 2685 CV: 25.98%	1088/**985** (89) ± 334 Q1: 850, Q3: 1343 CV: 30.64%	1479/**1380** (71) ± 425 Q1: 1239, Q3: 1710 CV: 28.72%
Xáltipan ig. (pumice)	2437/**2466** (18) ± 482 Q1: 2012, Q3: 2934 CV: 19.76%	2080/**2047** (7) ± 372 Q1: 1742, Q3: 2517 CV: 17.86%	1490/**1523** (18) ± 283 Q1: 1245, Q3: 1735 CV: 18.96%	1247/**1210** (7) ± 239 Q1: 982, Q3: 1468 CV: 19,16%
Xáltipan ig. (altered, welded)	2945/**3004** (7) ± 286 Q1: 2883, Q3: 3214 CV: 9.72%	3936/**3959** (6) ± 794 Q1: 3325, Q3: 4697 CV: 20.16%	1766/**1784** (7) ± 191 Q1: 1720, Q3: 1887 CV: 10.82%	2332/**2343** (6) ± 438 Q1: 1919, Q3: 2796 CV: 18.79%
Pre-caldera group				
Cinder cones total	3260/**3649** (15) ± 1089 Q1: 1673, Q3: 3979 CV: 33.40%	4195/**4351** (13) ± 1057 Q1: 4045, Q3: 4996 CV: 25.18%	1946/**2261** (15) ± 616 Q1: 1094, Q3: 2361 CV: 31.65%	2664/**2792** (13) ± 666 Q1: 2478, Q3: 3189 CV: 24.99%
Scoria	3880/**3880** (11) ± 270 Q1: 3640, Q3: 4090 CV: 6.95%	4584/**4444** (11) ± 510 Q1: 4068, Q3: 5198 CV: 11.12%	2297/**2289** (11) ± 151 Q1: 2126, Q3: 2445 CV: 6.58%	2907/**2852** (11) ± 330 Q1: 2590, Q3: 3202 CV: 11.35%
Fallout deposits	1556/**1532** (4) ± 88 Q1: 1487, Q3: 1648 CV: 5.66%	2058 (2)	984/**975** (4) ± 96 Q1: 897, Q3: 1079	1326 (2)
Teziutlán andesite unit total	3787/**3879** (138) ± 1204 Q1: 2828, Q3: 4706 CV: 31.80%	5341/**5425** (117) ± 1022 Q1: 4708, Q3: 6219 CV: 19.13%	2200/**2286** (132) ± 683 Q1: 1666, Q3: 2738 CV: 31.04%	3168/**3213** (114) ± 619 Q1: 2758, Q3: 3730 CV: 19.53%
Teziutlán and. (nonporous)	4125/**4384** (101) ± 1145 Q1: 3417, Q3: 4981 CV: 27.75%	5476/**5556** (89) ± 1050 Q1: 4729, Q3: 6404 CV: 19.17%	2407/**2561** (95) ± 639 Q1: 1969, Q3: 2850 CV: 26.55%	3259/**3285** (86) ± 622 Q1: 2842, Q3: 3764 CV: 19.08%
Teziutlán and. (porous)	2863/**2972** (37) ± 826 Q1: 2056, Q3: 3667 CV: 28.86%	4908/**5196** (28) ± 799 Q1: 4362, Q3: 5545 CV: 16.28%	1667/**1762** (37) ± 474 Q1: 1211, Q3: 2106 CV: 28.44%	2889/**3009** (28) ± 523 Q1: 2513, Q3: 3394 CV: 18.23%
Cuyoaco andesite unit	4142/**4029** (48) ± 1039 Q1: 3253, Q3: 5027 CV: 25.08%	5280/**4893** (37) ± 1314 Q1: 4114, Q3: 6559 CV: 24.89%	2457/**2377** (48) ± 602 Q1: 1984, Q3: 2906 CV: 24.48%	3083/**2972** (37) ± 775 Q1: 2413, Q3: 3806 CV: 25.13%
Basement				
Limestone Cretaceous	5310/**5298** (380) ± 1223 Q1: 4459, Q3: 6118 CV: 23.03%	7175/**7171** (275) ± 1446 Q1: 6311, Q3: 8230 CV: 20.16%	3118/**3058** (368) ± 731 Q1: 2615, Q3: 3535 CV: 23.44%	4271/**4317** (272) ± 835 Q1: 3824, Q3: 4856 CV: 19.54%
Chert nodules	5806/**5813** (18) ± 828 Q1: 5348, Q3: 6339 CV: 14.25%	8142/**8251** (15) ± 1148 Q1: 7248, Q3: 9172 CV: 14.10%	3532/**3588** (18) ± 639 Q1: 3048, Q3: 3889 CV: 18.10%	4763/**4849** (15) ± 718 Q1: 4092, Q3: 5361 CV: 15.07%
Shales Cretaceous	2826/**2469** (7) ± 1015 Q1: 2104, Q3: 3551 CV: 35.92%	3573/**3210** (7) ± 1190 Q1: 2534, Q3: 4162 CV: 33.31%	1467/**1365** (6) ± 322 Q1: 1258, Q3: 1624 CV: 21.97%	1973/**2058** (6) ± 404 Q1: 1529, Q3: 2322 CV: 20.45%
Limestone Jurassic	5057/**4834** (38) ± 872 Q1: 4384, Q3: 5800 CV: 17.23%	6358/**6360** (34) ± 1156 Q1: 5734, Q3: 7308 CV: 18.19%	3057/**2953** (36) ± 638 Q1: 2583, Q3: 3329 CV: 20.88%	3779/**3760** (32) ± 742 Q1: 3218, Q3: 4490 CV: 19.64%

Table 5 (continued)

Unit	V_P dry [m s^{-1}]	V_P sat [m s^{-1}]	V_S dry [m s^{-1}]	V_S sat [m s^{-1}]
Sandstone Jurassic	2300/**1959** (7) ± 1048 Q1: 1758, Q3: 2084 CV: 45.56%	3119/**3150** (6) ± 401 Q1: 2778, Q3: 3472 CV: 12.85%	1380/**1200** (7) ± 417 Q1: 1178, Q3: 1366 CV: 30.20%	1828/**1850** (6) ± 245 Q1: 1648, Q3: 2044 CV: 13.37%
Basaltic–andesitic dykes	4538/**4461** (24) ± 999 Q1: 3975, Q3: 5150 CV: 22.02%	5842/**5938** (20) ± 833 Q1: 5559, Q3: 6031 CV: 14.25%	2692/**2702** (24) ± 542 Q1: 2493, Q3: 3004 CV: 20.13%	3557/**3553** (20) ± 508 Q1: 3363, Q3: 3668 CV: 14.28%
Marble	4028/**3697** (85) ± 1268 Q1: 3031, Q3: 5078 CV: 31.48%	6698/**6581** (67) ± 1690 Q1: 5304, Q3: 7964 CV: 25.22%	2262/**2141** (84) ± 628 Q1: 1749, Q3: 2760 CV: 27.74%	3864/**3826** (66) ± 1069 Q1: 2971, Q3: 4761 CV: 27.66%
Quartz veins	3588/**3683** (20) ± 752 Q1: 3143, Q3: 4222 CV: 20.96%	5481/**5598** (20) ± 1658 Q1: 4186, Q3: 6377 CV: 30.26%	2120/**2081** (20) ± 418 Q1: 1864, Q3: 2522 CV: 19.74%	3181/**3378** (20) ± 857 Q1: 2477, Q3: 371 CV: 26.94%
Skarn	4627/**4570** (146) ± 1123 Q1: 3779, Q3: 5319 CV: 24.28%	6326/**6297** (133) ± 1372 Q1: 5661, Q3: 7130 CV: 21.69%	2704/**2639** (141) ± 656 Q1: 2189, Q3: 3208 CV: 24.27%	3742/**3752** (130) ± 815 Q1: 3328, Q3: 4261 CV: 21.78%
Granitoids total	3920/**3815** (124) ± 1172 Q1: 2986, Q3: 4719 CV: 29.91%	5122/**5176** (107) ± 1482 Q1: 3918, Q3: 6034 CV: 28.93%	2382/**2303** (122) ± 732 Q1: 1806, Q3: 2765 CV: 30.74%	3052/**3094** (105) ± 939 Q1: 2375, Q3: 3593 CV: 30.78%
Granitoids (weak–moderate alteration)	4352/**4302** (80) ± 1115 Q1: 3495, Q3: 5158 CV: 25.61%	5714/**5653** (66) ± 1407 Q1: 4860, Q3: 6424 CV: 24.63%	2659/**2556** (79) ± 700 Q1: 2195, Q3: 3173 CV: 26.32%	3420/**3415** (64) ± 882 Q1: 2905, Q3: 3908 CV: 25.80%
Granitoids (strong alteration)	3360/**3279** (31) ± 684 Q1: 2954, Q3: 3728 CV: 20.36%	4514/**4723** (31) ± 970 Q1: 3771, Q3: 5284 CV: 21.49%	2025/**1957** (31) ± 414 Q1: 1771, Q3: 2300 CV: 20.46%	2737/**2806** (31) ± 608 Q1: 2305, Q3: 3192 CV: 22.20%

Arithmetic mean values in normal font, the numbers in bold represent the median, ± = standard deviation, () = number of analyzed plugs, Q1: 25% quartile, Q3: 75% quartile, V_P = p-wave velocity, V_S = s-wave velocity, dry or sat = analyzed under dry or saturated conditions

Table 6 Rock compressibility, magnetic susceptibility, specific and volumetric heat capacity of the LHVC

Unit	ß [PSI]	χ [10^{-3} SI]	cp [J kg^{-1} K^{-1}]	VHC [J m^3 K^{-1}]
Post-caldera group				
Pyroclastics, undifferentiated	3.3E-04	3.977/**3.758** (3) ± 0.448	883 (1)	1306 (1)
Basalts	1.3E-05	1.356/**1.357** (18) ± 0.534 Q1: 0.997, Q3: 1.586 CV: 39.39%	753/**758** (5) ± 51 Q1: 701, Q3: 801 CV: 6.74%	1698/**1663** (5) ± 98 Q1: 1612, Q3: 1802 CV: 5.77%
Ash fall deposits	4.2E-04	− 0.004/− **0.009** (4) ± 0.016 Q1: -0.014, Q3: 0.013	862 (1)	1034 (1)
Caldera group				
Zaragoza ignimbrite	1.4E-04	1.098/**0.842** (15) ± 0.586 Q1: 0.630, Q3: 1.555 CV: 53.34%	766/**776** (3) ± 21	1248/**1164** (3) ± 176
Xáltipan ignimbrite total	2.6E-04	0.441/**0.310** (50) ± 0.431 Q1: 0.095, Q3: 0.778 CV: 97.72%	762/**750** (7) ± 38 Q1: 740, Q3: 803 CV: 4.95%	992/**931** (9) ± 348 Q1: 842, Q3: 1151 CV: 35.07%
Xáltipan ig. (unaltered)	2.9E-04	0.495/**0.325** (41) ± 0.446 Q1: 0.089, Q3: 0.963 CV: 90.14%	767/**763** (4) ± 28 Q1: 742, Q3: 796	975/**931** (7) ± 147 Q1: 842, Q3: 1044 CV: 15.03%
Xáltipan ig. (pumice)	6.3E-04	0.115/**0.117** (8) ± 0.032 Q1: 0.086, Q3: 0.131 CV: 27,91%	778 (2) ± 50	408 (1)
Xáltipan ig. (altered, welded)	6.2E-06	0.874 (1)	707 (1)	1697 (1)
Pre-caldera group				
Cinder cones total	5.8E-05	0.773/**0.644** (7) ± 0.330 Q1: 0.618, Q3: 1.008 CV: 42.61%	747/**761** (3) ± 32	1349/**1520** (3) ± 312

Table 6 (continued)

Unit	ß [PSI]	χ [10^{-3} SI]	cp [J kg^{-1} K^{-1}]	VHC [J m^3 K^{-1}]
Scoria	3.1E-05	0.598/**0.639** (5) ± 0.090 Q1: 0.528, Q3: 0.647 CV: 15.02%	765 (2) ± 6	1530 (2) ± 14
Fallout deposits	5.3E-04	1.211 (2) ± 0.287	710 (1)	989 (1)
Teziutlán andesite unit total	5.7E-06	6.092/**5.697** (80) ± 2.852 Q1: 4.081, Q3: 7.822 CV: 46.82%	765/**766** (15) ± 40 Q1: 751, Q3: 784 CV: 5.25%	1963/**2044** (15) ± 148 Q1: 1844, Q3: 2058 CV: 7.52%
Teziutlán and. (nonporous)	1.8E-06	6.995/**6.524** (55) ± 2.859 Q1: 5.322, Q3: 8.223 CV: 40.88%	762/**765** (10) ± 46 Q1: 744, Q3: 786 CV: 6.09%	2035/**2044** (11) ± 92 Q1: 1991, Q3: 2078 CV: 4.52%
Teziutlán and. (porous)	2.7E-05	4.105/**4.111** (25) ± 1.551 Q1: 2.767, Q3: 5.243 CV: 37.78%	772/**774** (5) ± 27 Q1: 749, Q3: 794 CV: 3.34%	1767/**1761** (4) ± 59 Q1: 1714, Q3: 1826
Cuyoaco andesite unit	2.9E-06	2.367/**2.471** (23) ± 1.269 Q1: 0.956, Q3: 2.961 CV: 53.63%	752/**744** (7) ± 26 Q1: 728, Q3: 766 CV: 3.51%	1941/**1924** (7) ± 127 Q1: 1817, Q3: 2002 CV: 6.53%
Basement				
Limestone Cretaceous	8.6E-07	0.162/− **0.004** (193) ± 0.634 Q1: − 0.026, Q3: 0.021 CV: 391.76%	807/**814** (32) ± 31 Q1: 785, Q3: 825 CV: 3.79%	2159/**2162** (32) ± 127 Q1: 2095, Q3: 2246 CV: 5.87%
Chert nodules	3.0E-07	− 0.029/− **0.032** (15) ± 0.012 Q1: − 0.033, Q3: -0.0267 CV: 40.95%	814 (2) ± 30	2157 (2) ± 138
Shales Cretaceous	1.6E-06	0.056/**0.051** (7) ± 0.010 Q1: 0.049, Q3: 0.058 CV: 17.59%	780 (1)	2068 (1)
Limestone Jurassic	8.7E-07	0.038/**0.001** (25) ± 0.115 Q1: − 0.003, Q3: 0.019 CV: 306.01%	829/**823** (6) ± 40 Q1: 809, Q3: 847 CV: 4.77%	2171/**2155** (5) ± 108 Q1: 2080, Q3: 2271 CV: 4.98%
Sandstone Jurassic	6.0E-05	0.067/**0.006** (6) ± 0.157 Q1: − 0.014, Q3: 0.125 CV: 232.56%	739 (1)	1524 (1)
Basaltic–andesitic dykes	9.1E-07	11.270/**4.199** (14) ± 12.410 Q1: 2.909, Q3: 26.52 CV: 110.05%	757 (2) ± 55	2088 (2) ± 312
Marble	9.8E-07	0.124/− **0.027** (41) ± 0.498 Q1: − 0.034, Q3: 0.008 CV: 402.46%	853/**836** (9) ± 45 Q1: 825, Q3: 859 CV: 5.25%	2318/**2269** (9) ± 123 Q1: 2208, Q3: 2435 CV: 5.32%
Quartz veins	3.3E-06	0.349/**0.136** (19) ± 0.713 Q1: 0.052, Q3: 0.350 CV: 204.11%	760/**763** (4) ± 13 Q1: 746, Q3: 771 V: 1.75%	1941/**1937** (4) ± 51 Q1: 1895, Q3: 1991
Skarn	1.6E-06	94.120/**3.920** (62) ± 190.800 Q1: 1.756, Q3: 102.800 CV: 202.72%	742/**740** (11) ± 26 Q1: 746, Q3: 763 CV: 3.51%	2399/**2477** (12) ± 333 Q1: 2028, Q3: 2629 CV: 13.89%
Granitoids total	5.1E-06	4.363/**3.331** (60) ± 4.457 Q1: 0.301, Q3: 6.402 CV: 102.15%	775/**787** (15) ± 54 Q1: 749, Q3: 809 CV: 6.91%	1901/**1920** (26) ± 123 Q1: 1798, Q3: 1979 CV: 6.48%
Granitoids (weak–moderate alteration)	1.2E-06	5.206/**3.573** (38) ± 4.878 Q1: 1.738, Q3: 6.795 V: 93.70%	769/**779** (12) ± 57 Q1: 733, Q3: 793 CV: 7.39%	1956/**1972** (9) ± 174 Q1: 1811, Q3: 2065 CV: 8.90%
Granitoids (strong alteration)	1.2E-05	0.036/**0.026** (12) ± 0.048 Q1: − 0.0068, Q3: 0.085 CV: 135.70%	795/809 (3) ± 38	1931/**1948** (4) ± 100 Q1: 1828, Q3: 2016

Arithmetic mean values in normal font, the numbers in bold represent the median, ± = standard deviation, () = number of analyzed plugs, Q1: 25% quartile, Q3: 75% quartile, ß = compressibility, cp = specific heat capacity, VHC = volumetric heat capacity, X = magnetic susceptibility

Appendix B Additional information on data processing

Table 7 provides an overview of the empirical relationships that were applied for the temperature and pressure correction of thermal conductivity, thermal diffusivity, specific

heat capacity and sonic wave velocities. These relationships are based on laboratory experiments of the respective parameter at elevated temperature and/or pressure conditions. Here we present the correction function for thermal conductivity of sedimentary rocks as an example to explain the procedure. The effect of temperature on thermal conductivity was calculated using the following equations:

$$\lambda(0) = 0.54 \cdot \lambda(25) + \frac{1}{2}\sqrt{1.16 \cdot (\lambda(25))^2 - 0.39 \cdot \lambda(25)}, \tag{4}$$

$$\lambda(T) = \frac{\lambda(0)}{0.99 + T \cdot (0.0034 - 0.0039/\lambda(0))}, \tag{5}$$

where λ (0) is the normalized thermal conductivity at 0 °C, λ (25) is the measured thermal conductivity at 25 °C, and λ (T) is the thermal conductivity at temperature T in °C. Abdulagatova et al. (2009) fitted their experimental data to the following empirical equations:

$$\lambda(T,P) = \lambda_\infty \exp\left(-\frac{P_0}{P}\right) + \lambda_0(P = 0.1, T), \tag{6}$$

$$\lambda_\infty(T) = a_0 + a_1 T + a_2 T^2, \tag{7}$$

$$\lambda_0(P = 0.1,\ T) = (C + \mathrm{DT})^{-1}, \tag{8}$$

where the values of parameters $a_0 = 1.7358 \times 10^{-2}$, $a_1 = 1.0272 \times 10^{-3}$, $a_2 = -\ 8.1 \times 10^{-7}$, $C = 0.30532$, $D = 0.2302 \times 10^{-3}$, P_0 = atmospheric pressure and P = pressure at reservoir depth. Based on the results presented in Abdulagatova et al. (2009), the following equation was derived to calculate the effect of pressure on thermal conductivity:

$$\lambda(P) = (-1E - 10) \cdot P^4 + (1E - 07) \cdot P^3 - (4E - 05) \cdot P^2 + 0.0074 \cdot P + \lambda \tag{9}$$

Table 7 Empirical relationships used for temperature and pressure correction of thermal properties and sonic wave velocities

Parameter	Type of correction	References	Rock type
Thermal conductivity	Temperature	Vosteen and Schellschmidt (2003)	Sedimentary, magmatic and metamorphic rocks
		Chen et al. (2021)	Volcanic rocks
	Pressure	Abdulagatov et al. (2006), Abdulagatova et al. (2009)	Sandstone, limestone, intrusive rocks
Thermal diffusivity	Temperature	Vosteen and Schellschmidt (2003)	Sedimentary, magmatic and metamorphic rocks
		Durham et al. (1987)	Volcanic rocks
Specific heat capacity	Temperature	Vosteen and Schellschmidt (2003)	Sedimentary, magmatic and metamorphic rocks
Sonic wave velocities	Temperature and pressure	Qi et al. (2020)	Carbonates
		Hughes and Maurette (1957) and Birch (1961)	Magmatic and intrusive rocks
		Vinciguerra et al. (2005)	Tuff

where $\lambda(P)$ is the thermal conductivity at reservoir pressure, λ = thermal conductivity at laboratory conditions and P is the respective pressure at reservoir depth.

Acknowledgements
We thank Ing. Miguel Angel Ramírez Montes Subgerencia de Estudios Gerencia de Proyectos Geotermoeléctricos and the Comisión Federal de Electricidad (CFE) team for their help during our sampling campaign. We also acknowledge our Mexican and European colleagues for their help and collaboration during our field work in Mexico. Special thanks to Antonio Pola from UNAM for providing the drilling device for our work at the CFE camp. Many thanks to Ruud Hendrikx, Baptiste Lepillier, Juliane Kummerow, Dirk Scheuvens and Gabriela Schubert for their support in the laboratories to perform chemical analyses. Furthermore, we thank Jana Perizonius, Thomas Kramer, Maximilian Bech and Roland Knauthe for their contribution to this project.

Authors' contributions
All authors contributed to this study and reviewed the manuscript. All authors read and approved the final manuscript.

Funding
Open Access funding enabled and organized by Projekt DEAL. This project has received funding from the European Union's Horizon 2020 research and innovation programme under Grant agreement No. 727550 (GEMex) and the Mexican Energy Sustainability Fund CONACYT-SENER, project 2015-04-68074.

Data availability
The results are included in the tables and figures presented in this study. Raw data can be accessed under https://doi.org/10.25534/tudatalib-201.10 (Weydt et al. 2021a).

Declarations

Competing interests
The authors declare that they have no conflict of interest.

Author details
[1]Department of Geothermal Science and Technology, Technische Universität Darmstadt, Schnittspahnstraße 9, 64287 Darmstadt, Germany. [2]Helmholtz Centre Potsdam, GFZ German Research Centre for Geosciences, Section 4.8, Geoenergy, Telegrafenberg, 14473 Potsdam, Germany.

Received: 30 September 2021 Accepted: 16 January 2022
Published online: 21 March 2022

References

Abdulagatov IM, Emirov SN, Abdulagatova ZZ, Askerov SY. Effect of Pressure and Temperature on the Thermal Conductivity of Rocks. J Chem Eng Data. 2006;51(1):22–33. https://doi.org/10.1021/je050016a.
Abdulagatova Z, Abdulagatov IM, Emirov VN. Effect of temperature and pressure on the thermal conductivity of sandstone. Int J Rock Mech Min Sci. 2009;46(6):1055–71. https://doi.org/10.1016/j.ijrmms.2009.04.011.
Adams SJ. Quantifying Petrophysical Uncertainties. IN: SPE 93125, SPE International conference proceeding, the 2005 Asia Pacific Oil and Gas Conference and Exhibition, 5–7 April, Jarkarta, Indonesia 2005; 2005. p. 6.
Arellano VM, Garcia A, Barragán RM, Izquierdo G, Aragón A, Nieva D. An updated conceptual model of the Los Humeros geothermal reservoir (Mexico). J Volcanol Geotherm Res. 2003;124(1–2):67–88. https://doi.org/10.1016/S0377-0273(03)00045-3.
Aretz A, Bär K, Götz AE, Sass I. Outcrop analogue study of Permocarboniferous geothermal sandstone reservoir formations (northern Upper Rhine Graben, Germany): impact of mineral content, depositional environment and diagenesis on petrophysical properties. Int J Earth Sci (geol Rundsch). 2016;2015(135):1431–52. https://doi.org/10.1007/s00531-015-1263-2.
Ashena R, Behrenbruch P, Ghalambor A. Log-based rock compressibility estimation for Asmari carbonate formation. J Petrol Explor Prod Technol. 2020;10:2771–83. https://doi.org/10.1007/s13202-020-00934-0.
ASTM D4525-13e2. Standard Test Method for Permeability of Rocks by Flowing Air. ASTM International, West Con-shohocken; 2013. p. 5. https://doi.org/10.1520/D4525-13E02.
ASTM D4543-19. Standard Practices for Preparing Rock Core Specimens and Determining Dimensional and Shape Tolerances. ASTM International, West Conshohocken; 2019. p. 13. https://doi.org/10.1520/D4543-19.
Athy LF. Density, porosity and compaction of sedimentary rocks. AAPG Bull. 1930;14(1):1–24. https://doi.org/10.1306/3D93289E-16B1-11D7-8645000102C1865D.
Bär K. Untersuchung der tiefengeothermischen Potenziale von Hessen. PhD thesis, 111 Fig., 28 Tab., 6 App., XXVI and p. 265. Germany: Technische Universität Darmstadt; 2012.
Bär K, Reinsch T, Bott J. The PetroPhysical Property Database (P^3)—a global compilation of lab-measured rock properties. Earth Syst Sci Data. 2020;12:2485–515. https://doi.org/10.5194/essd-12-2485-2020.
Baroomand M, Safari A, Bahroudi A. Magnetic susceptibility as a tool for mineral exploration (Case study: Southern of Zagros Mountains). Int J Min and Geo-Eng. 2015;49:57–66. https://doi.org/10.22059/IJMGE.2015.54364.
Benediktsdóttir Á, Arango-Galván C, Páll Hersir G, Held S, Romo-Jones JM, Luis-Salas J, Avil´s T, Ruiz-Aguilar D, Már Vilhjálmsson A. The Los Humeros superhot geothermal resource in Mexico: Results from an extensive resistivity

survey. GEMex Final Conference, 18–19 February 2020, Potsdam, Germany; 2020. http://www.gemex-h2020.eu. Accessed 28 Sep 2021.
Bernard R, Taran Y, Pennisi M, Tello E, Ramirez A. Chloride and Boron behavior in fluids of Los Humeros geothermal field (Mexico): a model based on the existence of deep acid brine. Appl Geochem. 2011;26:2064–73. https://doi.org/10.1016/j.apgeochem.2011.07.004.
Birch F. The velocity of compressional waves in rocks to 10 kilobars, part 2. J Geophys Res. 1961;66(7):2199–224. https://doi.org/10.1029/JZ066i007p02199.
Bourbiaux B, Basquet R, Daniel JM, Hu LY, Jenni S, Lange G, Rasolofosaon P. Fractured reservoirs modelling a review of the challenges and some recent solutions. First Break. 2005;23:33–40. https://doi.org/10.3997/1365-2397.2005018.
Calcagno P, Trumpy E, Gutiérrez-Negrín LC, Liotta D, Carrasco-Núñez G, Norini G, Brogi A, Garduño-Monroy VH, Benediktsdóttir A, Gaucher E, Toldeo T, Páll Hersir G, Manzella A, Santilano A, Gola G, Macías J L, Vaessen L, Evanno G, Arango-Galván C. 3D Geomodels of Los Humeros and Acoculco geothermal systems (Mexico)—H2020 GEMex Project: Methodology, products and feedback. GEMex Final Conference, 18–19 February, 2020, Potsdam, Germany; 2020. http://www.gemex-h2020.eu. Accessed 28 Sep 2021.
Carrasco-Núñez G, Gómez-Tuena A, Lozano VL. Geologic map of Cerro Grande volcano and surrounding area, Central Mexico. Geol. Soc. Am. Map Chart Ser. MCH 081; 1997. https://www.worldcat.org/title/geologic-map-of-cerro-grande-volcano-and-surrounding-area-central-mexico/oclc/37949323&referer=brief_results, Accessed 28 Sep 2021.
Carrasco-Núñez G, McCurry M, Branney MJ, Norry M, Willcox C. Complex magma mixing, mingling, and withdrawal associated with an intraplinian ignimbrite eruption at a large silicic caldera volcano: Los Humeros of central Mexico. GSA Bull. 2012;124(11–12):1793–809. https://doi.org/10.1130/B30501.1.
Carrasco-Núñez G, Hernández J, De Léon L, Dávilla P, Norini G, Bernal JP, Jicha B, Navarro M, López-Quiroz P. Geologic Map of Los Humeros volcanic complex and geothermal field eastern Trans-Mexican Volcanic Belt. Terra Digitalis. 2017a;1(2):1–11. https://doi.org/10.22201/igg.terradigitalis.2017.2.24.78.
Carrasco-Núñez G, López-Martínez M, Hernández J, Vargas V. Subsurface stratigraphy and its correlation with the surficial geology at Los Humeros geothermal field, eastern Trans-Mexican Volcanic Belt. Geothermics. 2017b;67:1–17. https://doi.org/10.1016/j.geothermics.2017.01.001.
Carrasco-Núñez G, Bernal JP, Dávilla P, Jicha B, Giordano G, Hernández J. Reappraisal of Los Humeros Volcanic Complex by New U/Th Zircon and 40Ar/39Ar dating: implications for greater geothermal potential. Geochem Geophys Geosyst. 2018;19:132–49. https://doi.org/10.1002/2017GC007044.
Carrasco-Núñez G, Norini G, Giordano G, Lucci F, Hernández J, Cavazos J, Cid-Luna H, Dávila P, Peña D, Barrios S, Fernández F. Towards a Comprehensive Volcanologic, Magmatic and Structural Model for Superhot Geothermal Systems: Case Study of Los Humeros Caldera Complex, Mexico. In: Proceedings World Geothermal Congress 2020+1. Reykjavik, Iceland, 2021. p. 15.
Cavazos-Álvarez JA, Carrasco-Núñez G. Effective mapping of large ignimbrites by using a GIS-based methodology; case of the Xáltipan ignimbrite from Los Humeros Volcanic Complex. Terra Digitalis. 2019;3(2):78–97. https://doi.org/10.22201/igg.25940694.2019.2.65.142.
Cavazos-Álvarez JA, Carrasco-Núñez G, Dávila-Harris P, Peña D, Jáquez A, Artega D. Facies variations and permeability of ignimbrites in active geothermal systems; case study of the Xáltipan ignimbrite at Los Humeros Volcanic Complex. J S Am Earth Sci. 2020;104: 102810. https://doi.org/10.1016/j.jsames.2020.102810.
Cedillo F. Modelo hidrogeológico de los yacimientos geotérmicos de Los Humeros, Pue., Mexico. Geotermia Revista Mexicana De Geoenergía. 1999;15(3):159–70.
Cedillo F. Hydrogeologic model of the geothermal reservoirs from Los Humeros, Puebla, Mexico. In: Proceedings World Geothermal Congress 2000, Kyushu-Tohoku, Japan, May 28-June 10, 2000; 2000.
Chen T, Clauser C, Marquat G, Willbrand K, Hiller T. Upscaling permeability for three-dimensional fractured porous rocks with multiple boundary method. Hydrogeol J. 2018;26:1903–16. https://doi.org/10.1007/s10040-018-1744-z.
Chen C, Zhu C, Zhang B, Tang B, Li K, Li W, Fu X. Effect of temperature on the thermal conductivity of rocks and its implication for in situ correction. Geofluids. 2021. https://doi.org/10.1155/2021/6630236.
Cladouhos T, Petty S, Bonneville AH, Schultz A, Sorlie F. Super-Hot EGS and the Newberry Deep Drilling project. In: Proceedings 43nd Workshop on Geothermal Reservoir Engineering, Stanford University, Stanford, California, 2018; 2018. p. 13.
Clauser C, Huenges E. Thermal conductivity of rocks and minerals. Rock physics & phase relations. In: Ahrens TJ, editor. Rock physics and phase relations: a handbook of physical constants. Washington: American Geophysical Union; 1995. p. 105–26. https://doi.org/10.1029/rf003p0105.
Contreras LF, Brown ET, Ruest M. Bayesian data analysis to quantify the uncertainty of intact rock strength. J Rock Mech Geotech Eng. 2018;10:11–31. https://doi.org/10.1016/j.jrmge.2017.07.008.
Cornejo N. Towards visualization of the reservoir settings in the Los Humeros and Acoculco geothermal fields using gravity. GEMex Final Conference, Potsdam, Germany, 2020, S1.6. http://www.gemex-h2020.eu. Accessed 28 Sep 2021.
Dávila-Harris P, Carrasco-Núñez G. An unusual syn-eruptive bimodal eruption: the Holocene Cuicuiltic Member at Los Humeros caldera, Mexico. J Volcanol Geotherm Res. 2014;271:24–42. https://doi.org/10.1016/j.jvolgeores.2013.11.020.
Deb P, Knapp D, Marquart G, Clauser C. Report on the numerical reservoir model used for the simulation of the Los Humeros super-hot reservoir in Mexico. Deliverable 6.3. GEMex H2020 project, European Commission. 2019;6.3(1):1–50. http://www.gemex-h2020.eu. Accessed 28 Sep 2021.
Durán EL, Adam L, Wallis IC, Barnhoorn A. Mineral alteration and fracture influence on the elastic properties of volcaniclastic rocks. J Geophys Res: Solid Earth. 2019;124(5):4576–600. https://doi.org/10.1029/2018JB016617.
Durham WB, Mirkovich VV, Heard HC. Thermal diffusivity of igneous rocks at elevated pressure and temperature. J Geophys Res. 1987;92:11615–34.
Ebong ED, Akpan AE, Ekwok SE. Stochastic modelling of spatial variability of petrophysical properties in parts of the Niger Delta Basin, southern Nigeria. J Petrol Explor Prod Technol. 2019;10:569–85. https://doi.org/10.1007/s13202-019-00787-2.

Eshagi E, Smith S, Ayer J. Petrophysical characterisation (i.e. density and magnetic susceptibility) of major rock units within the Abitibi Greenstone Belt. Laurentian University Mineral Exploration Research Centre. 2019;MERC-ME-2019–144:88.
Farmer CL. Upscaling: a review. Int J Numer Meth Fl. 2002;40:63–78. https://doi.org/10.1002/fld.267.
Farquharson JI, Wadsworth FB. Upscaling permeability in anisotropic volcanic systems. J Volcanol Geotherm Res. 2018;364:35–47. https://doi.org/10.1016/j.jvolgeores.2018.09.002.
Farquharson JI, Heap MJ, Varley NR, Baud P, Reuschlé T. Permeability and porosity relationships of edifice-forming andesites: a combined field and laboratory study. J Volcanol Geotherm Res. 2015;297:52–68. https://doi.org/10.1016/j.jvolgeores.2015.03.016.
Ferrari L, Orozco-Esquivel T, Manea V, Manea M. The dynamic history of the Trans-Mexican Volcanic Belt and the Mexico subduction zone. Tectonophysics. 2012;522–523:122–49. https://doi.org/10.1016/j.tecto.2011.09.018.
Ferriz H, Mahood G. Eruptive rates and compositional trends at Los Humeros volcanic center, Puebla, Mexico. J Geophys Res. 1984;89:8511–24. https://doi.org/10.1029/JB089iB10p08511.
Filomena CM, Hornung J, Stollhofen H. Assessing accuracy of gas-driven permeability measurements: a comparative study of diverse Hassler-cell and probe permeameter devices. Solid Earth. 2014;5:1–11. https://doi.org/10.5194/se-5-1-2014.
Fitz-Díaz E, Lawton TF, Juárez-Arriaga E, Chávez-Cabello G. The Cretaceous-Paleogene Mexican orogen: structure, basin development, magmatism and tectonics. Earth-Sci Rev. 2017;183:56–84. https://doi.org/10.1016/j.earscirev.2017.03.002.
Friðleifsson GÓ, Armannsson H, Gudmundsson A, Arnason K, Mortensen AK, Palsson B, Einarsson GM. Site selection for the well IDDP-1 at Krafla. Geothermics. 2014a;49:9–15. https://doi.org/10.1016/j.geothermics.2013.06.001.
Friðleifsson GÓ, Elders WA, Albertsson A. The concept of the Iceland deep drilling project. Geothermics. 2014b;49:2–8. https://doi.org/10.1016/j.geothermics.2013.03.004.
Frolova J, Vladimir L, Sergey R, David Z. Effects of hydrothermal alterations on physical and mechanical properties of rocks in the Kuril-Kamchatka island arc. Eng Geol. 2014;183:80–95. https://doi.org/10.1016/j.enggeo.2014.10.011.
Fuentes-Guzmán E, González-Partida E, Camprubí A, Hernández-Avilés G, Gabites J, Ruggieri G, Iriondo A, López-Martínez M. The Miocene Tatatila–Las Minas IOCG skarn deposits (Veracruz) as a result of adakitic magmatism in the Trans-Mexican Volcanic Belt Short running title: Miocene IOCG deposits and adakitic magmas in the Trans-Mexican Volcanic Belt. Boletín de la Sociedad Geológica Mexicana. 2020;73(3):A1105020. https://doi.org/10.18268/BSGM2020v72n3a110520.
Geotron-Elektronik. LightHouse UMPC V1.02 Installations- und Bedienungshandbuch. Pirna: Geotron-Elektronik. 2011;1.6, pp. 47.
Gómez-Tuena A, Carrasco-Núñez G. Cerro Grande volcano: the evolution of a Miocene stratocone in the early Trans-Mexican Volcanic Belt. Tectonophysics. 2000;318:249–80. https://doi.org/10.1016/S0040-1951(99)00314-5.
Gonzalez-Garcia H, Francke H, Huenges E. Estimation of depression cones of Los Humeros. GEMex Final Conference, Potsdam, Germany, 2020; 2020. http://www.gemex-h2020.eu. Accessed 28 Sep 2021.
Hartmann A, Peching R, Clauser C. Petrophysical analysis of regional-scale thermal properties for improved simulations of geothermal installations and basin-scale heat and fluid flow. Int J Earth Sci. 2008;97:421–33. https://doi.org/10.1007/s00531-007-0283-y.
Heap MJ, Kennedy BM. Exploring the scale-dependent permeability of fractured andesite. Earth Planet Sci Lett. 2016;447:139–50. https://doi.org/10.1016/j.epsl.2016.05.004.
Heap MJ, Violay ME. The mechanical behaviour and failure modes of volcanic rocks: a review. Bull Volcanol. 2021;83(5):1–47. https://doi.org/10.1007/s00445-021-01447-2.
Heap MJ, Lavallée Y, Petrakova L, Baud P, Reuschlé T, Varley NR, Dingwell DB. Microstructural controls on the physical and mechanical properties of edifice-forming andesites at Volcán de Colima, Mexico. J Geophys Res Solid Earth. 2014a;119(4):2925–63. https://doi.org/10.1002/2013JB010521.
Heap MJ, Baud P, Meredith PG, Vinciguerra S, Reuschlé T. The permeability and elastic moduli of tuff from Campi Flegrei, Italy: implications for ground deformation modelling. Solid Earth. 2014b;5(1):25–44. https://doi.org/10.5194/se-5-25-2014.
Heap MJ, Gravley DM, Kennedy BM, Gilg HA, Bertolett E, Barker SL. Quantifying the role of hydrothermal alteration in creating geothermal and epithermal mineral resources: the Ohakuri ignimbrite (Taupo Volcanic Zone, New Zealand). J Volcanol Geoth Res. 2020a;390: 106703. https://doi.org/10.1016/j.jvolgeores.2019.106703.
Heap MJ, Kushnir AR, Vasseur J, Wadsworth FB, Harlé P, Baud P, Kennedy BM, Troll VR, Deegan FM. The thermal properties of porous andesite. J Volcanol Geotherm Res. 2020b;398: 106901. https://doi.org/10.1016/j.jvolgeores.2020.106901.
Heap MJ, Baumann TS, Rosas-Carbajal M, Komorowski JC, Gilg HA, Villeneuve M, Moretti R, Baud P, Carbillet L, Harnett C, Reuschlé T. Alteration-induced volcano instability at La Soufrière de Guadeloupe (Eastern Caribbean). J Geophys Res Solid Earth. 2021. https://doi.org/10.1029/2021JB022514.
Heard HC, Page L. Elastic moduli, thermal expansion, and inferred permeability of two granites to 350°C and 55 megapascals. J Geophys Res. 1982;87:9340–8.
Heidarzadeh S, Saeidi A, Lavoie C, Rouleau A. Geochemical characterization of a heterogenous rock mass using geological and laboratory test results: a case study of the Niobec Mine, Quebec (Canada). SN Appl Sci. 2021;3(640):20. https://doi.org/10.1007/s42452-021-04617-1.
Hofmann H, Peters E, Hernández-Ochoa AF, Parisio F, Lepillier B. Hydraulic stimulation scenarios for a potential Enhanced Geothermal System (EGS) in Acoculco, Mexico. In: Proceedings World Geothermal Congress 2020+1, Reykjavik, Iceland, 2021. p. 6.

Homuth S, Götz AE, Sass I. Reservoir characterization of the Upper Jurassic geothermal target formations (Molasse Basin, Germany): role of thermofacies as exploration tool. Geoth Energy Sci. 2015;3:41–9. https://doi.org/10.5194/gtes-3-41-2015.
Hrouda F, Chlupáčová M, Chadima M. The Use of Magnetic Susceptibility of Rocks in Geological Exploration. Terraplus, Brno; 2009. p. 25. https://www.geomatrix.co.uk/cms/resources/downloads/the-use-of-magnetic-susceptibility-of-rocks-in-geological-exploration-v1-1.pdf. Accessed 20 September 2021.
Hughes DS, Maurette C. Variation of elastic wave velocities in basic igneous rocks with pressure and temperature. Geophysics. 1957;22(1):23–31. https://doi.org/10.1190/1.1438332.
IAPWS R15-11: International Association for the Properties of Water and Steam, Release on the IAPWS Formulation 2011 for the Thermal Conductivity of Ordinary Water Substance, 2011.
IAPWS R6-95: International Association for the Properties of Water and Steam, Revised Release on the IAPWS Formulation 1995 for the Thermodynamic Properties of Ordinary Water Substance for General and Scientific Use, 2016.
ZH Instruments. ZH Instruments Magnetic susceptibility meter SM30—User's manual. Czech, Brno; 2008. p. 56.
Jiang X-W, Wang X-S, Li W. Semi-empirical equations for the systematic decrease in permeability with depth in porous and fractured media. Hydrogeol J. 2010;18:839–50. https://doi.org/10.1007/s10040-010-0575-3.
Jolie E, Bruhn D, López-Hernández A, Liotta D, Garduño-Monroy VH, Lelli M, Páll Hersir G, Arango-Galván C, Bonté D, Calcagno P, Deb P, Clauser C, Peters E, Hernández-Ochoa AF, Huenges E, González-Acevedo ZI, Kieling K, Trumpy E, Vargas J, Gutiérrez-Negrín LC, Aragón-Aguilar A, Halldórsdóttir S, González-Partida E, van Wees J-D, Ramírez-Montes, MA, Diez-León HD, and the GEMex team: GEMex—A Mexican-European Research Cooperation on Development of Superhot and Engineered Geothermal Systems. In: Proceedings 43rd Workshop on Geothermal Reservoir Engineering Stanford University, Stanford, California, February 12–14, 2018; 2018, SGP-TR-2013, p. 10.
Jolliffle I. Principal component analysis. Encycl Stat Behav Sci. 2005;3:1580–4. https://doi.org/10.1002/0470013192.bsa501.
Klinkenberg LJ. The permeability of porous media to liquids and gases, Drilling Production Practice, API, 200–213. 1941. https://www.onepetro.org/conference-paper/API-41-200. Accessed 20 September 2021.
Konietzky H, Wang F. Thermal behaviour of rocks. Institut für Geotechnik, TU Bergakademie Freiberg; 2019. p. 20. https://tu-freiberg.de/sites/default/files/media/professur-felsmechanik-32204/E-book/30_thermal_behaviour_of_rocks_0.pdf. Accessed 15 September 2021.
Kozdrój W, Nawrocki J, Pańczyk-Nawrocka M, Ziółkowska-Kozdrój M, Wójcik K, Kumek J, González-Partida E. Stratigraphic, petrological features and datings of Los Humeros rocks from outcrops and boreholes, in: Final report on active systems: Los Humeros and Acoculco. GEMex H2020 project, European Commission, WP4. Deliverable 4.1. 2019;1:27–42. http://www.gemex-h2020.eu. Accessed 28 Sep 2021.
Kruszewski M, Hofmann H, Alvarez FG, Bianco C, Haro AJ, Garduno VH, Liotta D, Trumpy E, Brogi A, Wheeler W, Basteesen E, Parisio F, Saenger EH. Integrated stress field estimation and implications for enhanced geothermal system development in Acoculco. Mexico Geothermics. 2020;89:101931. https://doi.org/10.1016/j.geothermics.2020.101931.
Le Maitre RW, Streckeisen A. Igneous rocks: a classification and glossary of terms—recommendations of the International Union of Geological Sciences subcommission on the systematics of igneous rocks. Cambridge: Cambridge University Press; 2002. https://doi.org/10.1017/CBO9780511535581.
Lelli M, Kretzschmar TG, Cabassi J, Doveri M, Sanchez-Avila JI, Gherardi F, Magro G, Norelli F. Fluid geochemistry of the Los Humeros geothermal field (LHGF—Puebla, Mexico): new constraints for the conceptual model. Geothermics. 2020;90: 101983. https://doi.org/10.1016/j.geothermics.2020.101983.
Lenhardt N, Götz AE. Geothermal reservoir potential of volcaniclastic settings: the Valley of Mexico, Central Mexico. Renew Energy. 2015;77:423–9. https://doi.org/10.1016/j.renene.2014.12.034.
Lippmann E, Rauen A. Measurements of Thermal Conductivity (TC) and Thermal Diffusivity (TD) by the Optical Scanning Technology. Germany, Schaufling: Lippmann and Rauen GbR; 2009. p. 49.
López-Hernández A. Estudio Regional Volcánico y Estructural del Campo Geotérmico de Los Humeros, Puebla, México. Geotermia Revista Mexicana De Geoenergía. 1995;11:17–36.
López-Hernández A, García-Estrada G, Aguirre-Díaz G, González-Partida E, Palma-Guzmán H, Quijano-Léon J. Hydrothermal activity in the Tulancingo-Acoculco Caldera Complex, central Mexico: exploratory studies. Geothermics. 2009;38:279–93. https://doi.org/10.1016/j.geothermics.2009.05.001.
Lorenzo-Pulido CD. Borehole Geophysics and Geology of Well H-43, Los Humeros Geothermal Field, Puebla, México. Mexico: Comisíon Federal de Electricidad. 2008; Report 23, p. 40.
Lucci F, Carrasco-Núñez G, Rossetti F, Theye T, White JC, Urbani S, Azizi H, Asahara Y, Giordano G. Anatomy of the magmatic plumbing system of Los Humeros Caldera (Mexico): implications for geothermal systems. Solid Earth. 2020;11:125–59. https://doi.org/10.5194/se-11-125-2020.
Micromeritics: AccuPyc 1330 Pycnometer, V2.02, Part No. 133-42808-01. Germany, Munich:Micromeritics GmbH; 1997. p. 67.
Micromeritics: GeoPyc 1360, V3., Part 136-42801-01. Germany, Munich:Micromeritics GmbH; 1998. p. 69.
Middlemost EAK. Naming materials in the magma/igneous rock system. Earth-Sci Rev. 1994;37(3–4):215–24. https://doi.org/10.1016/0012-8252(94)90029-9.
Mielke P, Nehler M, Bignall G, Sass I. Thermo-physical rock properties and the impact of advancing hydrothermal alteration—a case study from the Tauhara geothermal field, New Zealand. J Volcanol Geotherm Res. 2015;301:14–28. https://doi.org/10.1016/j.jvolgeores.2015.04.007.
Mielke P, Weinert S, Bignall G, Sass I. Thermo-physical rock properties of greywacke basement rock and intrusive lavas from the Taupo Volcanic Zone, New Zealand. J Volcanol Geotherm Res. 2016;324:179–89. https://doi.org/10.1016/j.jvolgeores.2016.06.002.
Mielke P, Bär K, Sass I. Determining the relationship of thermal conductivity and compressional wave velocity of common rock types as a basis for reservoir characterization. J Appl Geophys. 2017;140:135–44. https://doi.org/10.1016/j.jappgeo.2017.04.002.

Navelot V, Géraud Y, Favier A, Diraison M, Corsini M, Lardeaux J-M, Verati C, de Lépinary JM, Legendre L, Beauchamps G. Petrophysical properties of volcanic rocks and impacts of hydrothermal alteration in the Guadeloupe Archipelago (West Indies). J Volcanol Geotherm Res. 2018;360:1–21. https://doi.org/10.1016/j.jvolgeores.2018.07.004.

Norden B, Förster A, Förster H-J, Fuchs S. Temperature and pressure corrections applied to rock thermal conductivity: impact on subsurface temperature prognosis and heat-flow determination in geothermal exploration. Geotherm Energy. 2020;1:1–19. https://doi.org/10.1186/s40517-020-0157-0.

Norini G, Carrasco-Núñez G, Corbo F, Lermo J, Hernández J, Castro C, Bonini M, Montanari D, Corti G, Moratti G, Piccardi L, Chavez G, Zuluaga MC, Ramírez M, Cedillo F. The structural architecture of the Los Humeros volcanic complex and geothermal field. J Volcanol Geotherm Res. 2019;381:312–29. https://doi.org/10.1016/j.jvolgeores.2019.06.010.

Ochoa-Camarillo H, Buitrón-Sánchez BE, Silva-Pineda A. Redbeds of the Huayacocotla anticlinorium, state of Hidalgo, east-central Mexico. Special Papers-Geol Soc Am. 1999;340:59–68. https://doi.org/10.1130/0-8137-2340-x.59.

Oliva-Urcia B, Kontny A, Vahle C, Schleicher AM. Modification of the magnetic mineralogy in basalts due to fluid–rock interactions in a high-temperature geothermal system (Krafla, Iceland). Geophys J Int. 2011;186(1):155–74. https://doi.org/10.1111/j.1365-246X.2011.05029.x.

Olvera-García E, Bianco C, Garduño-Monroy VH, Brogi A, Liotta D, Wheeler W, Gómez-Alvarez SN-B, Jiménez-Haro A, Guevara-Alday JA, Bastesen E, Lepillier B, Zucchi M, Caggianelli A, Ruggieri G. Geology of Las Minas: an example of an exhumed geothermal system (Eastern Trans-Mexican Volcanic Belt). J Maps. 2020;16(2):918–26. https://doi.org/10.1080/17445647.2020.1842815.

Pinti DL, Castro MC, Lopez-Hernandez A, Han G, Shouakar-Stash O, Hall CM, Ramírez-Montes M. Fluid circulation and reservoir conditions of the Los Humeros Geothermal Field (LHGF), Mexico, as revealed by a noble gas survey. J Volcanol Geoth Res. 2017;333–334:104–15. https://doi.org/10.1016/j.jvolgeores.2017.01.015.

Pola A, Crosta G, Fusi N, Barberini V, Norini G. Influence of alteration on physical properties of volcanic rocks. Tectonophysics. 2012;566–567:67–86. https://doi.org/10.1016/j.tecto.2012.07.017.

Pola A, Martínez-Martínez J, Macías JL, Fusi N, Crosta G, Garduño-Monroy VH, Núñez-Hurtado JA. Geomechanical characterization of the Miocene Cuitzeo ignimbrites, Michoacán, Central Mexico. Eng Geol. 2016;214:79–93. https://doi.org/10.1016/j.enggeo.2016.10.003.

Popov Y, Beardsmore G, Clauser C, Roy S. ISRM suggested methods for determining thermal properties of rocks from laboratory tests at atmospheric pressure. Rock Mech Rock Eng. 2016;49:4179–207. https://doi.org/10.1007/s00603-016-1070-5.

Qi D, Hesketh T. An analysis of upscaling techniques for reservoir simulation. Pet Sci Technol. 2005;23:827–42. https://doi.org/10.1081/LFT-200033132.

Qi H, Ba J, Müller TM. Temperature effect on the velocity-porosity relationship in rocks. JGR Solid Earth. 2020. https://doi.org/10.1029/2019JB019317.

Reinsch T, Dobson P, Asanuma H, Huenges E, Poletto F, Sanjuan B. Utilizing supercritical geothermal systems: a review of past ventures and ongoing research activities. Geotherm Energy. 2017;5(16):25. https://doi.org/10.1186/s40517-017-0075-y.

Ringrose P, Bentley M. Reservoir model design—a practitioner's guide. Springer, Switzerland; 2021. p. 249. https://doi.org/10.1007/978-3-030-70163-5.

Rochelle CA, Lacinska A, Kilpatrick A, Rushton J, Weydt LM, Bär K, Sass I. Evidence for fracture-hosted fluid-rock reactions within geothermal reservoirs of the eastern Trans-Mexico volcanic belt. In: Proceedings World Geothermal Congress 2020+1, Reykjavik, Iceland, 2021. p. 11.

Romo-Jones JM, Gutiérrez-Negrín LC, Canchola-Félix I. 2019-México Country Report. IEA Geothermal. 2020. https://drive.google.com/file/d/1Nq9gPbgzto7bMvv5hktjhi5JBxwJXV49/view. Accessed 28 Sep 2021.

Rühaak W, Guadagnini A, Geiger S, Bär K, Gu Y, Aretz A, Hohmuth S, Sass I. Upscaling thermal conductivities of sedimentary formations for geothermal exploration. Geothermics. 2015;8:49–61. https://doi.org/10.1016/j.geothermics.2015.08.004.

Sari M. The stochastic assessment of strength and deformability characteristics for a pyroclastic rock mass. Int J Rock Mech Min Sci. 2009;46:613–26. https://doi.org/10.1016/j.ijrmms.2008.07.007.

Sass I, Götz AE. Geothermal reservoir characterization: a thermofacies concept. Terra Nova. 2012;24:142–7. https://doi.org/10.1111/j.1365-3121.2011.01048.x.

Schön JH. Physical properties of rocks: fundamentals and principles of petrophysics. Amsterdam: Elsevier; 2015.

Scott SW, Covell C, Júlíusson E, Valfells Á, Newson J, Hrafnkelsson B, Pállson H, Gudjónsdóttir M. A probalistic geological model of the Krafla geothermal system constrained by gravimetric data. Geotherm Energy. 2019;7(29–2019):1–30. https://doi.org/10.1186/s40517-019-0143-6.

Setaram Instrumentation. K/C80-1A C80 Commissioning. France, Caluire: Setaram Instrumentation KEP Technologies; 2009, pp. 52.

SGM. CARTA GEOLÓGICO—MINERA, Veracruz, E14-3, Veracruz, Puebla y Tlaxcala. Mexico: Servicio Geológico Mexicano, first edition, 2002.

SGM. CARTA GEOLÓGICO—MINERA, Perote, E14-B26, Veracruz y Puebla. Mexico: Servicio Geológico Mexicano, first edition, 2007.

SGM. CARTA GEOLÓGICO—MINERA, Xonactlán, E14-B25, Veracruz y Puebla. Mexico: Servicio Geológico Mexicano, first edition, 2011.

SGM. CARTA GEOLÓGICO—MINERA, Mexcaltepec, E14-B24, Veracruz y Puebla. Mexico: Servicio Geológico Mexicano, first edition, 2012.

Takahashi I. Quantifying Information and Uncertainty of Rock Property Estimation from Seismic Data. PhD thesis, USA, California: Geophysics, Stanford University; 2000. p. 200.

Tello HE. Estado de equilibrio soluto-mineral y saturación de minerales de alteración en fluidos geotérmicos de alta temperature. PhD Thesis, xvii + p. 271. Mexico: Facultad de Ingeniería, UNAM; 2005.

Urbani S, Giordano G, Lucci F, Rossetti F, Acocella V, Carrasco-Núñez G. Estimating the depth and evolution of intrusions at resurgent calderas: Los Humeros (Mexico). Solid Earth. 2020;11:527–45. https://doi.org/10.5194/se-11-527-2020.

Villeneuve M, Kennedy B, Gravley D, Mordensky S. Characteristics of altered volcanic rocks in geothermal reservoirs, in Fontoura SAB, Rocca RJ, Mendoza JP (Eds.): Rock Mechanics for Natural Resources and Infrastructure Development. In: Proceedings of the 14th International Congress on Rock Mechanics and Rock Engineering (ISRM 2019), Foz do Iguassu, Brazil, 2019. CRC Press Taylor and Francis Group, United Kingdom. 2019;6:SG3120–3127.
Vinciguerra S, Trovato C, Meredith PG, Benson PM. Relating seismic velocities, thermal cracking and permeability in Mt. Etna and Iceland basalts. Int J Rock Mech Min Sci. 2005;42(7–8):900–10. https://doi.org/10.1016/j.ijrmms.2005.05.022.
Vinciguerra S, Trovato C, Meredith PG, Benson PM, Troise C, De Natale G. Understanding the seismic velocity structure of Campi Flegrei caldera (Italy): from the laboratory to the field scale. Pure Appl Geophys. 2006;163(10):2205–21. https://doi.org/10.1007/s00024-006-0118-y.
Viniegra-Osario F. Geología del Macizo de Teziutlán y la Cuenca Cenozoica deVeracruz. Asociación Mexicana De Geólogos Petroleros. 1965;17:101–63.
von Dobeneck T, Müller M, Bosbach B, Klügel A. Ground magnetic surveying and susceptibility mapping across weathered basalt dikes reveal soil creep and pedoturbation. Front Earth Sci. 2021;8: 592986. https://doi.org/10.3389/feart.2020.592986.
Vosteen H-D, Schellschmidt R. Influence of temperature on thermal conductivity, thermal capacity and thermal diffusivity for different types of rock. Phys Chem Earth. 2003;28:499–509. https://doi.org/10.1016/S1474-7065(03)00069-X.
Wang S, Huang Z, Wu Y-S, Winterfeld PH, Zerpa LE. A semi-analytical correlation of thermal-hydraulic-mechanical behaviour of fractures and its application to modeling reservoir scale cold water injection problems in enhanced geothermal reservoirs. Geothermics. 2016;64:81–95. https://doi.org/10.1016/j.geothermics.2016.04.005.
Weinert S, Bär K, Sass I. Database of petrophysical properties of the mid-German crystalline high. Earth Syst Sci Data. 2021;13:1441–59. https://doi.org/10.5194/essd-13-1441-2021.
Weydt LM, Heldmann C-DJ, Machel HG, Sass I. From oil field to geothermal reservoir: assessment for geothermal utilization of two regionally extensive Devonian carbonate aquifers in Alberta, Canada. Solid Earth. 2018a;9:953–83. https://doi.org/10.5194/se-9-953-2018.
Weydt LM, Bär K, Colombero C, Comina C, Deb P, Lepillier B, Mandrone G, Milsch H, Rochelle CA, Vagnon F, Sass I. Outcrop analogue study to determine reservoir properties of the Los Humeros and Acoculco geothermal fields, Mexico. Adv Geosci. 2018b;45:281–7. https://doi.org/10.5194/adgeo-45-281-2018.
Weydt LM, Ramírez-Guzmán ÁA, Pola A, Lepillier B, Kummerow J, Mandrone G, Comina C, Deb P, Norini G, Gonzalez-Partida E, Avellán DR, Macías JL, Bär K, Sass I. Petrophysical and mechanical rock property database of the Los Humeros and Acoculco geothermal fields (Mexico). Earth Syst Sci Data. 2021a;13:571–98. https://doi.org/10.5194/essd-13-571-2021.
Weydt LM, Bär K, Sass I. Petrophysical reservoir characterization of the Los Humeros and Acoculco geothermal fields, Mexico. In: Proceedings World Geothermal Congress 2020+1, Reykjavik, Iceland, 2021b.
Willcox C. Eruptive, magmatic and structural evolution of a large explosive caldera volcano: Los Humeros México. PhD thesis, x + p. 326, 1 Appendix. United Kingdom: University of Leicester; 2011. https://leicester.figshare.com/articles/thesis/Eruptive_Magmatic_and_Structural_Evolution_of_a_Large_Explosive_Caldera_Volcano_Los_Humeros_Central_Mexico/10104785/1. Accessed 20 March 2021.
Wyering LD, Villeneuve MC, Wallis IC, Siratovitch PA, Kennedy BM, Gravley DM, Cant JL. Mechanical and physical properties of hydrothermally altered rock, Taupo Volcanic Zone, New Zealand. J Volcanol Geotherm Res. 2014;288:76–93. https://doi.org/10.1016/j.jvolgeores.2014.10.008.
Yáñez C, García S. Exploración de la región geotérmica Los Humeros-Las Derrumbadas. Internal report, Estados de Puebla y Veracruz, Comisión Federal de Electricidad, Mexico City, Mexico. 1982:1–96.
Zarrouk S, Watson A. Thermodynamic and transport properties of saturated steam and water. Geothermal Program, University of Auckland, Faculty of Engineering; 2010. p. 23.
Zimmermann RW, Somerton WH, King MS. Compressibility of porous rocks. J Geophys Res. 1986;91(12):765–77. https://doi.org/10.1029/JB091iB12p12765.

Publisher's Note